Spring 5-2023

Measurements of Magnetic Field Penetration of Materials for Superconducting Radiofrequency Cavities

Iresha Harshani Senevirathne
Old Dominion University, isene001@odu.edu

Recommended Citation

MEASUREMENTS OF MAGNETIC FIELD PENETRATION OF MATERIALS FOR SUPERCONDUCTING RADIOFREQUENCY CAVITIES

by

Iresha Harshani Senevirathne
B.S. January 2014, University of Peradeniya, Sri Lanka
M.S. May 2018, Old Dominion University, USA

A Dissertation Submitted to the Faculty of
Old Dominion University in Partial Fulfillment of the
Requirements for the Degree of

DOCTOR OF PHILOSOPHY

PHYSICS

OLD DOMINION UNIVERSITY
May 2023

Approved by:

Jean Delayen (Director)

Alexander Gurevich (Member)

Anne-Marie Valente-Feliciano (Member)

Moskov Amaryan (Member)

Khan Iftekharuddin (Member)

ABSTRACT

MEASUREMENTS OF MAGNETIC FIELD PENETRATION OF MATERIALS FOR SUPERCONDUCTING RADIOFREQUENCY CAVITIES

Iresha Harshani Senevirathne
Old Dominion University, 2023
Director: Prof. Jean Delayen

Superconducting Radio Frequency (SRF) cavities used in particle accelerators are typically formed from or coated with superconducting materials. Currently high purity niobium is the material of choice for SRF cavities which have been optimized to operate near their theoretical field limits. This brings about the need for significant R&D efforts to develop next generation superconducting materials which could outperform Nb and keep up with the demands of new accelerator facilities. To achieve high quality factors and accelerating gradients, the cavity material should be able to remain in the superconducting Meissner state under high RF magnetic field without penetration of quantized magnetic vortices through the cavity wall. Therefore, the magnetic field at which vortices penetrate in a superconductor is one of the key parameters of merit of SRF cavities. Techniques to measure the onset of magnetic field penetration on thin film samples need to be developed to mitigate the issues with the conventional magnetometry measurements which are strongly influenced by the film orientation and shape and edge effects. The applied magnetic field is also needed to be parallel to the one side of the superconductor to resemble the magnetic field profile at the surface of the SRF cavities operating at fundamental accelerating mode. In this work we report the development of an experimental setup called Magnetic Field Penetration (MFP) magnetometer to measure the field of full flux penetration through bulk, thin films and multilayered superconductors. Our system combines a small superconducting solenoid which can generate the magnetic field up to 500 mT at the sample surface and three Hall probes to detect the full flux penetration through the planner superconductor with 2 inch diameter. This setup was used to study alternative materials which could potentially outperform niobium, as well as SIS multilayer coatings on niobium.

To my family, friends and all who have supported through this journey....

ACKNOWLEDGMENTS

First and foremost, I would like to acknowledge my advisor Prof. Jean Delayen for his continuous support and guidance in my doctoral study and research with patience and motivation. I was given the opportunities to expand my knowledge on the subject and to present my work in the presence of the accelerator science community.

I express my gratitude to Prof. Alex Gurevich for his explanation on data, guidance, advices and suggestions to improve the experimental work and research articles. I am also grateful to my Jefferson Lab mentor Dr. Anne-Marie Valente-Feliciano for providing many samples I needed to test with my setup and for useful discussion on the progress of the research project. I like to thank the rest of the advisory committee members, Prof. Moskov Amaryan and Prof. Khan Iftekharuddin, for providing useful feedback during the annual reviews.

I am thankful to Dr. Gianluigi Ciovati for his support to run the experiment at Jefferson Lab providing the necessary equipment. My sincere thank to Read Beverstock for his support whenever needed during the experiment, Dr. Eric Lechner and Carrie Baxley for their help to fulfill some tasks in the chem room, especially for mechanical polishing and electropolishing of my samples, and Dr. Ishwari Parajuli for help in writing Labview Program. I'm also thankful to Dr. Junki Makita and Dr. Salvador Sosa for their initial guidance to start this experiment. My thanks also go to Dr. Nizam Sayeed and Dr. Chris Sundahl for providing me with good quality Nb_3Sn samples. I would also like to acknowledge Pete Kushnick and Justin Kent for helping in low temperature measurements at VTA, Steve Dutton for helping me on soldering very tiny wires in my setup and all other SRF and the machine shop staff at Jefferson Lab for their support during my experiment.

I express my gratitude to the faculty and staff members of the Department of Physics at Old Dominion University for accepting me as a graduate student and for helping me during my graduate studies. My special thank go to Lisa Okun, Delicia Malin and Annette Guzman-Smith for handling all the administrative tasks so I could focus on my research work. I give special thanks to the international office at ODU for their help during my stay at Old Dominion University.

I would like to express my sense gratitude to the Department of Physics, University of Peradeniya, and all my teachers who supported me along the way.

I am also thankful to Ven. Bandarawela Seelaviveka, Kurnia Foe, my dear friend Patty Lyle and Sri Lankan friends for their constant friendship and immense support throughout

tough times in my stay away from my home country.

I want to express my sincere gratitude to my parents K. G. Senevirathne, Sujatha Pathiraja and my husband, Nandiaka Bandara for their unconditional love, encouragement, and support to pursue my educational endeavors.

Finally, I would like to thank all who have helped me in every way during this journey.

TABLE OF CONTENTS

LIST OF TABLES

LIST OF FIGURES

Figure Page

CHAPTER 1

INTRODUCTION

Particle accelerators are machines that propel charged particles such as electrons and protons to high speeds and energies. The collision of these accelerated charged particles with targets or other particles releases energy, produces nuclear reactions, scatters particles, and produces other particles such as neutrons. This allows scientists to discover the world of the particles containing atoms, atomic nuclei, and nucleons as well as particles like the Higgs bosons.

Basically, in the accelerator, the continuous particle beam coming out of an ion or electron source is bunched at a given RF frequency and then accelerated up to the required final energy. In general, they are operated as pulsed accelerators i.e. the beam generated by the ion source is delivered as short or long pulses of a given time length between a few microseconds and a few milliseconds at a given repetition frequency usually between 1 Hz and 100 Hz. They can operate continuously as well, producing a constant stream of particles called continuous wave (CW) accelerators [1].

Accelerators are generally linear or circular. In the linear accelerator, called linac, the particle beam passes through only once, therefore they will be more expensive when higher energies are required. Linacs are used for fixed-target experiments, as injectors to circular accelerators, or as linear colliders. In the circular accelerator, the particles are injected from a linac and they move in a very fast circle, receiving a bunch of little kicks each time around in the circular accelerator to achieve high energies. The circular accelerator can be used for both fixed target and colliding beam experiments.

1.1 ACCELERATING CAVITIES

Accelerating cavities are a key component of the particle accelerators which impart energy to charged particles. RF power (typically between 50-3000 MHz [2]) is applied to a cavity close to its resonant frequency to build up large electromagnetic fields to accelerate charged particles injected from the source into a well defined high energetic beam. Typical accelerating cavities operate at the fundamental, or lowest RF frequency, TM_{010} mode. In this mode, the electric field pointing towards the beam direction is maximum on the axis

and decays radially to zero at the cavity walls. The magnetic field is azimuthal, with the highest magnetic field located near the cavity equator and zero on the cavity axis. Accelerating cavities are elliptical that is derived from the right circular cylinder referred to as a "pillbox" shape. There are ports on the beam tubes to bring rf power in to establish the fields and deliver power to the beam.

Normal conducting copper cavities were typically used in the early stages of particle acceleration. Later on, copper cavities became uneconomical due to superconducting cavities having a surface resistance (R_s) many orders of magnitude lower, hence lower ohmic power at the cavity wall than that of copper. Eventhough superconducting cavities require refrigerator power to operate at cryogenic temperatures (2-4 K), the net gain factor is still attractive. Copper accelerating structures limit the maximum accelerating gradient to values of less than 1 MV/m in continuous wave operation. In pulsed operation accelerating fields over 100 MV/m seems accessible but with a low pulse duration in the order of microsecond with low duty factor ($< 0.1\%$). Such applications are needed a large amount of RF power that is limited to control dissipating high power in the walls of a copper cavity. Superconducting radio-frequency (SRF) cavities stand out over normal conducting cavities with their many capabilities such as small input RF power, lower ohmic losses, high voltage production, etc in both continuous wave and pulsed applications [2].

High-purity niobium is the material of choice for the fabrication of SRF cavities, because of its relatively high value of superconducting transition temperature, ($T_c = 9.2$ K), the lower critical magnetic field (H_{c1}), relative abundance and ease in availability, and mechanical strength as well as formability. The material should be free of defects that can initiate a thermal breakdown and defects may be detected by quality control methods such as eddy current scanning and identified by several special methods. Conventionally, niobium cavities are fabricated from sheet niobium by the formation of half-cells by deep drawing, followed by trim machining and Electron-Beam Welding (EBW). This should be done by choosing welding parameters carefully while following several cleaning steps.

Performance of Nb cavities can be limited by multipacting, trapped magnetic flux, field emission and thermal breakdown which mostly result from topographic surface imperfections and nonsuperconducting materials precipitates [1]. Recent technological advances have significantly mitigated these issues and increased the accelerating gradients from a few MV/m to 45-50 MV/m [3–7]. As a result, the best Nb cavities can now operate at RF field amplitudes close to a theoretical limit at which the surface RF magnetic field approaches the superheating field H_{sh} [8–10]. Further progress in the SRF accelerator technology demands

even higher accelerating gradients (reduces the number of the cavities needed to achieve the required energy of a beam) and lower RF losses (decreases the electric power consumption) while increasing the operating temperature to 4.2 K or higher (gives the ability to use less expensive cooling methods). This challenging task can only be accomplished using superconductors that have higher critical temperatures than $T_c = 9.2$ K of Nb.

Besides a higher T_c another important parameter of merit of the SRF cavity material is the field onset of magnetic flux penetration which cause strong dissipation under the RF field. The superheating magnetic field thus defines a theoretical field limit of SRF breakdown at which explosive flux penetration accompanied by high RF losses occurs. Currently, the best Nb cavities can operate at the peak magnetic field around 200-220 mT, which is close to H_{sh} for Nb [1].

Alternative superconductors having higher T_c and H_{sh} [11], all of them have H_{c1} lower than that of Nb. Smaller H_{c1} make alternative superconductors prone to premature flux penetration and high RF losses at fields well below H_{sh}. This is because materials or topographic defects on the cavity surface trigger local flux penetration at $H_{c1} < H_p < H_{sh}$ or even at $H_p < H_{c1}$ for polycrystalline superconductors with weakly-coupled grain boundaries [12].

1.2 MULTILAYER STRUCTURE

To address the so-called problem of premature flux penetration in low-H_{c1} superconductors, an SIS multilayer coating has been proposed [13, 14]. In this case, the inner surface of the Nb cavity is coated with thin superconducting (S) layers having higher T_c and H_{sh} separated by thin insulating (I) layers. Here S layers should be thinner than the London penetration depth, λ_L of the superconductor and the thickness of I layers can be a few nm to suppress the Josephson coupling between S layers. With such an SIS structure, there is a potential to take advantage of the high H_{sh} and low R_s of the alternative superconductors used in the S layers regardless of their small H_{c1}. SRF researchers have been putting significant effort into developing SIS multilayers, and they are producing excellent work [15–19].

1.3 MAGNETOMETRY TECHNIQUES

The onset of magnetic field penetration, B_p in a thin film of SIS multilayer structures is an important characteristic of high-field performance of alternative materials for SRF cavities [20] but the measurements of B_p on thin film test samples under the conditions emulating those of SRF cavities are challenging. The problem is that the RF magnetic field

in the accelerating TM mode in the cavity is parallel to the surface of the superconductor so the screening Meissner RF currents only flow in a thin layer $\sim \lambda_L$ at the inner surface of the cavity. However, in typical dc magnetometry measurements, B_p is extracted from the field dependence of the magnetic moment, $M(B)$ of a sample placed in a nearly uniform magnetic field. In this case, the magnetic field is applied to both sides of the sample, and $M(B)$ depends strongly on the geometry of a flat sample and its orientation concerning B [21]. The so-obtained values of B_p are strongly influenced by the pinning of normal conducting vortices and surface and magnetic geometrical barriers [22, 23] and thus are hardly representative of B_p for the SRF cavity geometry.

Several methods have been developed to measure the field-dependent quality factors $Q(B)$ and the breakdown fields on test thin film samples of alternative SRF materials. In a quadrupole resonator technique a thin film sample deposited onto a 3" substrate is welded to the niobium resonator [24, 25]. However, this technique can only probe a low-field part of $Q(B)$ (currently up to 60 mT well below $B_{sh} \approx 240$ mT of Nb) and cannot measure the breakdown fields $\simeq B_{sh}$ of the promising SRF materials as all of them have B_{sh} higher than B_{sh} of Nb. A way around this problem is to measure the flux penetration field for a thin film sample placed in parallel dc magnetic fields of superconducting solenoids which can produce fields well above B_{sh}. This was implemented in Ref. [26] in which the Hall probes were used to detect the penetration field of thin films deposited onto a stainless steel hollow tube. This technique allows one to apply a strong dc magnetic field parallel to the outer surface of the superconducting film but requires uniform film coating of a long cylindrical tube and cannot be used to measure test thin film of multilayer small flat samples of different SRF materials.

The problems outlined above bring about the need to develop a simple technique to measure the flux penetration field through thin film or SIS multilayer samples typically deposited onto 1-2" substrates. This technique should provide a parallel magnetic field applied to only one side of the sample to emulate the field configuration of SRF cavities. In this work, we report the development of such a technique which includes a Hall probe experimental setup, called an MFP magnetometer for the measurement of the field of full flux penetration B_p through a flat superconducting sample placed under a small superconducting solenoid which can generate magnetic field higher than 500 mT. To illustrate the capabilities of this setup, we also discuss the results of measurements of B_p on bulk Pb and Nb, thin film, and multilayer sample measurements along with other sample characterizations.

1.4 ORGANIZATION OF DISSERTATION

Chapter 2 describes the Meissner effect, the theories of superconductivity, and the critical magnetic fields of superconductors.

Chapter 3 gives a brief outline of superconducting RF cavities along with their fundamentals and limitations.

Chapter 4 provides a description of materials used to fabricate superconducting cavities with reasons to look beyond Nb and materials proposed for future generation SRF cavities including SIS multilayer structure.

Chapter 5 includes the design and fabrication of magnetic field penetration (MFP) magnetometer and its calibration using bulk superconducting samples.

Chapter 6 studies the magnetic field penetration measurements of bulk superconductors using the MFP magnetometer. The effect of sample thickness on the first onset of magnetic penetration (B_p) and hysteresis behavior based on the measurements is also discussed. Moreover, the model suggested to simulate the bulk Pb and Nb is presented.

Chapter 7 moves on to the characterizations of the thin film superconductors using the MFP magnetometer and other characterizing techniques such as RRR, and XRD measurements.

Chapter 8 describes the SIS multilayer measurements (NbTiN/AlN on bulk Nb) along with the study of the effect of NbTiN thickness and substrate roughness.

Chapter 9 includes the summarized results, conclusions, and future outlook.

CHAPTER 2

SUPERCONDUCTIVITY

Superconductivity is a phenomenon in certain metals and ceramics where the resistance of the material does not gradually decrease at low temperatures, rather, it suddenly drops to zero at a specific temperature for each superconductor. This characteristic temperature is called its critical temperature (T_c) and varies over a wide range. In Table 1, critical temperatures of some materials used in our experiment are listed. Those elements become superconducting under normal pressure at their T_c. The critical temperature is usually very sensitive to the presence of magnetic impurities. As shown in Fig. 1, the transition is typically sharp in pure material, therefore the T_c of these materials is well defined. Most practical materials are inhomogeneous and their transition is broad.
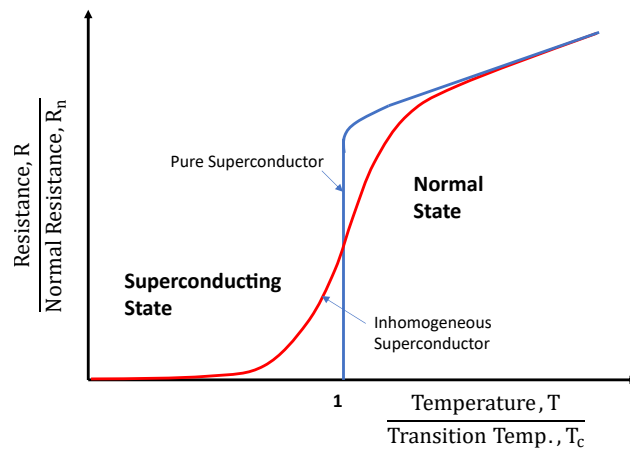
FIG. 1. The superconducting resistance transition at T_c for pure (blue) and inhomogeneous (red) materials. Adapted from [27].

TABLE 1. Critical temperatures of some superconducting materials used in our experiment.

Superconducting Material	Critical Temperature (T_c) [K]
Pb	7.2 [28]
Nb	9.2 [29]
NbTi	9.7 [30]
Nb_3Sn	18.1 [31]
NbTiN	16-18 [32]

Due to its cryogenic nature, superconductivity was not discovered until Dutch physicist Heike Kamerlingh Onnes was able to liquefy Helium using the Hampson-Linde cycle in 1908. With a boiling point of 4K at ambient pressure, liquid helium allowed Onnes to experiment with very cold temperatures. He was able to discover that resistivity decreases with temperature, but the behavior was unknown as it approached 0 K. In April 1911, Onnes measured the resistivity of Mercury wire and the resistance dropped to 0 suddenly at about 4K [33]. He later won the 1913 Nobel Prize for his work. Further experiments, many interesting discoveries were made and phenomenological theories by Gorter and Casimir [34], by F. and H. London [35], and Ginzburg and Landau [36] contributed to a deeper understanding of this phenomenon. In 1957, J. Bardeen, L.N. Cooper, and J. R. Schrieffer published BCS Theory [37, 38], which explains the microscopic origin of superconductivity and received a Nobel Prize in 1972.

Superconductors have the major advantage that their resistivity is zero, allowing for persistent a large current flow without heating the wire. This can be used to create very strong magnetic coils in MRI imaging machines, and strong magnetic fields in scientific testing equipment, colliders, or any application that requires a high permanent magnetic field. They can also move electric power around with zero resistance, making them very desirable for power cables and efficient devices.

2.1 MEISSNER EFFECT

The Meissner effect is a property of superconducting materials in an external magnetic field which was discovered in 1933 by W. Meissner and R. Ochsenfield [39]. Meissner effect can distinguish a superconductor from a perfect conductor as depicted in Fig. 2. Consider small spherical samples of a superconductor and a perfect conductor are held at temperature, T, and placed in a small external magnetic field, B_{ext}. Initially, both samples are at temperature $T > T_c$ with a null external magnetic field, $B_{ext} = 0$ and then both samples are cooled to temperature, $T < T_c$. This process is known as Zero-Field Cooling (ZFC). Once the external field, H_a is turned on, both samples exclude the magnetic field lines from their interior, behaving as a perfect diamagnet. Conversely, If both materials are subjected to Field Cooling (FC) process, which cools both samples placed in non zero magnetic field, and when the temperature reaches $T < T_c$, the perfect conductor admits field lines in its interior, while the superconductor expels magnetic field.
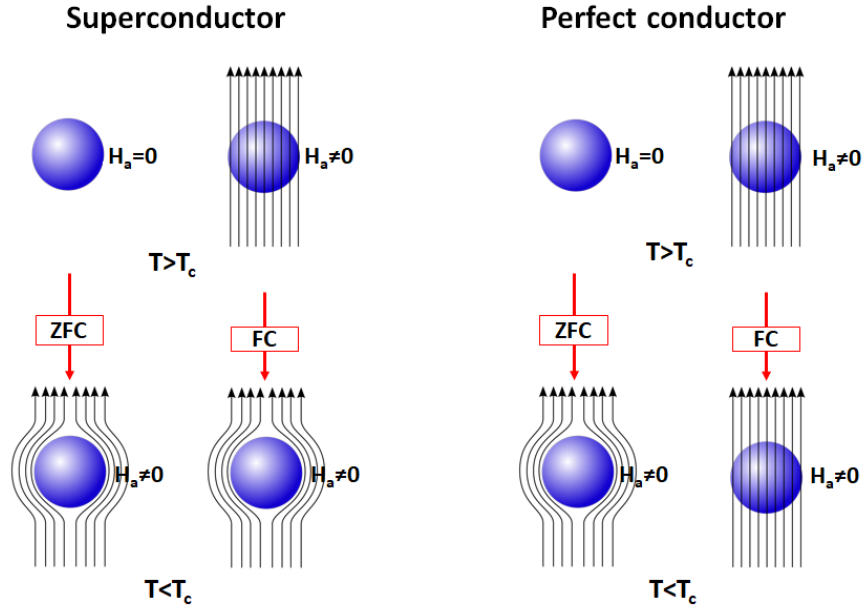
FIG. 2. A schematic view of the Zero-Filled Cooling and Field-Cooling processes for both a superconductor and a perfect normal conductor. Here H_a is the applied magnetic field. Adapted from [27].

To maintain perfect diamagnetism, screening currents arise on the surface and circulate to produce a magnetic field that is equal and opposite to the applied external field, leaving zero field inside the superconductor. These screening currents are simply described using Maxwell's equations. The total current is a combination of external currents (j_{ext}) and internal screening currents (j_{int})

$$j = j_{ext} + j_{int}. \tag{1}$$

The screening currents generates a magnetization in the sample per unit volume (M) defined by

$$\nabla \times M = j_{int}. \tag{2}$$

We can also define the external magnetic field (H_{ext}) in terms of j_{ext}

$$\nabla \times H = j_{ext}. \tag{3}$$

Following Maxwell equation, $\nabla \times B = \mu_o j$, the magnetic induction or magnetic flux density can be written as

$$B = \mu_o(H + M). \tag{4}$$

Where μ_o is the permeability of free space and has value of $4\pi \times 10^{-7} \text{NA}^{-2}$. Imposing the Meissner condition $B = 0$ in the equation (4), immediately leads to the magnetization,

$$M = -H. \tag{5}$$

The magnetic susceptibility is defined as

$$\chi = \frac{dM}{dH}\Big|_{H=0}. \tag{6}$$

For superconductors, $\chi = -1$.

Solids with a negative value of χ are called diamagnets. They are magnetized oppositely to the external magnetic field by screening out part of the external magnetic field. Since superconductors screen out the magnetic field from their interior, superconductors act as diamagnets.

In the Meissner state, the flux density does not fall abruptly to zero at the boundary of the superconductor but dies away within the region where the screening currents are flowing. This very thin region is called "penetration depth" (λ) and it is very small ($\sim 10^{-5}$

cm), but plays a very important role in determining the properties of superconductors. The London theory of superconductivity can be used to examine how a magnetic field penetrates a superconductor.

2.2 THEORIES OF SUPERCONDUCTIVITY

2.2.1 LONDON MODEL

The Meissner effect was well described in 1935 by Fritz and Heinz London [35]. They assumed that the supercurrent which screens the superconductor is carried by a fraction of the conduction electrons in the metal called superelectrons. Since the superelectrons have no friction, their equation of motion in an electric field is given by

$$F = m_e \frac{\partial \vec{v}}{\partial t} = eE. \tag{7}$$

Where m_e, v and e are the mass, velocity and charge of the electron respectively. The superconducting current (J_s) can therefore be given by

$$\vec{J_s} = en_s\vec{v}. \tag{8}$$

where n_s is the density of superelectrons. This immediately leads the equation

$$\frac{\partial \vec{J_s}}{\partial t} = \frac{n_s e^2}{m_e}\vec{E}. \tag{9}$$

This is the first London equation, which describes a perfect conductor. To derive second London equation, we can use Maxwell equation, $\triangledown \times \vec{E} = -\frac{\partial \vec{B}}{\partial t}$ and obtain

$$\frac{\partial}{\partial t}\left[\frac{m_e}{n_s e^2}\vec{\triangledown} \times \vec{J_s} + \vec{B}\right] = 0, \tag{10}$$

which represents the penetration of an externally applied magnetic field into the perfect conductor. As there is no resistance, Eq. (10) must be time independent, which leads to the equation

$$\left[\vec{\triangledown} \times \vec{J_s} + \frac{n_s e^2}{m_e}\vec{B}\right] = 0. \tag{11}$$

2.2.2 PENETRATION DEPTH

London equations can describe the screening behavior of the superconductor in the Meissner state by deriving an equation for the penetration depth, λ. Consider, a superconductor semi space $x > 0$, and the magnetic field B_o is applied in the z-direction. By inserting Eq. (11) into Maxwell equation $\vec{\nabla} \times \vec{B} = \mu_o \vec{J}_s$ and using the relation $\vec{\nabla} \times \vec{\nabla} \times \vec{B} = -\vec{\nabla}^2 \vec{B}$ ($\vec{\nabla} \cdot \vec{B} = 0$ due to Gauss's law), we can obtain the differential equation

$$\frac{d^2 \vec{B}_z}{dx^2} - \frac{\mu_o n_s e^2}{m_s} \vec{B}_z(x) = 0. \tag{12}$$

This equation can be solved with the solution

$$\vec{B}_z(x) = \vec{B}_o e^{-\frac{x}{\lambda_L}}. \tag{13}$$
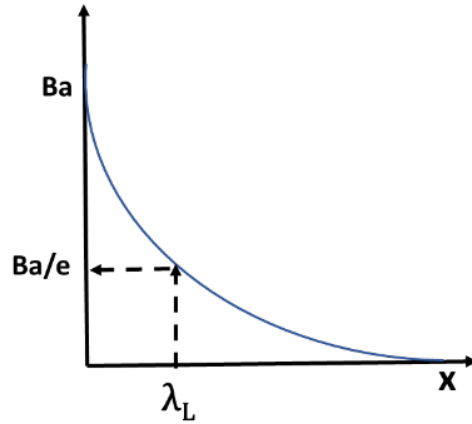
FIG. 3. The applied magnetic field, B_a near the surface of a superconductor in the Meissner state decays exponentially on a length scale given by the penetration depth, λ_L. Adapted from [27].

In a superconductor thicker than the penetration depth, the magnetic flux density decays exponentially as shown in Fig. 3. The thickness at which the magnetic field falls to $1/e$ of its value at the surface is called London Penetration depth, λ_L. This λ_L is defined as

$$\lambda_L = \sqrt{\frac{m_s}{\mu_o n_s e^2}}. \tag{14}$$

This tells that λ_L is independent of the strength of the magnetic field and the dimensions of the specimen, but this is true only for the bulk specimen.
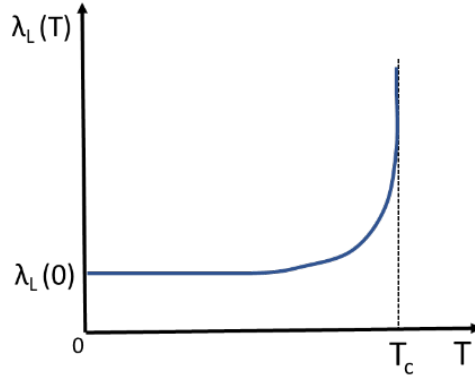
FIG. 4. The penetration depth, λ as a function of temperature. λ increases as the temperature increases and becomes effectively infinite at the critical temperature, T_c. Adapted from [27].

The number density of superconducting electrons depends on the temperature, so the penetration depth is temperature dependent. For $T \ll T_c$, all of the free electrons are superconducting, but the number density falls steadily with increasing temperature until it reaches zero at the critical temperature.

According to the London model

$$\lambda \propto n_s^{-1/2},$$

where n_s is the number of superconducting electrons. Therefore the penetration depth increases as the temperature increases and becomes effectively infinite at the critical temperature, T_c corresponding to a uniform field in the material at and above the critical temperature. Fig. 4 shows this temperature dependence of some superconductor, which is well represented by the expression

$$\lambda(T) = \lambda(0) \left[1 - \left(\frac{T}{T_c} \right)^4 \right]^{-1/2}. \tag{15}$$

London penetration depth of some superconductors at 0 K are given below.

TABLE 2. Penetration depth of some superconducting materials.

Element	Al	Cd	Hg	In	Nb	Pb	Sn	Tl	YBa$_2$Cu$_3$O$_7$
λ [nm]	50	130	38-45	64	47	39	51	92	170

2.2.3 COHERENCE LENGTH

A modified form of the London equation introducing the coherence length, ξ_o was later proposed by Pippard in 1953 [40]. Due to the incompatibility between experimental estimations of λ_L (0 K) and the values predicted London model, Pippard introduce a nonlocal generalization of Eq. 10 to address this discrepancy. He proposed the relation between the current at a point r in the solid, $J(r)$ and the vector potential at nearby points r' as

$$J(r) = \frac{3}{4\pi\xi_o} \frac{n_s e^2}{m_e} \int \frac{R[R.A(r')]e^{-R/\xi}}{R^4} dr', \tag{16}$$

where $R = r - r'$ that must have the characteristic dimension of coherence length, ξ and the presence of scattering was assumed related to that of pure material ξ_o by

$$\frac{1}{\xi} = \frac{1}{\xi_o} + \frac{1}{l}. \tag{17}$$

Here l is the mean free path of the electrons at the Fermi surface of the metal

$$l = v_F \tau. \tag{18}$$

with τ the scattering time from the Drude conductivity formula, and v_F, the electron band velocity at the Fermi surface.

The value of ξ_o could be estimated by using Heisenberg uncertainty principle ($\Delta x \geq \frac{\hbar}{\Delta p}$) argument to be

$$\xi_o = a\frac{\hbar v_F}{kT_c}.\tag{19}$$

Here a is a constant, which Pippard found for Sn and Al to be 0.15, and was later confirmed by the BCS theory which describes in next section to be 0.18 [41].

2.2.4 MICROSCOPIC THEORY OF SUPERCONDUCTIVITY

In 1957, a complete theory of superconductivity was established by Bardeen, Cooper, and Schreiffer, called the BCS theory [37, 38] that gives a microscopic description instead of the previous phenomenological macroscopical representations. This theory describes super-conductivity as a microscopic effect caused by a condensation of two electrons bound by a weak interaction that dominates over the repulsive Coulomb force, called "Cooper Pairs", first described by L. Cooper in 1956 [42].
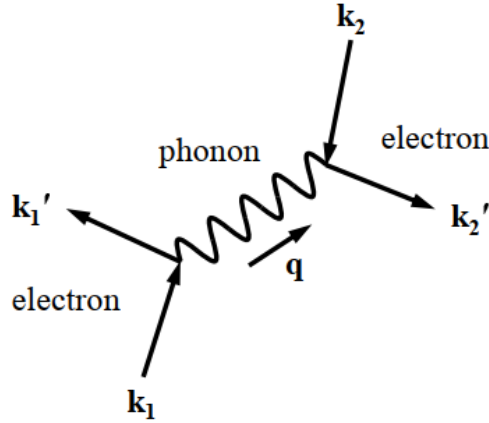
FIG. 5. Feynman diagram of electron-electron interaction transmitted by a phonon.

The Fermi-Dirac distribution describes that, at absolute zero temperature, electrons will fill up all available states up to the Fermi energy, E_F and they are constrained by the Pauli

exclusion principle. The volume of occupied states with radius, $p_F = \sqrt{2mE_F}$ in momentum space is often called the "Fermi Sea". When two electrons are added to a Fermi sea at absolute zero, Cooper pairs are formed from an interaction between electrons and a phonon (vibrational energy). Normally an electron would never be able to interact with another electron due to the repulsive effect of the Coulomb force, but in the crystal lattice, electron-electron interaction may occur through the exchange of a lattice phonon. When a single negatively charged electron with momentum k_1 slightly deforms the lattice of atoms in the superconductor drawing towards the small excess of positive charge and creates phonons of momentum, $q = k - k'$. This excess, in turn, attracts a second electron of momentum k_2. It is a weak, indirect attraction that binds the electrons together, into a Cooper pair as shown in Fig. 5. The distance between two paired electrons is the BCS coherence length, (ξ_0).
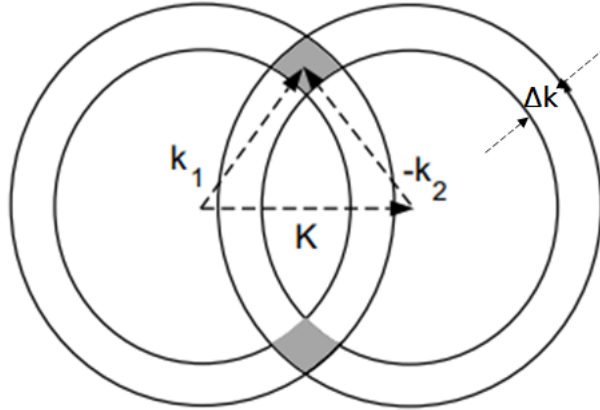
FIG. 6. Scatering shells of two electrons with Fermi radius, k_F and thickness Δk describe the pair of wave vectors k_1 and k_2. All pairs for which $k_1 + k_2 = K$ end in the shaded volume. The number of pairs k_1, k_2 is proportional to this volume in k space and maximum for $K = 0$.

Before and after scattering, the momenta of the paired electrons are within a range of $\Delta k = m\omega_n/\hbar k_F$, where ω_n is the average phonon frequency and k_F is the Fermi momentum. Thus, the scattering in phase space is restricted to a narrow shell of Δk. Both electrons are subjected to this restriction as schematically depicted in Fig. 6. The transition from (k_1, k_2)

state to (k_1', k_2') state satisfies the momentum conservation such as $k_1 + k_2 = k_1' + k_2' = K$, where K is a constant. This scattering is restricted to the overlap of the two scattering shells, clearly, this is negligible unless $K \approx 0$. Thus the interaction is most likely strongest if pairing electrons have equal and opposite momenta and spin, $k_1 = -k_2$ and $\sigma_1 = -\sigma_2$.

The importance of linking electrons into Cooper pairs is the fact that electrons are fermions (particles with non-integer spins), fermion must obey Pauli's exclusion principle which states that no two fermions with the same spin can occupy the same state. However, electrons with opposite spins in a Cooper pair add up to an integer spin of 0.

For two electrons in a Cooper pair in Fermi sea at absolute zero, the zero momentum wave function is of the form

$$\psi(r_1, r_2) = \sum_k g_k e^{ik(r_1 - r_2)} (|\uparrow_1 \downarrow_2\rangle - |\uparrow_1 \downarrow_2\rangle), \tag{20}$$

where g_k are weighting coefficients which are antisymmetric, $g_k = g_{-k}$ and $\uparrow$ and $\downarrow$ are up and down spin states of the electrons. By substituting this into Shrödinger equation $H\psi = E\psi$, the energy eigenvalue, E is given by

$$(E - 2\epsilon_k)g_k = \sum_{k' > k_F} V_{kk'} g_{k'}, \tag{21}$$

where ϵ_k are unperturbed plane wave energies and $V_{kk'}$ represents the matrix elements of the interaction potential.

$$V_{kk'} = \frac{1}{V} \int_v d^3 r V(r) e^{i(k-k').r}. \tag{22}$$

Here r is the distance between two electrons and V is the normalization volume. $V_{kk'}$ characterizes the strength of the potential for scattering a pair of electrons with momenta $(k', -k')$ to momenta $(k, -k)$. By assuming that $V_{kk'}$ is negative constant in whole energy range of interest, $V_{kk'}$ is simplified as

$$V_{kk'} = \begin{cases} -V_o & \text{for } E_F < \epsilon_k, \epsilon_k' < E_F + \hbar\omega_c, \\ 0 & \text{Otherwise,} \end{cases} \tag{23}$$

where V_o is the characteristic positive constant, E_F is the Fermi energy and ω_c is the cutoff frequency.

Since the density of states, N in the vicinity of E_F is the approximately constant, $N \sim N_o$ in the normal metal. By replacing sum by integration, Eq. 21 can be simplified as

$$(2E_F - E) = \frac{2\hbar\omega_c}{e^{\frac{2}{N_oV_o}} - 1} \approx e^{-2/N_oV_o}, \tag{24}$$

for $N_oV_o \ll 1$.

Then, the interaction energy of the Cooper pair can be written as

$$\delta E = E - 2E_F = -2\hbar\omega_c e^{-2/N_oV_o}. \tag{25}$$

In BCS theory, the superconducting ground state $|\psi\rangle$ is a common state of all Cooper pairs and it can be expressed by the product of the wave function of the individual Cooper pairs.

$$|\psi\rangle = \prod_k (u_k + v_k c^*_{k\uparrow} c^*_{-k\downarrow})|0\rangle, \tag{26}$$

where $|0\rangle$ is the vaccum state with no particles present. $|v_k|^2$ and $|u_k|^2$ are the probability that pair $(k\uparrow, -k\downarrow)$ is occupied and unoccupied respectively, $|u_k|^2 + |v_k|^2 = 1$.

Since electrons obey Fermi statistics, the creation operator, $c_{k\sigma}$ and annihilation operator, $c_{k\sigma\dagger}$ of momentum k and spin σ ($\uparrow$ or $\downarrow$) obey the characteristic commutation relations

$$\{c_{k\sigma}, c_{k'\sigma'}\} = \delta_{kk'}\delta_{\sigma\sigma'},$$

and

$$\{c_{k\sigma}, c_{k'\sigma'}\} = \left\{c^\dagger_{k\sigma}, c^\dagger_{k'\sigma'}\right\} = 0.$$

v_k^2 and u_k^2 can be written in terms of E_k

$$v_k^2 = \frac{1}{2}\left(1 - \frac{\xi_k}{E_k}\right), \tag{27}$$

$$u_k^2 = \frac{1}{2}\left(1 + \frac{\xi_k}{E_k}\right). \tag{28}$$

E_k is the excitation energy of a quasi-particle of momentum $\hbar k$ and it is defined as, $E_k = \sqrt{\Delta^2 + \xi_k^2}$, where Δ is essentially independent of k and hence, is the minimum excitation energy or "Energy Gap". It can be referred to as order parameter in the phenomenological theory. $\xi_k = E_k - E_F$ is the single particle kinetic energy relative to Fermi energy. Fig. 7 represents the graphical interpretation of Eq. (27), demonstrates that the interaction of the electrons with virtual phonons gives rise to an occupation of states above the Fermi energy, resulting in a kinetic energy of the system higher in the normal state. The difference between free energy of superconducting state and normal state is known as "Condensation Energy" and quantity Δ is the measure of condensation energy.
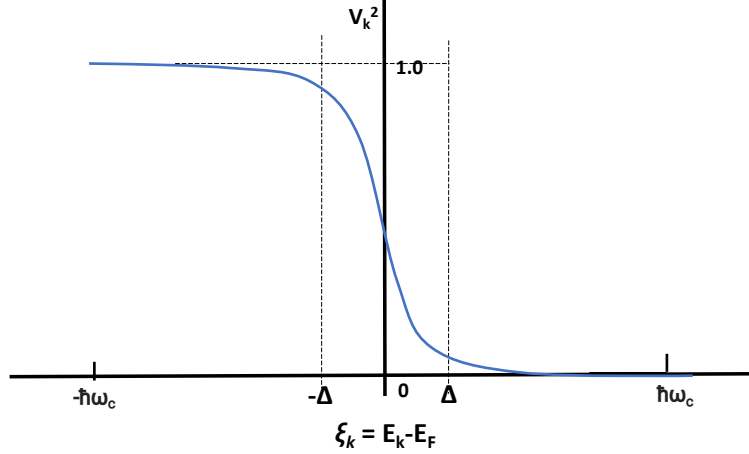
FIG. 7. BCS fractional occupation, v_k^2 as a function of electron energy, ξ_k measured from Fermi energy at absolute zero temperature. Adapted from [41].

Energy gap, Δ is given by

$$\Delta = \frac{\hbar\omega_c}{\sinh(\frac{1}{N_o V_o})} \approx 2\hbar\omega_c e^{-1/N_o V_o}.$$
(29)

This relation valid for weak coupling limit, $N_o V_o \ll 1$.

At a temperature greater than absolute zero, the superconductor can be excited above the ground state. The simplest conceivable excited state is a broken pair state in which only one state of the pair $(k' \uparrow, -k' \downarrow)$ is occupied and they behave almost like a free electron, generally called "quasi-particles". The common ground state of the Cooper pairs is separated from quasi-particle states by the energy gap Δ. Since two unpaired electrons are always created by breaking up one pair, minimum energy of $\delta E_{min} = 2\Delta$ is required to excite the superconductor.

The density of states of quasi-particles $N_s(E_k)$ is directly related to the density of the normal state, $N_n(E_F)$, since no state is lost in the superconducting transition.

$$\frac{N_s(E_k)}{N_n(E_F)} = \begin{cases} N_n(E_F)\frac{E_k}{\sqrt{E_k^2 - \Delta^2}} & \text{for } E_k > \Delta, \\ 0 & \text{for } Ek < \Delta. \end{cases}$$
(30)

In Fig. 8, the predicted density of states of quasi-particles is depicted. The density of states is diverged at $E_k = \Delta$ and it is merged with $N_s(E_F)$ for $E_K \gg \Delta$.
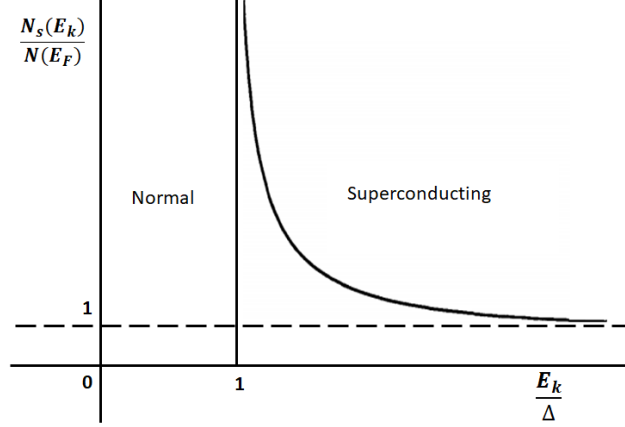
FIG. 8. Density of states of superconducting compared to normal state. The density of states is diverged at $E_k = \Delta$ and it is merged with $N_s(E_F)$ for $E_K \gg \Delta$. Adapted from [41].

Assuming quasi-particles obey Fermi-Dirac statistics, the probability of an excited state of k at a finite temperature is then given by

$$f(E) = \frac{1}{e^{(E-E_F)/\bar{k}T} + 1},\tag{31}$$

where $\bar{k}$ is the Boltzmann's constant and T is the absolute temperature. Since the probability of not formation of Cooper pairs is $2f$, the probability pair state is $1 - 2f$.

At the absolute temperature, $\Delta(0) \approx 1.764 k T_c$, due to electron-phonon interaction strength, this may differ from one material to another. The Δ also relates to characteristic coherence length as $\xi_o \approx \frac{\hbar \nu_F}{\Delta}$ which represents the spatial extension of a Cooper pair wavefunction. The BCS theory provides the expression for $\xi_o = 0.18 \frac{\hbar \nu_F}{k T_c}$ that is in good agreement with the equation determined by Pippard.

Fig. 9 shows the temperature dependence of the energy gap. Near absolute zero, the energy gap is approximately constant and decreases faster with increasing temperature. This relation can be formulated as

$$\frac{\Delta(T)}{\Delta(0)} = 1.74 \sqrt{1 - \frac{T}{T_c}}.\tag{32}$$
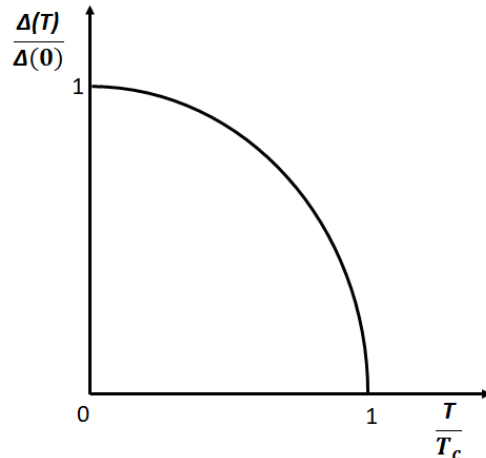
FIG. 9. Temperature dependence of normalized energy gap. Near absolute zero, the energy gap is approximately constant and decreases faster with increasing temperature. Adapted from [41].

2.2.5 GINZBURG LANDAU THEORY

Ginzburg-Landau (GL) theory, which was published in 1950 [36], provides an analytical description of superconductivity without examining the microscopic properties of superconductors. This plays a very important role in the analysis of superconductivity phenomena even after the emergence of BCS theory, which explains the microscopic behavior of superconductors. One of the key successes of the GL theory is its prediction of the distinction between type I and type II superconductors that have very different electromagnetic properties. Most importantly, GL theory is talking about the critical fields of both types of superconductors and flux penetration through quantized vortices in type II superconductors.

GL theory is based on second order phase transition and assumes that the free energy can be explained in terms of an order parameter $(\psi(\vec{r}))$. $\psi(\vec{r})$ is the microscopic wave function of the superconducting electrons and $|\psi|^2$ represents the density of superconducting charge carriers (n_s). According to the GL theory, the order parameter is small, varies slowly, and becomes zero at the transition temperature, T_c.

2.2.6 THE GL FREE ENERGY

The time dependent GL theory can be developed using thermodynamic arguments involving free energy shown in Fig. 10. When the temperature is above T_c, it must be energy wise favorable in a normal conducting state and the free energy function must have a minima at $\psi = 0$ since there exist no Cooper pairs in the superconducting sample.
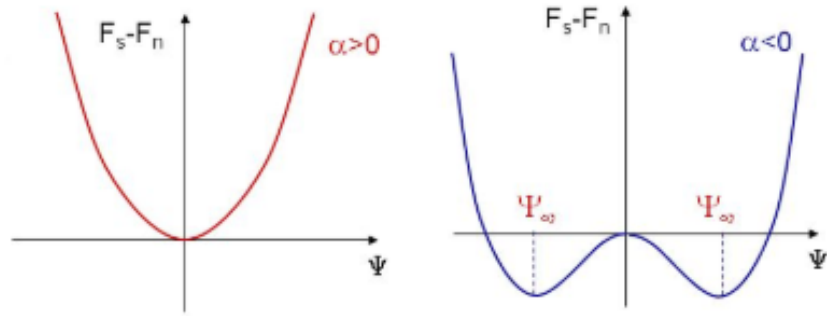
FIG. 10. Ginzburg-Landau free energy for $T > T_c(\alpha > 0)$ (left) and for $T < T_c(\alpha < 0)$ (right). Adapted from [41].

Contrary, when the temperature is below T_c, it must be favorable to be superconducting. In this case, the free energy function must have at least one minima when $\psi \neq 0$, and it may not have minima at $\psi = 0$.

In the absence of fields and gradients, the free energy can be written as

$$F_s = F_n + \alpha(T)|\psi|^2 + \frac{\beta(T)}{2}|\psi|^4, \tag{33}$$

where F_s and F_n are the free energy of the normal and superconducting states respectively. This is applicable when T is close to T_c and $\beta(T)$ is positive. $\alpha(T)$ is positive in normal state and negative in superconducting state. The equilibrium phase corresponds to a minimum i.e. $\partial F_s/\partial \psi = 0$. This leads to the condition $\alpha\psi_o + \beta\psi_o^3 = 0$ for the order parameter ψ_o at equilibrium. In normal state, minimum energy occurs at $|\psi|^2 = 0$ where as the minimum energy of superconducting state occurs when $|\psi|^2 = |\psi_\infty|^2 = -\frac{\alpha}{\beta}$, where ψ_∞ is the ψ at

infinity. When this value of ψ is substituted back to the Eq.21, one can find

$$F_s - F_n = -\frac{\alpha^2}{2\beta}. \tag{34}$$

Since α is positive when $T > T_c$ and negative when $T < T_c$, α can be defined as

$$\alpha(T) = \alpha(0) \left[\frac{T}{T_c} - 1 \right]. \tag{35}$$

In classical Landau theory, the order parameter is spatially invariant and a real quantity. In GL theory the microscopic wave function of the superconducting state $\psi(\vec{r}) = |\psi(\vec{r})|e^{i\varphi(\vec{r})}$ with $|\psi(\vec{r})|^2 = n_s$ where n_s is the density of superconducting electrons. Order parameter, $\psi(\vec{r})$ is not only a function of position but also it is included the magnetic field energy and the couping of the supercurrent to the magnetic field. When the magnetic field is present, the free energy density of superconducting can be expanded in a series of the form

$$F_s = F_n + \alpha|\psi(\vec{r})|^2 + \frac{\beta}{2}|\psi(\vec{r})|^4 + \frac{1}{2m^*}|(-i\hbar\nabla - e^*A)\psi(\vec{r})|^2 + \frac{1}{2}\mu_o H^2, \tag{36}$$

where m^* and e^* are twice the mass and charge of the electron respectively. The free energy of the normal state is given by same expression when $\psi = 0$. Third term can be written in more transparent form

$$\frac{1}{2m*}\left[\hbar^2(\nabla|\psi|)^2 + (\hbar\nabla\varphi - e^*A)^2|\psi|^2\right]. \tag{37}$$

The first term gives the extra energy associated with gradients in the magnitude of the order parameter. The second term gives the kinetic energy associated with supercurrents in a gauge-invariant form with φ as constant. It can be written as $n_s^*(\frac{1}{2}m^*v_s^2)$, where v_s is supercurrent velocity given by

$$v_s = \frac{p_s - e^*A}{m^*}, \tag{38}$$

where $p_s = \hbar\nabla\varphi$. In the absence of fields, currents or gradients, the free energy is minimized by having $\psi = \psi_\infty$ everywhere. On the other hand, when fields, currents and gradients are present, the minimum overall free energy is given by taking volume integral of Eq. (36) by considering $\psi(\vec{r}) = |\psi(\vec{r})|e^{i\varphi(r)}$. This leads to derive GL differential equations

$$\alpha\psi + \beta|\psi|^2\psi + \frac{1}{2m^*}(-i\hbar\nabla - e^*A)^2\psi = 0, \tag{39}$$

and

$$J = \frac{c}{4\pi}curl h = \frac{e^*\hbar}{2m^*i}(\psi^*\nabla\psi - \psi\nabla\psi^*) - \frac{e^{*2}}{m^*c}\psi^*\psi A, \tag{40}$$

or

$$J = \frac{e^*}{m^*}|\psi|^2(-i\hbar\nabla - e^*A) = e^*|\psi|^2 v_s. \tag{41}$$

2.2.7 GL CHARACTERISTIC LENGTHS

The Ginzburg-Landau theory contains two characteristic lengths, namely the penetration depth, (λ) and the GL coherence length, (ξ). To deduce the expression for λ, consider the specimen with dimensions much greater than this quantity. In the superconducting state, the magnetic field vanishes inside the sample and ψ is constant. By imposing $|\psi|^2 = -\frac{\alpha}{\beta}$ to Eq.40, the current density can be obtained as

$$j_s = \frac{4e^2}{m}\frac{|\alpha|}{\beta}A. \tag{42}$$

This current density is identical to that of in the second London equation and consequently, GL expression for penetration depth is given by

$$\lambda_{GL} = \sqrt{\frac{m\beta}{4\mu_o e^2 |\alpha|}}. \tag{43}$$

GL coherence length, $\xi(T)$, that describes the length scale of variations in the magnitude of ψ or the density of the superconducting electrons. To derive an expression for $\xi(T)$, we first consider a simplified case in which no fields are present, then $A = 0$. Second, we can take ψ to be real since the differential equation has only real coefficients. If we introduce a normalized wave function, $f = \frac{\psi}{\psi_\infty}$ where $\psi_\infty^2 = -\frac{\alpha}{\beta} > 0$, then Eq. (39) becomes

$$\frac{\hbar^2}{2m^*|\alpha|}\frac{d^2f}{dx^2} + f - f^3 = 0. \tag{44}$$

This makes it natural to define the characteristic length ξ for variation of ψ by

$$\xi_{GL} = \frac{\hbar}{\sqrt{2m^*|\alpha|}}. \tag{45}$$

Using the boundary conditions $f(0) = 0$, $\lim_{x\to\infty} f(x) = 1$ and $\lim_{x\to\infty} \frac{df(x)}{dx} = 0$. We finally obtain

$$f(x) = \tanh\frac{x}{\sqrt{2}\xi}. \tag{46}$$
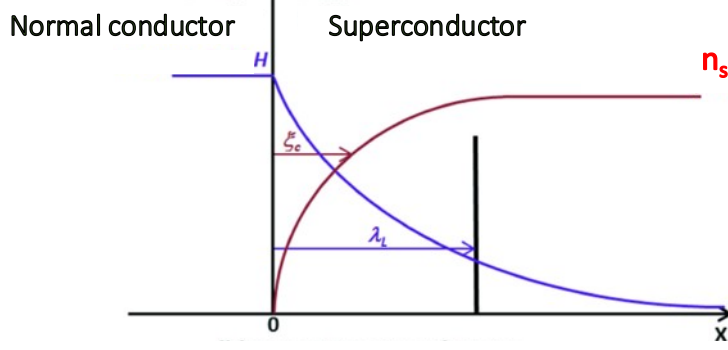
FIG. 11. Spatial variation of the magnetic field B and the Cooper pair density ns at a boundary between a normal metal and a superconductor. Adapted from [43].

As indicated in Fig. 11, the density of the Cooper pairs $n_s(x)$ increases steadily from zero at the phase boundary to its bulk value $n_s(\infty) = |\psi_\infty|^2$. This rise is characterized by the coherence length ξ. In this figure, the decay of the magnetic field, determined by the penetration depth, λ_L is also depicted. Because of the vanishing density of Cooper pairs close to the phase boundary, the curve flattens in this region.

It is also useful to introduce the famous dimensionless GL parameter κ, which is defined as

$$\kappa_{GL} = \frac{\lambda_{GL}}{\xi_{GL}}. \tag{47}$$

Since κ is a function of β only, it is temperature independent and is given by

$$\kappa = \sqrt{\frac{m^{*2}\beta}{2\mu_o\hbar^2 e^2}}. \tag{48}$$

If $\xi_{GL} > \lambda_L$ then the boundary has a positive surface energy (Type I superconductors), and negative when $\xi_{GL} < \lambda_L$ (Type II superconductors). The crossover κ_{GL} occurs at $1/\sqrt{2}$, such that:

- $\kappa_{GL} < 1/\sqrt{2}$ for Type I superconductors

- $\kappa_{GL} > 1/\sqrt{2}$ for Type II superconductors.

2.3 CRITICAL MAGNETIC FIELDS

Superconductivity is characterized both by zero resistance (perfect conductivity) and by the complete expulsion of magnetic fields (the Meissner effect). An increase in either temperature or magnetic flux density can destroy superconductivity and reinstate the normal conducting state. In the absence of an applied magnetic field, the temperature at the transition from the superconducting state to the normal conducting state (T_c) is independent of the shape or size of the sample. This is a well defined thermodynamic phase transition. For a given temperature, the maximum applied magnetic field strength at above mentioned phase transition refers to the critical magnetic field at that temperature. As temperature decreases, the critical field increases generally to a maximum at absolute zero. At the transition temperature, the strength of the critical field is zero.

2.3.1 THERMODYNAMIC CRITICAL FIELD, H_C

The superconducting state of material results from the pair formation of electrons interacting with valance bonds known as Cooper pairs at the Fermi energy. These pair bonds can be broken thermally or magnetically. When a magnetic field is applied to a superconductor, the Cooper pairs within the penetration depth of the surface form a supercurrent, J_s to expel the external field, and J_s increases the bulk free energy of the superconductor. If this additional free energy equals the binding energy, the pairs dissociate, the density of superconducting electrons is decreased while the density of normal electrons is increased, and eventually the material reverts to the normal phase [44]. The magnitude of the supercurrent at which the Cooper pairs break is known as the depairing current density (J_d). The magnetic field at this transition is known as the thermodynamic critical field (B_c).

We can use thermodynamics to deduce the formula for the critical magnetic field. The thermodynamic explanation is based on Gibbs free energy difference between two phases superconducting and normal (Fig. 12) [27]. Consider a superconducting specimen at temperature T and in absence of an applied magnetic field $(H_a = 0)$, the Gibbs free energy per unit volume of the superconducting state is g_s and that of in the normal conducting state g_n. When an external magnetic field, H_a is applied parallel to the superconductor, it acquires magnetization, M, and the change in free energy per unit volume

$$\Delta g(H_a) = g_s(T, H) - g_s(T, 0) = -\int_0^{H_a} MdH. \qquad (49)$$

In superconducting state, magnetization is negative and this change becomes

$$\Delta g(H_a) = \int_0^{H_a} |M| dH = \frac{1}{2}\mu_o H_a^2.$$

If the field strength is increased enough to raise free energy of normal conducting state (g_n) than that of superconducting state (g_s), metal becomes normal conducting. This happens when $g_s(T,H) > g_n(T,0)$, which gives

$$g_n(T,0) - g_s(T,0) < \frac{1}{2}\mu_o H_a^2.$$

Therefore a superconductor will be in superconducting state up to maximum magnetic field strength called critical field (H_c).

$$H_c(T) = \sqrt{\frac{2}{\mu_o}[g_n(T,0) - g_s(T,0)]}. \tag{50}$$

The critical magnetic field at any temperature below the critical temperature is approximately given by the relationship

$$H_c(T) = H(0)[1 - (T/T_c)^2]. \tag{51}$$

The $H(0)$ is the critical field at absolute zero.
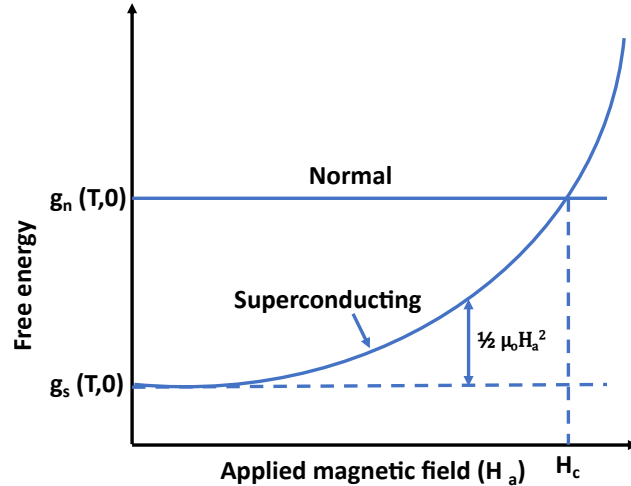
FIG. 12. The variation of Gibbs free energy of normal and superconducting states with applied magnetic field. Adapted from [27].

In the thermodynamic aspect, the magnetic field can penetrate the superconductor below H_c, creating a normal conducting layer with a thickness smaller than London penetration depth. Surface energy at the normal-superconducting boundary explains two types of superconductors named type I and type II, depending on how magnetic flux penetrates the material. Most pure elements such as Aluminum, Lead, and Mercury tend to be type I superconductors. To maintain superconductivity, both boundaries should have the same free energy. In the superconducting region, electrons arrange over a distance of ξ decreasing free energy, and the external magnetic field provides positive energy over λ. Inside the superconductor, both contributions cancel out, but at the boundary, if $\xi \gg \lambda$, there will be a net small positive energy. This type of metal is characterized as a type I superconductor. In contrast, in metals with $\xi \ll \lambda$, boundary energy is negative and allows partial flux penetration, characterized as type II superconductors [3].

In type I superconductors, superconductivity is abruptly destroyed when the strength of the applied field rises above a critical value H_c. This behavior is different from type II superconductors which exhibit two critical magnetic fields, H_{c1} and H_{c2}. The phase diagram of type I and type II superconductors is shown in Fig. 13.
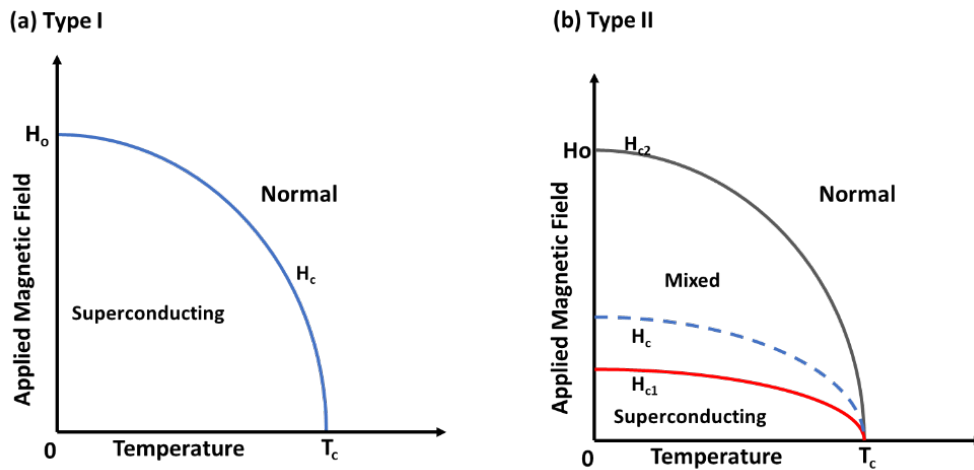
FIG. 13. Phase diagram of the superconductor : the variation of the applied magnetic field with the temperature in (a) type I and (b) type II Superconductors. Adapted from [45].

2.3.2 LOWER AND HIGHER CRITICAL FIELDS, H_{C1} AND H_{C2}

In type II superconductors such as niobium and alloys like Nb_3Sn, NbN, MgB_2, there exists a critical field called the lower critical field H_{c1}, above which magnetic field penetrates the superconductor in the form of a regular array of flux tubes known as vortices (Fig. 14). H_{c1} is the phase boundary where the equilibrium between having one vortex and no vortex in the superconducting state. Each vortex is enclosed in the quantized magnetic flux, $\phi_o = \frac{h}{2e} \approx 2 \times 10^{-15} Tm^2$. The center of the vortex has a normal conducting core and covers an area of roughly $\pi\xi^2/2$ [3]. This partial flux penetration refers to as the "vortex state" or since having both superconducting normal conducting regions "mixed state", or since the existence of vortices was predicted by Abrikosov, "Abrikosov state".

H_{c1} in terms of $\kappa_{GL} = \frac{\lambda}{\xi}$

$$H_{c1} = \frac{\phi_o}{4\pi\lambda^2} \ln(\kappa_{GL}) = \frac{H_c}{\sqrt{2}\kappa_{GL}} \ln(\kappa_{GL}). \tag{52}$$

Above H_{c1}, the vortices move into the material and the vortex flux density in the superconductor is increased. At a sufficiently large magnetic field, the density of superconducting electrons goes to zero and superconductivity breaks down. The field at which this complete superconducting-normal conducting transition is called the upper critical field, H_{c2}.

$$H_{c2} = \frac{\phi_0}{2\pi\xi^2} = H_c\sqrt{2}\kappa_{GL}. \tag{53}$$

Under the influence of an applied magnetic field, the change in the induced magnetic field inside the material, B and the magnetization, $M = (B/\mu_o - H)$ for both types of superconductors are distinguished in Fig. 15. The magnetic flux density inside a type I superconductor is zero up to H_c and increases with the increasing magnetic field. Magnetization increases with the magnetic field and drops to zero at H_c at which the magnetic field inside the material (B) is the same as the applied magnetic field (H). The magnetic flux density inside a type II superconductor is zero up to H_{c1} and increases in a higher field. At H_{c2} flux penetrates the whole of the material. (d) Magnetization increases with the magnetic field, peaks at H_{c1}, and then decreases to zero at H_{c2}. This process is reversible for pure ideal materials.
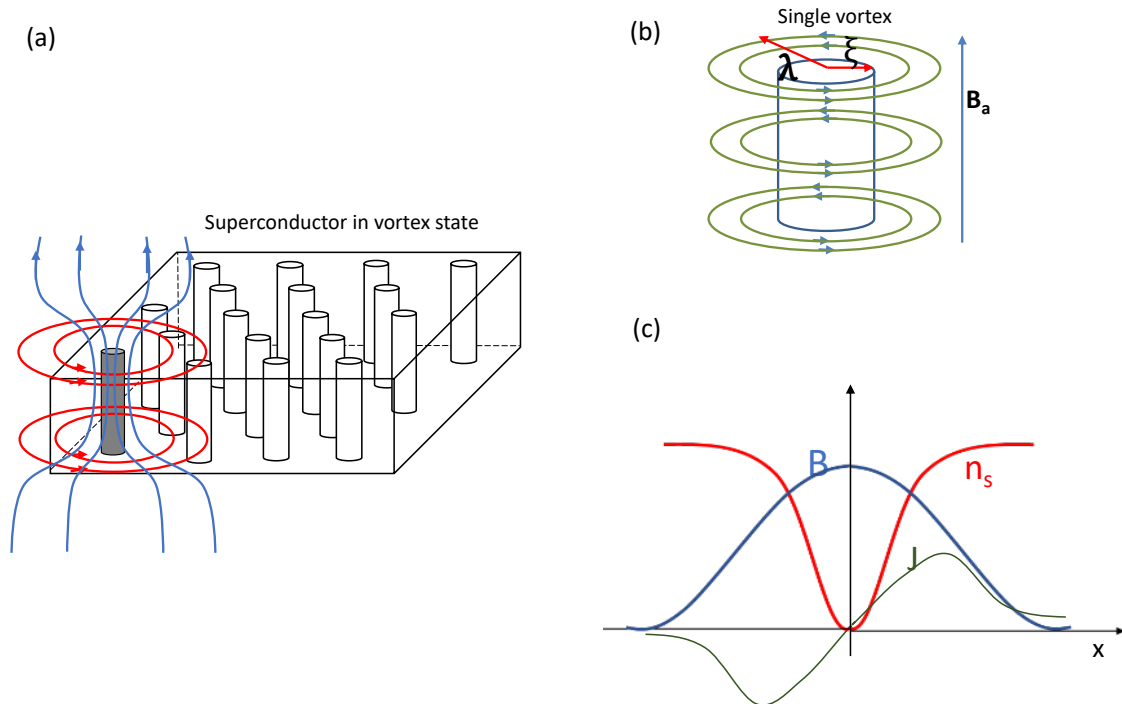
FIG. 14. Schematic diagram showing (a) magnetic flux penetrating a superconductor via vortices (b) single vortex having normal core with radius ξ and supercorrent around in radius λ and (c) the variation of B-field, superconducting electron density (n_s) and supercurrent (J) across the votex as a function of distance from the center of vortex. (a) and (c) are adapted from [46].
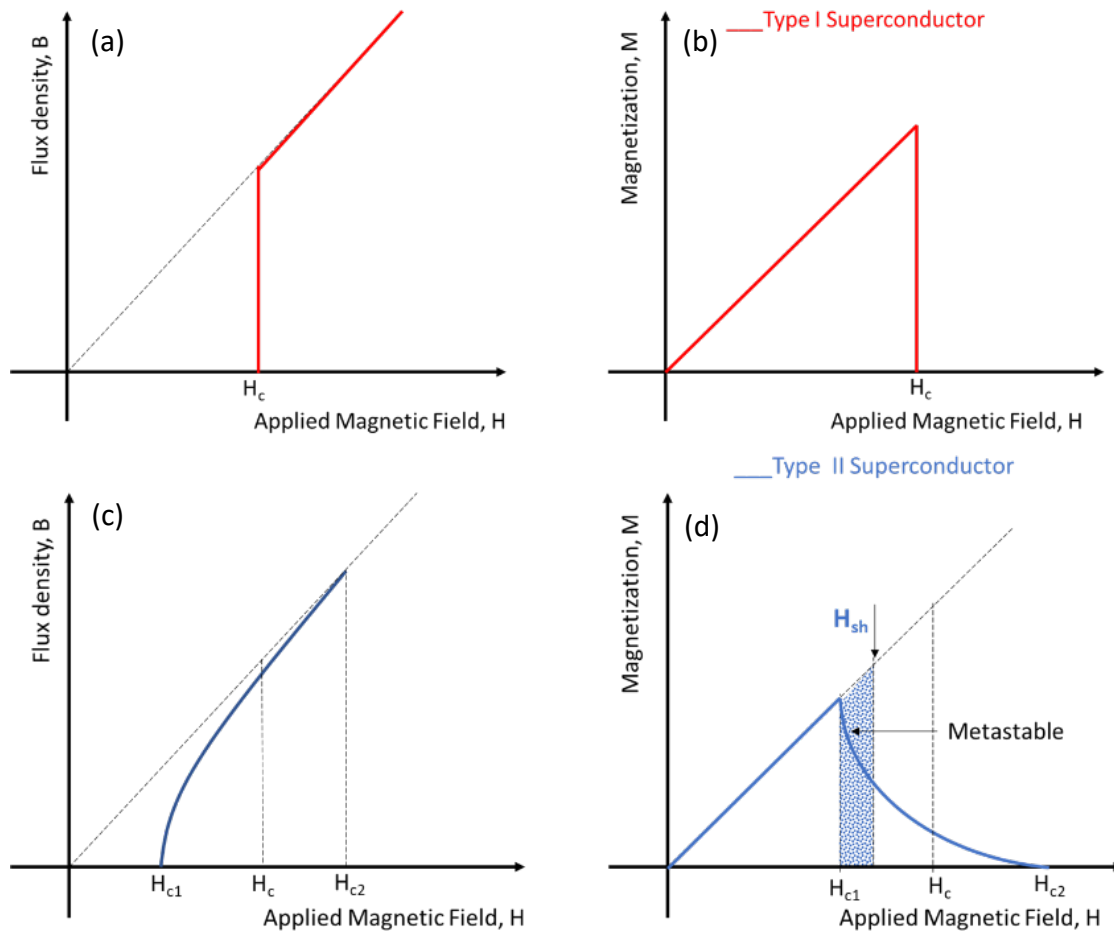
FIG. 15.   The behaviour of type I and type II superconductors in an external magnetic field(a) The magnetic flux density inside a type I superconductor is zero up to H_c and increases in higher field (b) Magnetization increases with magnetic field and drops to zero at H_c (c) The magnetic flux density inside a type II superconductor is zero up to H_{c1} and increases in higher field. At H_{c2} flux penetrates completely through the material. (d) Magnetization increases with magnetic field, peaks at H_{c1} and then decreases to zero at H_{c2}. This process is reversible for pure ideal materials. Adapted from [43].

2.3.3 SUPERHEATING FIELD, H_{SH}

At H_{c1}, the bulk of type II superconductor is energetically favorable for flux to be inside it, but flux penetration will not necessarily occur in this field. It is because of the energy barrier, the so-called Bean-Livingston barrier that prevents penetration of vortices through the surface of the material [47]. The superconductor will stay superconducting until this barrier breaks down at the external magnetic field, $H_o > H_{c1}$. This scenario is discussed in [47] by interpreting the interaction between a vortex and the superconducting surface as a possible explanation for experimental data.

Consider an ideally smooth surface of a superconductor with an isolated vortex in the interior, parallel to the surface and center of the vortex at x_o. Until the vortex appears, surface current induces to cancel out the external magnetic field, which can be represented by an "image vortex" outside the surface and it provides an attractive force to the surface (Fig. 16(a)).
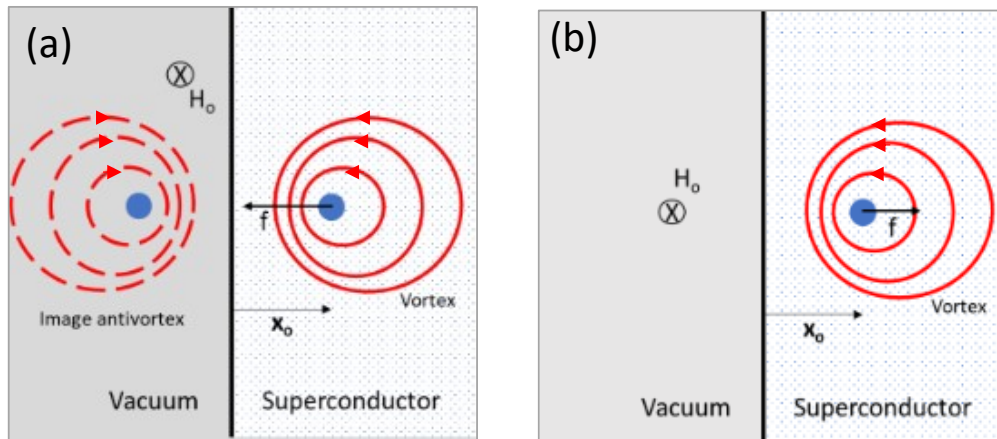
FIG. 16. Schematic representation of the forces on a vortex near a superconducting surface (a) attractive force produced by an image vortex of opposite sign (b) repulsive force from interaction with the surface fields. Adapted from [48].

$$f_{image} = \phi_o \frac{dH_{image}}{dx}, \tag{54}$$

where H_{image} is the field generated by the image force.

A repulsive force is then exerted on vortex due to the external field which is in the same sign as the field of vortex (Fig. 16(b)).

$$f_{ext} = \phi_o \frac{H_o}{\lambda} e^{-\frac{x_o}{\lambda}}. \tag{55}$$

Then the Gibbs free energy of this two contributions

$$G = -\int f dx = -\int (f_{ext} + f_{image}) dx, \tag{56}$$

$$G = -\phi_o H_{image}(2x_o) + \phi_o H_o e^{(-\frac{x_o}{\lambda})} + const. \tag{57}$$

At $x_0 \longrightarrow \infty$ the first two terms are zero and

$$const = G(\infty) = \phi_o(H_{c1} - H_o).$$

The Gibbs free energy can be written as

$$G = \phi_o \left[-H_{image}(2x_o) + H_o e^{(\frac{-x_o}{\lambda})} + H_{c1} - H_o \right]. \tag{58}$$

Fig. 17 represents the change in Gibbs free energy of an isolated vortex. As the external magnetic field, H_o increases, the energy barrier shrinks but does not disappear and the vortex is still unable to penetrate the ideal superconducting sample surface at H_{c1}. This means that the superconductor remains in the Meissner state above H_{c1}, which is now metastable and can be referred to as a superheated Meissner state. The field at which the barrier vanishes is called the superheating field, H_{sh}. At this field, the shielding currents become large enough to push away a vortex from its "mirror image" and push it inside the sample. This superheating field, H_{sh} defines the theoretical field limit of the superconductor. However, the actual material surface involves a tremendous number of material and topographic defects which reduce the energy barrier, causing local penetration of vortices at the field $H_{c1} < H_o < H_{sh}$ or even at $H_o < H_{c1}$. Special preparation and polishing of the surface are required for the barrier to be observed in ordinary superconductors such as niobium.
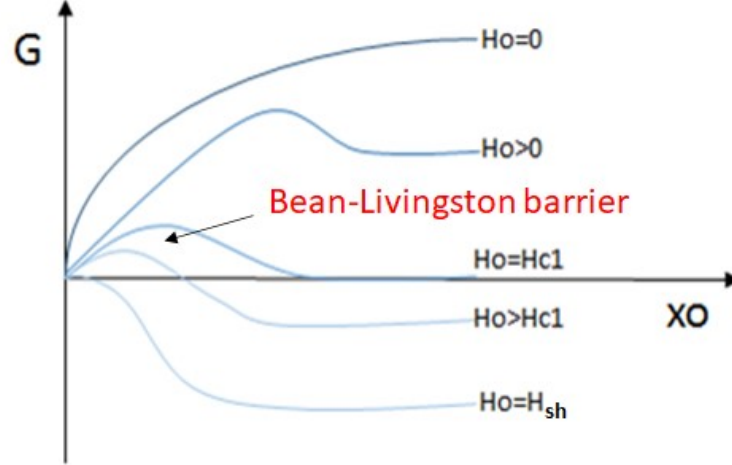
FIG. 17. Gibbs free energy of an isolated vortex as a function of its distance from the surface for different values of applied field, H_o. Adapted from [48].

The Superheating field depends on temperature dependent material properties: penetration depth (λ) and coherence length (ξ). Solving GL equations for the half space superconductor in one dimension under parallel surface magnetic field H_{sh} has been calculated in [49] and dependency of H_{sh} on $\kappa_{GL} = \lambda/\xi$ is represented in [3] as

$$
\begin{aligned}
H_{sh} &\approx \frac{0.84}{\sqrt{\kappa}} H_c, \ \kappa_{GL} \ll 1, \\
H_{sh} &\approx 1.2 H_c, \ \kappa_{GL} \approx 1, \\
H_{sh} &\approx 0.745 H_c, \ \kappa_{GL} \gg 1.
\end{aligned}
\tag{59}
$$

2.3.4 SURFACE CRITICAL FIELD, H_{C3}

The behavior of the top thin layer of the superconductor under a magnetic field is different than in bulk. In 1963, Saint James and de Gennes showed that the existence of a thin superconducting sheath near the surface of the superconductor within thickness ξ is possible above H_{c2} up to $H_{c3} = 1.695 H_{c2}$ in the parallel applied field on the surface [50]. At the field, H_{c2}, the bulk superconductor is in the normal phase. When the applied magnetic field is perpendicular to the surface, $H_{c3} = H_{c2}$.

CHAPTER 3

SUPERCONDUCTING RF CAVITIES

Superconducting RF cavities are the devices that use to accelerate charged particle beams by transferring RF energy. When RF power is applied to a cavity close to its resonant frequency, it builds up large electromagnetic fields. The electric field that is generated accelerates the beam as it passes through the cavity, but a magnetic field is also produced, which interacts with the superconductor on the cavity surface. For sufficiently large magnetic fields, the superconductor will quench at which the cavity transitions from a superconducting state to a normal conducting state, causing the loss of the stored energy within the cavity.

3.1 FUNDAMENTALS

The several important figures of merit that are used to evaluate cavity performances will be discussed in detail. The cavity accelerating voltage V_c is the ratio of the maximum energy gain that a particle moving along the cavity axis can achieve to the charge of that particle. The accelerating gradient is defined as the ratio of the accelerating voltage per cell V_c to the cell length. The optimal length of the cavity cells is typical $\beta\lambda/2$ where β is the ratio between the velocity of charged particles and light, v/c. The accelerating gradient is

$$E_{acc} = \frac{V_c}{\frac{\beta\lambda}{2}}. \tag{60}$$

The E_{acc} is proportional to the peak surface magnetic field, H_p that is the maximum possible magnetic field at the cavity wall with no flux penetration.

The RF power dissipation in a cavity wall is characterized by the quality factor Q_o, which tells us how many RF cycles are required to dissipate the energy U stored in the cavity.

$$Q_o = \frac{\omega_o U}{P_c} = \frac{\omega_o \mu \int_v |H(r)|^2 dV}{\oint R_s |H(r)|^2 dA}, \tag{61}$$

where P_c is the RF power dissipated in the cavity. The RF magnetic field $H(r)$ for the excited eigenmode with angular frequency $\omega_o = 2\pi f_o$ is integrated over the cavity volume V and surface A. The surface resistivity R_s quantifies the RF power and depends only on the frequency and intrinsic material properties. It remains the only term in the formula

that is material dependent, making it convenient to write the quality factor in terms of the geometry factor G as

$$Q_o = \frac{G}{\langle R_s \rangle}. \tag{62}$$

The surface resistance is a function of the RF magnetic field and may therefore vary along the cavity wall. It must be averaged over the cavity surface. R_s values ranging from -1 to 10 nΩ and corresponding Q values between 10^9 and 10^{11} has been achieved with SRF cavities. The geometry factor G is determined only by the shape of the cavity and hence is useful for comparing cavities with different shapes. The cavity's shunt impedance R_{sh} relates the dissipated power P_c and the accelerating voltage

$$P_c = \frac{V_c^2}{R_{sh}}. \tag{63}$$

A related quantity is the geometric shunt impedance R_{sh}/Q_o, or simply R/Q, which depends only on the cavity's shape. It can be formulated as

$$\frac{R_{sh}}{Q_o} = \frac{V_c^2}{\omega_o U}. \tag{64}$$
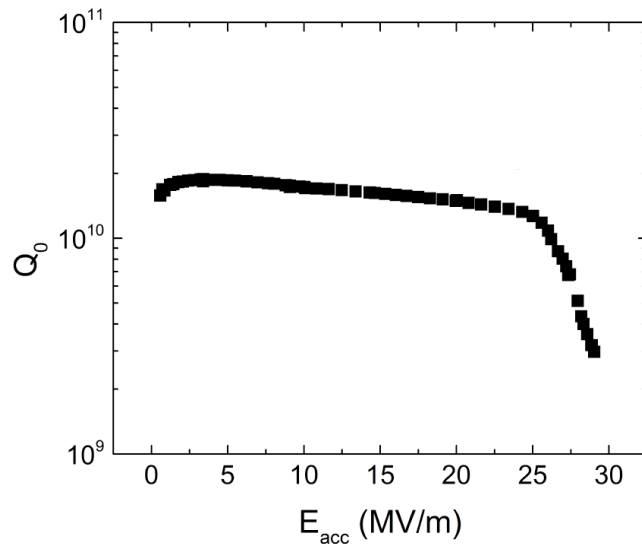
FIG. 18. The quality factor versus accelerating gradient for typical electropolished cavity.

For a good cavity design, geometric shunt impedance should be maximized. The power loss is

$$P_c = V_c^2 \frac{R_s}{(R_{sh}/Q_o)G}. \tag{65}$$

Maximizing both R/Q and G during cavity design leads to low RF power dissipation.

Basically, the performance of a cavity can be evaluated during cavity testing using only two figures of merits, quality factor, Q_o, and accelerating gradient, E_{acc}. In a cavity testing quality factor, Q_o is measured while increasing input power, and the test result is plotted against a calculated accelerating gradient, E_{acc} or an equivalent magnetic field B_p on the inner surface of the cavity (Fig. 18).

The ratios of the peak surface electric and magnetic fields to the accelerating gradient, E_{pk}/E_{acc} and B_{pk}/E_{acc} are the crucial parameters of cavity performances. A high surface electric field can cause field emission of electrons that deteriorate performance. A high surface magnetic field limits the accelerating gradient at which the breakdown of superconductivity, also called quench [3].

SRF cavities are designed mainly for accelerator applications and SRF properties. Depending on the application, cavity design needs to be based on some choices such as cavity frequency, cell shape, number of cells, beam aperture, operating gradient, operating temperature, input coupler, and Higher-Order Mode (HOM) coupler types [3].

3.2 LIMITATIONS

The main goal in the RF design of a superconducting cavity is to get a higher accelerating gradient and a lower power dissipation, which are determined by lower peak surface fields (E_{pk}/E_{acc} and B_{pk}/E_{acc}) and a higher $G(R/Q_o)$. There are some defining fundamental limits for the maximum expected gradients based on the maximum expected surface magnetic fields and electric field dependent phenomena that determine the maximum gradient and Q_o of cavities. Fig. 19 illustrates the decrease of cavity performances due to some mechanisms such as residual losses, multipacting, field emission, and thermal breakdown.
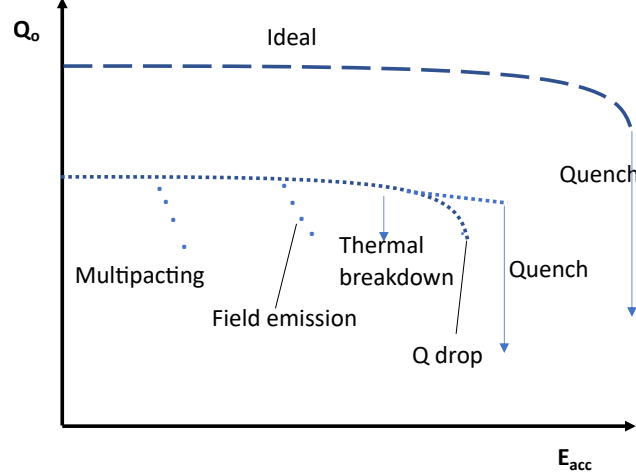
FIG. 19. The main mechanisms which limit the SRF cavity performances such as residual losses, multipacting, field emission, and thermal breakdown. Adapted from [51].

3.2.1 RESIDUAL LOSSES

Residual losses affect lot to degrade the quality factor of the cavity. The surface resistance, R_s can be broken up into two components; a temperature dependent BCS resistance (R_{BCS}) and temperature independent residual resistance (R_{res}).

$$R_s = R_{BCS} + R_{res}. \tag{66}$$

R_{BCS} is exponentially decreasing at lower temperatures, so quality factor would be infinitely high at 0 K, if only contribution to R_s would be due to the losses caused by oscillating quasi particles as calculated using the BCS theory. Temperature independent R_{res} limits the experimental Q_o at lower temperatures. Residual losses arise from several mechanisms including losses from trapped magnetic flux, hydrides and oxides [1, 52].

Ether Earth's magnetic flux or DC current surrounded around cavity causes to trapped magnetic flux which gives major contribution to R_{res}. It can be estimated as

$$R_{res} = \alpha H_{dc} \sqrt{f}, \tag{67}$$

where f is in the units of GHz and H_{dc} is the residual DC magnetic field. $\alpha =$ 0.2-0.3 nΩ/mG for Nb at GHz frequencies [1].

Another mechanism that contributes to residual losses is hydride formation by a chemical reaction between hydrogen on niobium walls and niobium. This is known as hydrogen Q-disease, which grows more seriously with the slow cooling down of the cavity. Rapid cooling down may not cause Q disease. The surface of niobium is covered with a 3-5 nm thick native oxide layer. the surface structure and chemical identity of the oxide layer directly affect to SRF cavity performances due to R_{res} contribution of dielectric losses and electric interface losses [1, 53].

3.2.2 MULTIPACTING

Multipacting is another performing limiting phenomenon in SRF cavities. It is a resonant process that leads to generating a large current with in a small region of the cavity and restricts the increase of cavity fields by rising the incident power. As a result, heat is generated at certain locations of the cavity surface which can cause quench of the SRF cavity. Then, the quality factor of the cavity is decreased very sharply and a low acceleration gradient is achieved.

Multipacting (multiple impact electron amplification) is generally triggered by an electron emitted from a cosmic ray, photoemission, or impacting field emission electrons. The emitted electron gets energized by the RF field inside the cavity and interacts with the cavity wall, consequently generating secondary electrons from a cavity surface. the number of secondary electrons depends on the surface characteristics and on the impact energy of the primary electron. If the secondary electrons synchronized with the RF field and produce more electrons, it increases exponentially to a very high value within a few RF cycles.

The number of electrons emitted after k^{th} impact with the cavity, N_e can be represented in terms of function $\delta(K)$ as

$$N_e = N_o \prod_{m=1}^{k} \delta(K_m),$$
(68)

where N_o is the number of initial secondary electrons and K_m is the kinetic energy at the mth impact.

After several impacts, electrons tend to return to their original position and this is referred to as "n-point multipacting", where n is the number of impact sites along the electron trajectories. For the $\beta = 1$ cavities, one-point multipacting is very common. The number of Rf periods required by electrons to return the point of origin is called "multipacting order". In $\beta = 1$ cavities, two-point multipacting usually originated between opposite points of the equator. Analytical analysis of multipactig is explained properly in Ref. [1]. Multipacting

can be avoided by carefully selecting the proper shapes of cavities including the input coupler and output coupler.

3.2.3 FIELD EMISSION

Electron field emission limits the accelerating gradient in superconducting cavities. When exposed to an intense, properly oriented electric field, a conducting surface can emit electrons and these electrons are accelerated by the RF field in the accelerating cavity. In a superconducting cavity, even the small additional dissipation of RF power due to the electron loading of the cavity may correspond to significant and undesirable degradation of the cavity Q-value, and an increase of the cavity cryogenic consumption.

Some experiments show that presence of the microparticle contaminants, and surface scratches with sharp features inside the cavity trigger field emission. Hence the cleaning of rf cavities by High Pressure Rinse (HPR) and assembly under class 10-100 clean room conditions can prevent the field emission [3].

3.2.4 THERMAL BREAKDOWN

The thermal breakdown is one of the main limitations to reach high accelerating fields in the SRF cavity. This is also known as "quench". This starts from micro regions of cavity surface that have higher rf losses than surface resistance for an ideal superconductors, so-called "defects", where vortices that locally penetrate and develop into a thermomagnetic flux avalanche. This continues until the temperature of a part or all of the RF surface exceeds the critical temperature, and eventually causes a quench, thereby coming to normal conducting state and rapidly dissipating all stored energy in the cavity fields.

3.2.5 HIGH FIELD Q-SLOPE

The performance curve of the SRF cavity in GHz range Q vs E_{acc} shows three distinct regions depending on E_{acc} values.

- Below 5 MV/m - low-field Q-slope

- Up to 20-30 MV/m - medium field Q-slope

- Above - High field Q-slope.

At the highest fields ($\sim$ 80-100 mT), the quality factor starts to decrease rapidly even in the absence of field emission. This is known as high field Q-slope and eventually causes

the breakdown of the cavity. High field Q-slope typically arises in the cavity prepared by buffered chemical polishing (BCP) or electropolishing (EP). This can be improved by mild baking (at 100-120 ^{o}C for 48 hrs). Exposure to dust free air during baking removes water and hydrocarbons on the cavity wall coming from the wet treatments [3].

CHAPTER 4

MATERIALS FOR SRF CAVITIES

4.1 LOOKING BEYOND NIOBIUM

Over the past few decades, bulk niobium (Nb) is the only material of choice for Super-conducting Radio Frequency (SRF) cavities used in particle accelerators. With the highest critical temperature ($T_c = 9.25$ K) and the highest lower magnetic field (H_{c1} (0 K)=180 mT) of Nb, lower RF losses, and higher accelerating gradients have been achieved. In addition, it is relatively reliable in fabrication. Many possible compounds with higher critical temperatures than Nb have been explored, but none of these materials can reach Nb in terms of its performance with increasing RF fields or its ease of use for accelerator applications. With the continuous improvement of the RF performance of bulk Nb cavities, they can achieve extremely high quality factors $Q_o \sim 10^{10} - 10^{11}$ and accelerating fields up to $E_{acc} \sim 50$ MV/m at 1.3–2 K and 1–2 GHz with rf peak breakdown field up to 170–180 mT [1] which is close to the thermodynamic critical field of Nb, $H_c = 200$ mT. Further improvement will be difficult to achieve with bulk Nb, which leads to looking beyond materials and structures other than Nb.

4.2 MATERIALS OTHER THAN NIOBIUM

Selected alternative SRF cavity materials should have both fundamental and technological requirements.

- Low surface resistance, R_s

$$R_s = R_{BCS} + R_{res}.$$

BCS resistance, R_{BCS} is depends on the temperature and the BCS theory predicts that high T_c materials are good in RF applications. Those materials also should be a good conductor in the normal phase with low resistivity, ρ_n for low R_{BCS} [11].

Residual resistance, R_{res} never vanishes, typically in several nΩ. R_{res} is not yet understood clearly but possible mechanisms of origin are mentioned in literature such as rough

surface, metallic inclusions, chemical residues or surface defects, and flux trapped during cooling. Since, $R_{res} \propto \rho_n$, the one with the lower ρ_n should have the smallest residual resistance [11].

- High lower critical magnetic field, H_{c1} and high superheating magnetic field H_{sh}

At H_{c1}, magnetic flux can start to penetrate inside the materials destroying the Meissner state, but it can persist metastably up to H_{sh}, which defines the theoretical field limit of the SRF breakdown (Chapter 2). Higher H_{c1} and H_{sh} are required to lead SRF cavity towards higher E_{acc}.

- High thermal conductivity to transfer the RF power through the cavity wall [20].

By looking at the material requirements, several materials as potential candidates for SRF applications can be considered.

- B1 Nb compounds such as NbN and NbTiN

- A15 compounds such as Nb_3Sn, Nb_3Al, Nb_3Ga, Nb_3Ge, V_3Ga, V_3Si, Mo_3Re

- Magnesium Diboride, MgB_2

- Oxipnictides

The superconducting parameters $(T_c, \rho_n, H_{c1}, H_c, H_{c2}, \lambda, \Delta$ and $\xi)$ of above mentioned materials are listed in Table 1 in Ref [11].

Since clean Nb is the highest B_{c1} and B_{sh} among elemental superconductors, almost all above materials have B_{c1} lower than that of Nb, which causes premature flux penetration at the lower field compared to Nb. Real superconductors with material and topographic defects reduce the energy barrier, causing local penetration of vortices sometimes well below B_{c1}. In particular, at a temperature as low as that required for SRF operations, vortices that locally penetrate at such a weak spot would develop into a thermomagnetic flux avalanche and eventually cause a quench. To address this problem A. Gurevich proposed a multilayer structure in Ref. [13].

4.3 SIS MULTILAYER SYSTEM

The multilayer structures are comprised of alternating layers of superconductors (S) and insulators (I) fabricated on bulk Nb as shown in Fig. 20. Its main idea is to delay thermomagnetic avalanches caused by a local penetration of vortices at defects and not to allow

them to develop into avalanches.The type II superconductor candidates with $T_c > T_c(\text{Nb})$ and $B_{sh} > B_{sh}(\text{Nb})$ such as Nb$_3$Sn [54], NbN [55], NbTiN [56], MgB$_2$ [57] and some Fe-based superconductors could potentially enhance the surface field at the onset of vortex penetration, B_p above B_{c1} of Nb. The thickness of the layer should be smaller than the London penetration depth (λ) of that material.

Strong enhancement of B_{c1} of thin film with thickness d $< \lambda_L$ in parallel external field predicted by Abrikosov [58, 59] is given by

$$B_{c1} = \frac{2\phi_o}{\pi d^2} \ln \frac{d}{\xi}, \tag{69}$$

where Φ_o is the flux quantum and $\xi = 1.07\xi_o$. For example, for a 20 nm NbN thin film with $\xi_o = 5$ nm has a $B_{c1} = 4.2$ T [13].

The I layer is an important feature in the SIS structure, which prevents both the propagation of vortices and localizes dissipation in the S layer. I layer can be a few nanometers in size to suppress the Josephson coupling between S layers [13, 14].
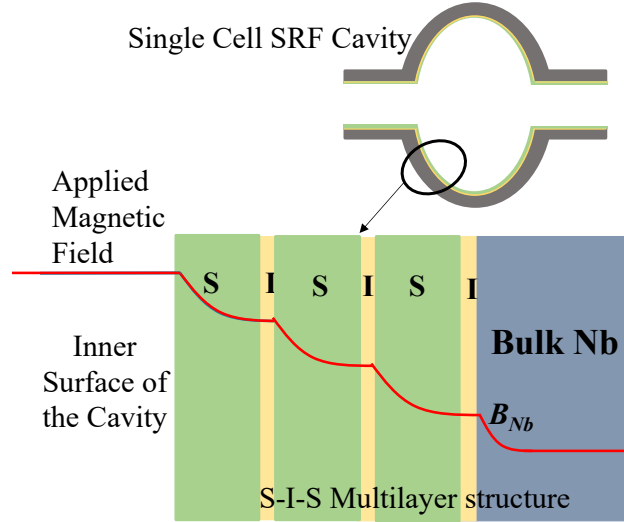
FIG. 20. Multilayer coating consisting of thin ($d < \lambda$) layers of superconductors with high H_{sh} separated by thin dielectric layers deposited on the inner surface of the Nb cavity. Inner red curve: Increase of peak surface magnetic field at each layer.

The surface resistance is also strongly reduced because the superconducting materials used have higher gap $\Delta(\text{Nb}_3\text{Sn}, \text{NbN}\dots)$ than Nb because $R_s \propto \lambda^4 \exp(-\frac{\Delta}{k_B T})$ [20]. With such structures, the quality factor could be increased two orders of magnitude above Nb values.Moreover, high field performance of Nb cavities can be achieved not only by using superconductors with higher H_{sh} but also Nb-I-Nb multilayer structure which can increase quality factor by a significant amount.

4.3.1 MAXIMUM SCREENING FIELD

The maximum H_m can be reached at an optimum multilayer thickness

$$d_m = \lambda \ln(\mu + \sqrt{\mu^2 + k}), \tag{70}$$

where

$$\mu = H_{sh}\lambda/(\lambda + \lambda_o)H_{sho},$$

and

$$k = (\lambda - \lambda_o)/(\lambda + \lambda_o) > 0.$$

μ and k depend on the materials parameters of S layers and the substrate. The optimized SIS multilayer can screen the field exceeding both superheating fields of layer material H_{sh} and substrate (Nb) H_{sho} [14] given by

$$H_m = \left[H_{sh}^2 + \left(1 - \frac{\lambda_o^2}{\lambda^2}\right)H_{sho}^2\right]^{1/2}, \tag{71}$$

λ is the penetration depth of layer material and λ_o is that of substrate (Nb). H_m exceeds both H_{sh} and H_{sho} if $\lambda > \lambda_o$.

For example for a dirty Nb_3Sn ($H_{sh} = 0.84H_c$= 454 mT) layer on Nb ($H_{sho} = 240$ mT and $\lambda_o = 40$ nm) yields $H_m = 507$ mT at $d_m = 132$ nm, which tells that the Meissner state persists up to the field 12% higher than H_{sh} of Nb_3Sn [14].

The enhancement of H_m does not necessarily require I layers if there is a dirty layer at the surface, λ increases due to a shorter mean free path, l according to the relation $\lambda \sim \lambda_o(\xi_o/l)^{1/2}$. For instance, a dirty Nb layer with $l = 2$ nm has $\lambda = 180$ nm and $\xi = (l\xi_o)^{1/2} = 9$ nm, using $H_{sh} \sim 0.84H_c$ for $\kappa = \lambda_o/l = 20$, yields $d_m = 79$ nm and $H_m = 288$ mT that is 20% higher than H_{sh} clean Nb= 240 mT. In the limit of $(\lambda_o/\lambda) \to 0$, Eq. (71) becomes

$$H_m = \sqrt{H_{sh}^2 + H_{sho}^2},$$

which gives $H_m = 293$ mT [14].

4.3.2 PENETRATION OF VORTICES AT SURFACE DEFECTS

The local penetration of vortices occurs at the inevitable materials or topographic defects at the surface. This SIS multilayer structure can block the dissipative penetration of the vortices at defect in the first superconducting layer.

If there is a topographic defect at the surface of the superconductor, it is a weak spot at which the surface barrier is locally reduced and magnetic flux penetrates before reach to H_{sh}, even before H_{c1}. When a vortex starts to penetrate through the first superconducting layer, it can not penetrate parallel to the surface but enters as a small semi loop around the defect. The vortex semi loop expands under the Lorentz force of Meissner current until it hits the insulator layer which impedes the propagation of the vortex, most part of the dissipative vortex core disappears and converts it into two short vortices of opposite polarity. This vortex–antivortex pair expands during the positive RF cycle and contracts and eliminates in the negative cycle. Therefore, the SIS multilayer greatly reduces the power dissipation at the cavity wall, cavity high field performance is improved and a potential increase of breakdown field of the cavity can be predicted [20].

4.3.3 SS BILAYER SYSTEM

It is particularly important to discuss a system of a superconducting thin film on a bulk superconductor substrate with two different penetration depths λ_1 and λ_2 with no I layer in between. This is referred to as the SS bilayer system.

The SS bilayer structure is protected by the double barriers of the Bean–Livingstone barrier at the surface and the barrier due to the SS boundary. Both barriers can be locally reduced at the defects. If a vortex penetrates from a weak spot due to a surface defect, it may be delayed at the SS boundary. Eventhough, the SS boundary is not as strong as the I layer in the SIS structure, it also contributes to preventing the penetration of vortices [60].

If $\lambda_1 = \lambda_2$, the SS bilayer system can be reduced to a simple semi-infinite superconductor that feels only the Bean-Livingston barrier. When $\lambda_1 \neq \lambda_2$, there exists not only a Bean-Livingston barrier but also a barrier due to the SS boundary. when $\lambda_1 > \lambda_2$, the force due to the SS boundary acts as a barrier to prevent the penetration of vortices. That means the SS boundary pushes the vortex to the direction of the material with a large penetration depth [60].

CHAPTER 5

MAGNETIC FIELD PENETRATION MAGNETOMETER

The performance of alternative SRF materials and structures other than Nb under an external magnetic field needs to be investigated. Implementing RF testing of such materials by applying them into a cavity is a time consuming, expensive next level experiment. On the other hand, testing flat small samples of such materials with a DC magnetometer is relatively reliable to estimate their sustainable maximum surface field. The peak surface magnetic field is a limiting factor of SRF cavities because it determines the potential enhancement of the accelerating gradient. Field onset of first full flux penetration, (B_p) in other words, surface field when first magnetic flux detection at full penetration into the material is a relevant parameter.

Superconducting Quantum Interference Device (SQUID) magnetometer is a largely used technique to measure magnetic flux penetration [15]. The main difficulty is that when the samples are immersed in a uniform external field, the superconducting transition is greatly influenced by the shape, orientation, and edge effects. For the thin film measurements, the demagnetization factor is huge, and alignment becomes a concern.

The third harmonic system has been designed and implemented as a better solution to perform thin film measurements [19, 61, 62]. In this configuration, since a coil with a diameter much smaller than the sample diameter, the field decays quickly around the coil, the field at the sample edges can be ignored. In this measurement system, the 1 kHz AC magnetic field is applied to the superconducting sample using a solenoid coil, and the third harmonic component (3 kHz) is induced in the solenoid coil when the magnetic field penetrates into the sample is detected. Due to setup thermal instability at the higher field, it is a difficult task to reach above 200 mT at 2 K, which is necessary to test many alternative materials for their high field performances.

In this work, magnetic field penetration (MFP) magnetometer is developed to measure the field of full flux penetration using an approach similar to a two-coil technique which has been widely used for the measurements of the magnetic penetration depths and coherence lengths in superconducting films [63–68].

A group from Daresbury Laboratory used a ferrite C-shaped dipole magnet along with a superconducting solenoid to generate a parallel magnetic field at the surface of a flat sample.
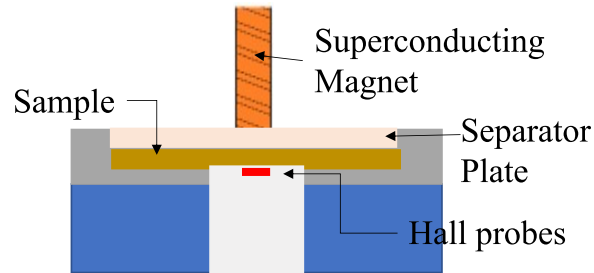
FIG. 21. Main features of experimental setup of MFP magnetometer. A superconducting solenoid is placed above the sample top surface to apply a magnetic filed. Hall probes are mounted at the bottom of the sample to detect magnetic filed penetrated through the sample. A separator plate provides a fixed gap between the magnet and the sample.

In the fact that using the comparably large magnet, the measurement is possibly affected by the edge effect. In their setup, one Hall probe was used to read the applied field and the other one to detect the field penetrating through the sample [69]. Our experimental setup depicted in Fig. 21 uses a similar approach but is able to generate a high surface magnetic field without the use of ferrite. Here a superconducting solenoid is placed above the sample to apply a dc magnetic field to one surface of the film. Instead of using a Hall probe to read the applied magnetic field on the sample surface, we calibrated the applied magnetic field generated at different magnet currents (describes in section 5.4), which helps to minimize the separation between the magnet and the sample and hence to achieve magnetic field high enough to test various superconducting samples having a higher superheating field, H_{sh}. Three magnetic Hall sensors are mounted under the sample to detect penetrated magnetic field through the sample. A 0.5 mm thick separator plate made of sapphire (Al_2O_3) is inserted between the sample and the magnet to maintain a fixed separation between them and protect the sample during the experiment. This setup can house flat samples up to 50 mm in diameter and thicknesses up to a few millimeters. The assembled setup is submerged in a liquid helium bath which allows us to investigate the magnetic flux penetration at the temperatures such as 4.35 K and 2 K.

In the course of the measurements, a sample is cooled down to either 4.35 K or 2 K at zero magnetic field and then the magnet current is increased gradually to apply a magnetic field. If a superconductor thicker than a few λ_L is in the Meissner state, it screens the external

magnetic field so no magnetic field is detected by the Hall probes mounted on the other side of the sample. Once the external field exceeds B_p, vortices enter the superconductor and the magnetic flux breaking through the sample is detected by the magnetic sensors.

5.1 MAGNET DESIGN

The superconducting magnet was fabricated by winding a NbTi thin wire on a dielectric spool using a lathe machine as depicted in Fig. 22(a). This magnet has 4 layers of homogeneous wingdings with 78 turns per layer (Fig. 22(b)). An epoxy was used to insulate the layers and provide a monolithic structure that does not allow movement of the wire inside the coil (Fig. 22(c)). This NbTi wire of diameter 0.325 mm can carry a maximum current of up to 100 A. The assembled magnet has a inner diameter of 6.5 mm, a outer diameter of 8.93 mm, a length of 25.35 mm and can generate a magnetic field greater than 500 mT. Table 3 shows summarized details of the NbTi magnet.

TABLE 3. Materials and dimensions of the superconducting solenoid magnet fabricated for MFP magnetometer.

Material of the wire	NbTi
Material of the spool	Garolite
Wire thickness	0.325 mm
Number of turns per layer	78
Number of layers	4
Inner diameter	6.5 mm
Outer diameter	8.93 mm
Height	25.35 mm

The expected field distribution around our magnet placed above the superconducting sample was simulated using the Poisson computer code. The results shown in Fig. 23(b) were obtained for the parameters of our coil, a fixed gap $d=1$ mm between the magnet and

the sample, and 100 A of magnet current (Fig. 23(a)). The diameter of our magnet was chosen to be five times smaller than the sample diameter of 50 mm to avoid penetration of the magnetic field at the film edges.
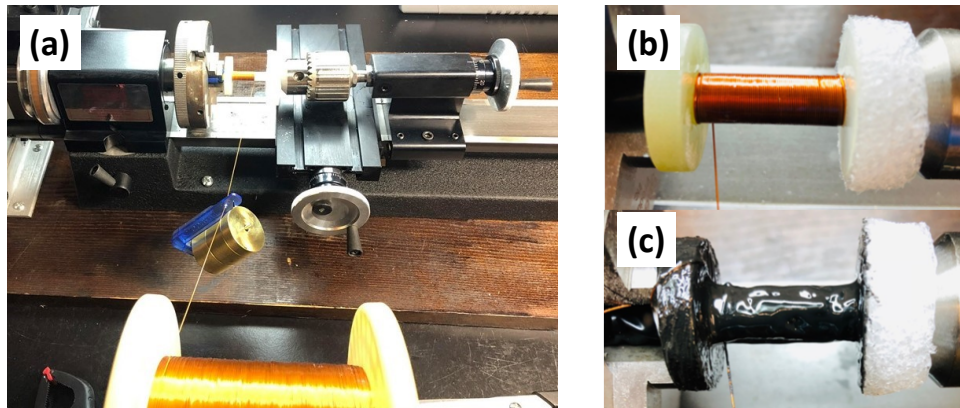
FIG. 22. Fabrication of the superconducting solenoid: (a) setup arrangement used for the magnet wingding (b) dielectric spool with four even layers of wingdings (c) completed magnet with the outer epoxy layer.

FIG. 23(b) shows that a thick superconducting sample in the Meissner state acts as a magnetic mirror, which can be modeled by adding an image magnet placed on the other side of the sample. As a result, the vertical component of the magnetic field (B_z) cancels out and the radial field component parallel to the film surface is twice the radial magnetic field (B_r) produced by the solenoid in free space. This field configuration caused by screening current flowing at the top surface of the sample mimics the field distribution in SRF cavities.

The fabricated solenoid magnet was tested to observe the dependence of the magnetic flux density generated by the solenoid magnet on its electrical current. A final result of the magnet test is the magnetic field at Hall probe location as a function of the applied current ($B = g(I)$).
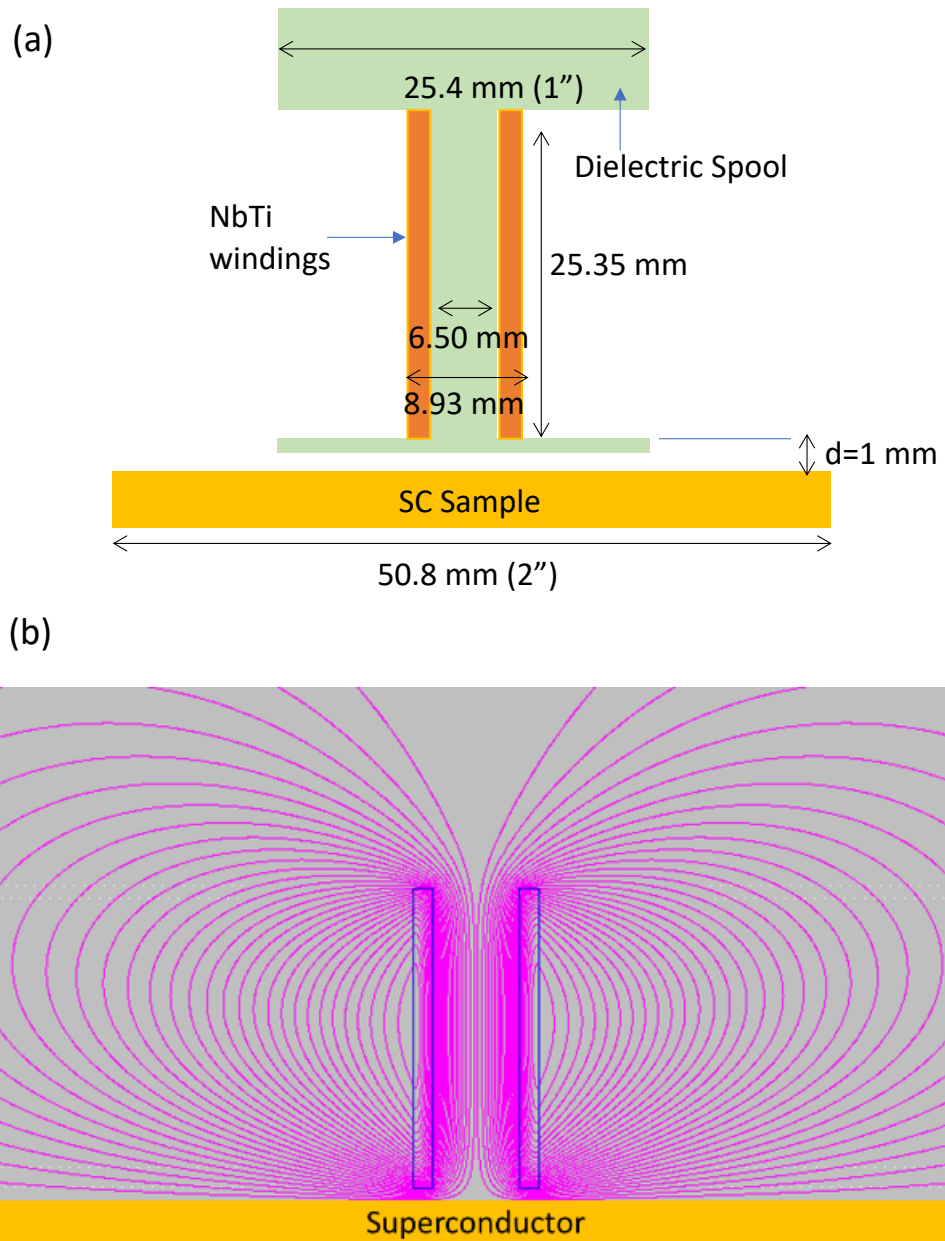
FIG. 23. (a) Dimensions of the multi-turn coil (b) magnetic field around the multi turn coil is expelled from the interior of the superconductor in the Meissner state, which makes the filed lines parallel to the sample surface and mimic the field configuration at the inner cavity surface.

Two Hall probes were placed under the magnet near the edge (where the maximum field from the magnet) so that the sensor surface is perpendicular to its longitudinal axis and the magnetic field. Measurements were performed under forward and reverse electrical currents in order to examine the linearity of the characteristic. Since the NbTi wire can hold the current up to 100 A, we can power up the magnet with a current below 100 A without quenching the magnet. As shown in Fig. 24 curves obtained from both forward and reverse currents coincide with each other with no hysteresis remaining in the magnet wire at zero magnet current.
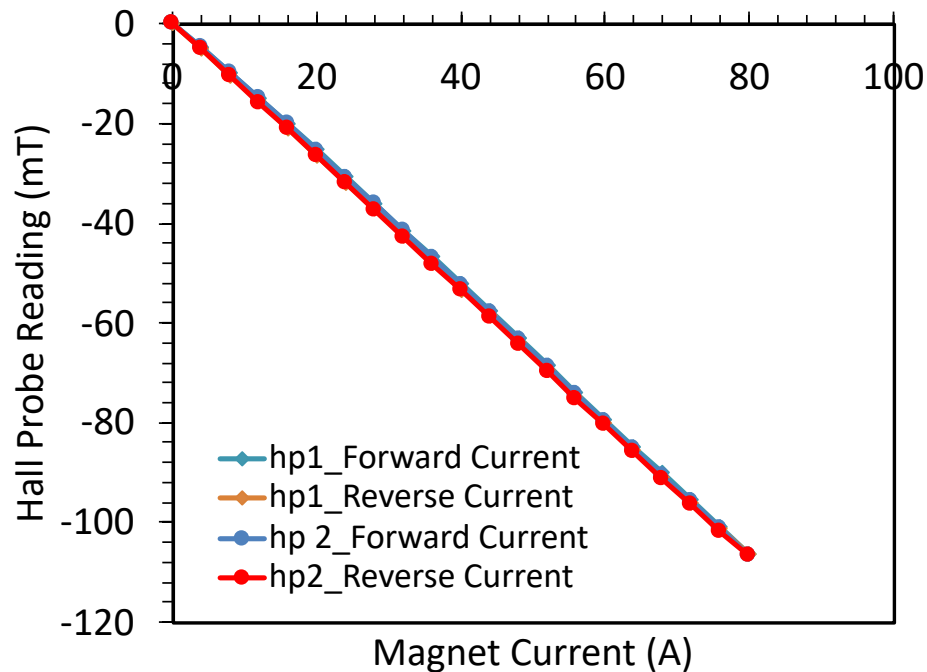
FIG. 24. Testing magnet with no sample: Magnetic field detected from the two Hall probes mounted under the magnet where the maximum field from the magnet with respect to forward and reverse magnet current.

5.2 MAGNETIC SENSORS

The onset of the magnetic field penetration through the sample is measured by three Hall sensors mounted underneath the sample. The Hall probes were calibrated by passing a few tens of mAs through the probe and by measuring the Hall voltage U_H proportional to the applied magnetic field, as shown in Fig. 25(a). In our setup, we used HHP-NP Hall probes from Arepoc to measure the magnetic field normal to the sensor.
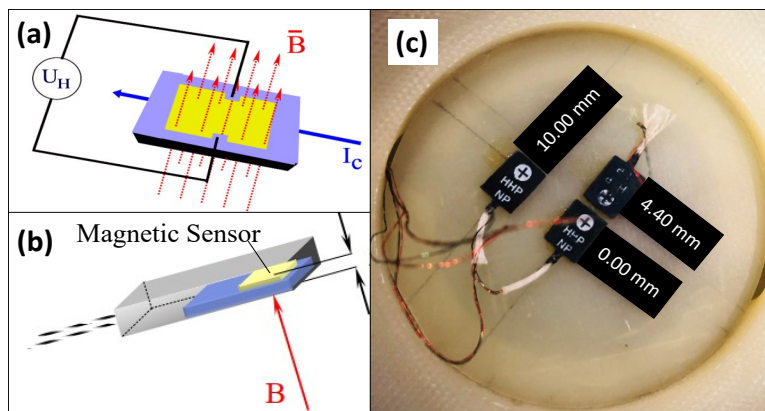
FIG. 25. (a) HHP-NP Hall probes used in the experimental setup which can detect the component of the magnetic field perpendicular to probe (b) the Hall sensor located inside the probe covered with the resin (c) configuration of the Hall probes mounted at the bottom of the sample.

These HHP-NP probes have a sensitivity of 70 mV/T and can operate at temperatures between 1.5 K and 350 K in magnetic fields up to 5 T. The active area center is marked by a cross located on the top surface of the sensor package with accuracy better than ± 0.1 mm. The dimensions of the active area are $500 \times 100 \, \mu$m, and the overall dimensions are $7 \times 5 \times 1$ mm. The model HHP-NP is a probe covered by a synthetic resin in transverse modification and the electrical system is parallel to the bottom surface with high accuracy (Fig. 25(b)).

In our setup, three Hall probes are mounted under the sample, one is at the center other two are at 4.40 mm and 10.00 mm from the center as shown in FIG. 25(c) in order to study the penetrated field profile along the sample radius.

5.2.1 HALL PROBE CALIBRATION

At the very beginning of this experiment, two Hall probes were available (the model HHP-VC high linearity hall probes). The model HHP-VC is developed for operation at a temperature range of 1.5-350 K in magnetic fields up to 5 T similar HHP-NP type. The position of the active area is shifted to the left right corner with the distance 250 μm from the corner edges. The probe is designed for high resolution mapping of the magnetic field and the dimensions of the active area are 50 x 50 μm (smaller than that of HHP-NP) and the overall dimensions are 5 x 4 x 0.8 mm.

Since the HHP-VC model is a probe with a specially passivated uncovered semiconductor surface, it is very tricky to handle them in multiple tests. Because they were broken after a few sample testings, HHP-NP type Hall probes with the protective cover were chosen and ordered with the calibration curve to save our effort and time.

However, at the beginning calibration was carried out for two HHP-VC Hall probes. A superconducting magnet that gives maximum field 1 T (Fig. 26(a)) is used to apply an external magnetic field perpendicular to the probes. A simple circuit was designed to supply a current (10 mA) to the hall probes as shown in Fig. 26(b and c) and to measure Hall voltages for known fields provided by a superconducting magnet.

The Hall voltage is given by
$$V_H = \frac{IB}{ned} \propto B,$$
where n is the density of mobile charge, e is the electron charge, d is the thickness of the conductor in the Hall probe, and B is the magnetic field component perpendicular to the Hall probe.

Measurements were performed at 4.35 K and 2.0 K as shown in Fig. 27 in the increasing and decreasing directions in order to examine the linearity of the characteristic. The sensitivity of the sensor was calculated from the slope of the obtained characteristic curve of Hall voltage plotted against the magnetic field ($V_H = f(B)$).
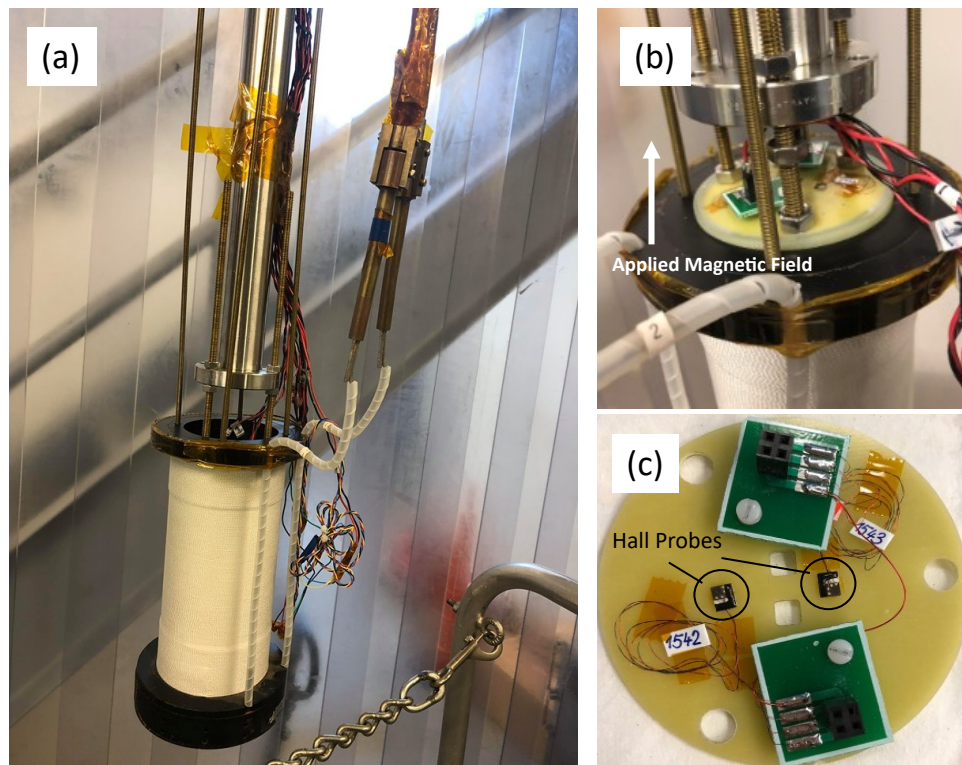
FIG. 26. Setup used to calibrate Hall probes (a) Superconducting magnet that can be powered up to 1 T (b) Hall sensors placed inside the superconducting magnet so that applied magnetic field is perpendiclar to the sensors (c) Circuit designed for two Hall probes.
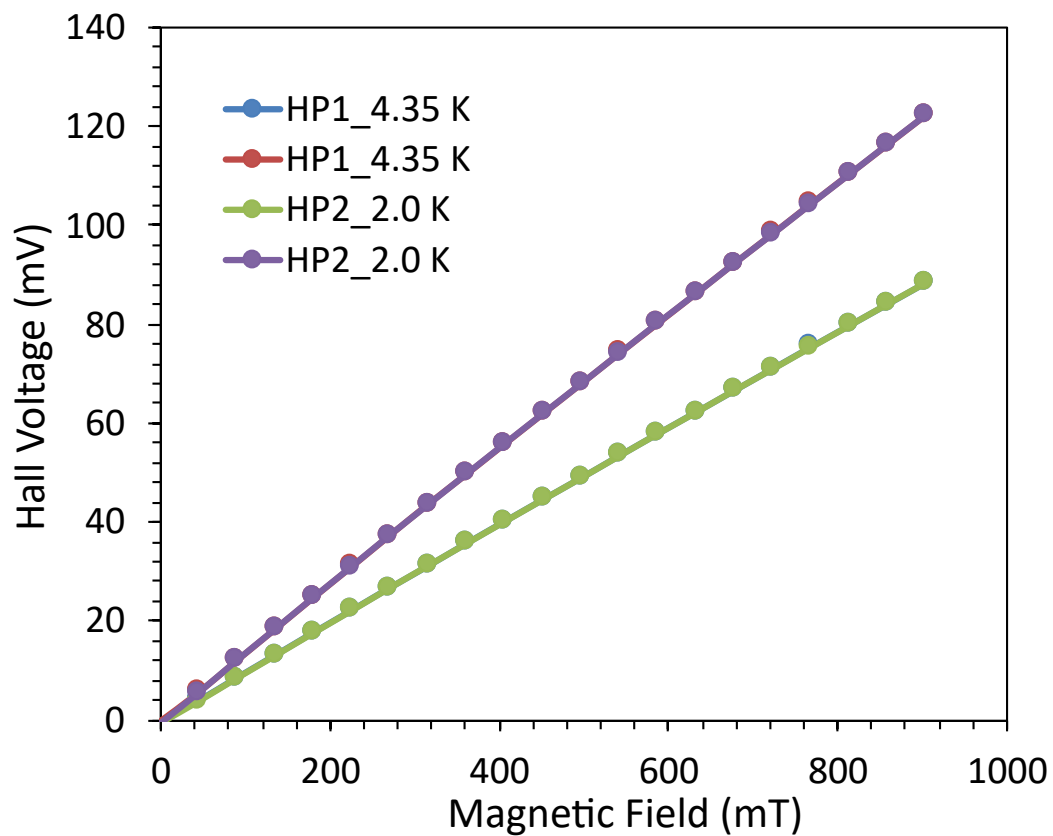
FIG. 27. Hall Probe Calibration at 4.35 K and 2.0 K: Hall voltages recorded for increasing (blue and green) and decreasing (red and purple) magnetic field perpendicular to the Hall probe.

5.3 SETUP ASSEMBLY

All components of the setup were assembled in a nonmagnetic container, as shown in the schematic diagram Fig. 28 and real setup pictures in Fig. 29. The superconducting wires in the magnet were connected to copper current leads which can carry up to 80-90 A. Other features of the setup are finger springs that push the magnet down to avoid vertical movement of the assembly, a G10 plate to permanently mount the Hall probes, and a separator plate between the magnet and the sample to maintain a fixed gap between them and protect the sample surface. According to our simulations, if the gap between the magnet and the sample varies by 0.1 mm, the maximum surface magnetic field changes nearly by 7%.

Furthermore, measurements of flux penetration on thin films are sensitive to surface or edge defects which can cause premature local penetration of vortices. In turn, the heat generated by penetrating vortices causes more vortices to enter the sample which produces more heat and eventually a thermo-magnetic avalanche. To mitigate the flux jumps, the sapphire separator plate was replaced by a copper plate to improve heat transfer from the sample to the He bath. This system is placed in a liquid He dewar at Jefferson lab to perform the experiment at both 2 K and 4 K. Fig. 28(b) represents the schematic diagram of the cryogenic insert with our setup which is placed in liquid He dewar.
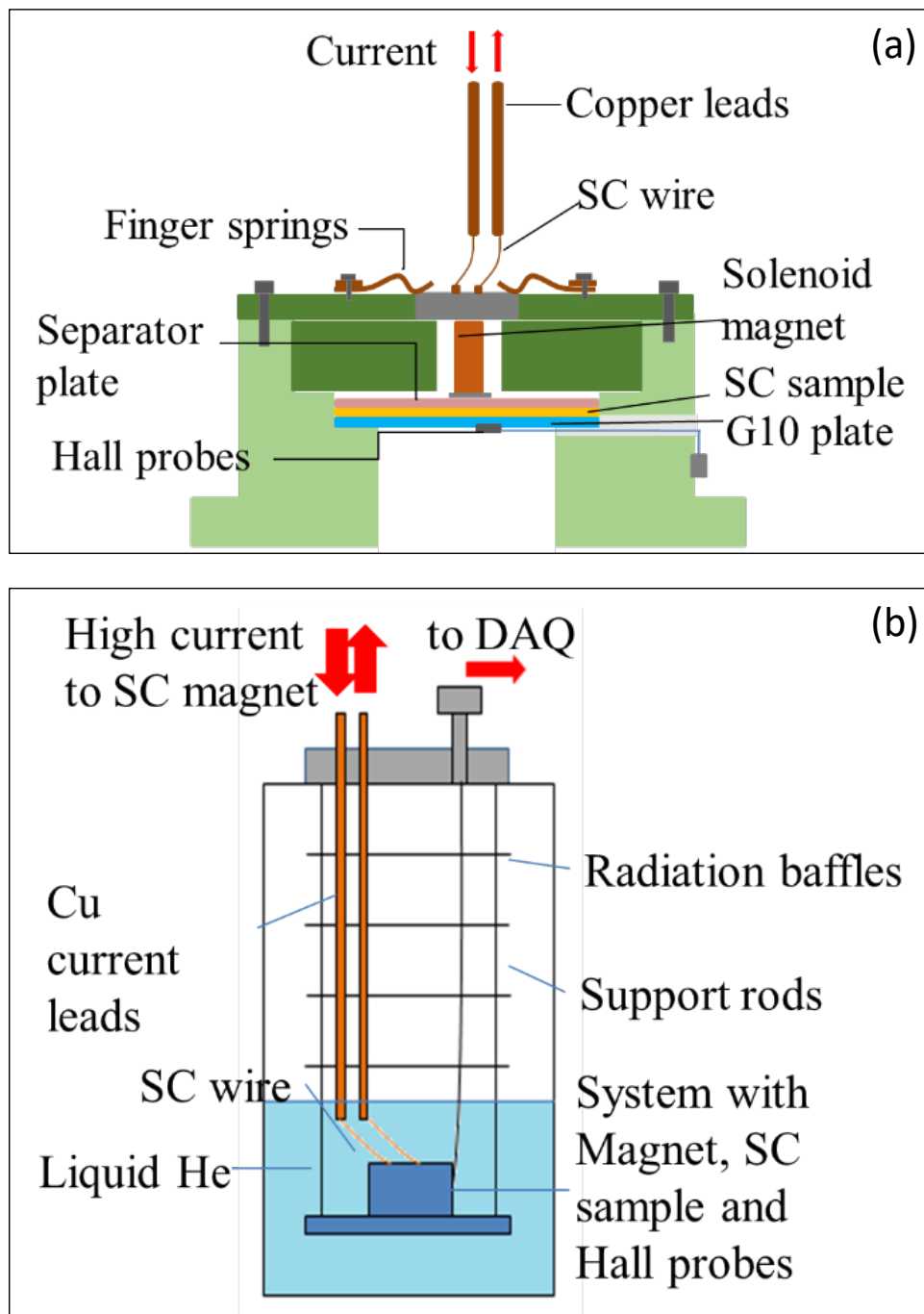
FIG. 28. Schematic diagrams of (a) the nonmagnetic container supports magnetic coil, sample and magnetic sensors symmetrically and (b) Setup assembled in a cryogenic insert.
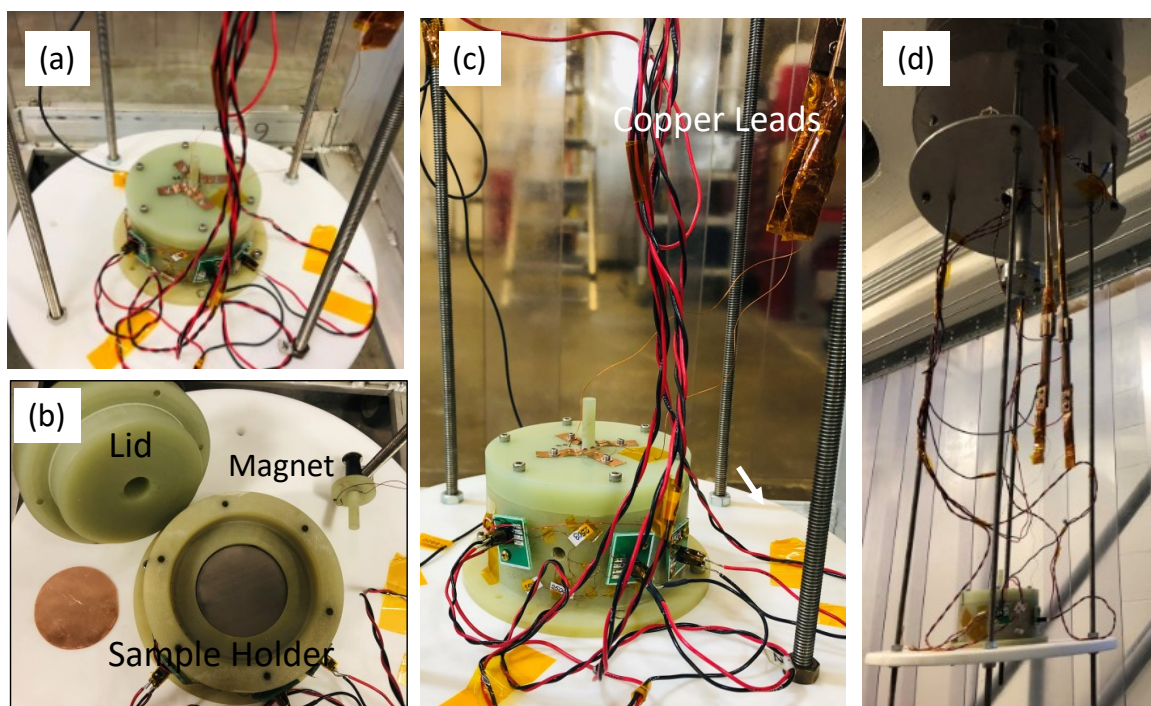
FIG. 29. (a) Outer (b) Inner view of the nonmagnetic container supports magnetic coil, sample and magnetic sensors symmetrically. (c) Two copper leads are connected to the magnet to pass high current (d) This setup is assembled in a cryogenic insert at Jefferson Lab to perform the experiment at cryogenic temperatures.

5.4 SETUP CALIBRATION

5.4.1 CALIBRATION 1

Setup calibration was carried out using 99.99 % pure bulk superconducting Lead(Pb), Tantalum(Ta), and Niobium(Nb) samples with dimensions 50 mm in diameter and 0.1 mm in thickness. The penetrated magnetic field was measured through all three samples separately, Pb at 4.35 K, Ta at 2.00 K, and Nb at both 4.35 and 2.00 K while powering up the magnet with gradually increasing current as shown in Fig. 30(a). These curves indicate the first full penetration of magnetic flux for every three samples clearly, which confirms that this technique is successful to determine the surface fields at which the first flux penetrates through the various superconducting samples. The critical field values from Refs.[28, 29, 70] were used to plot the calibration curve, breakdown field vs current at first full flux penetration. Fig. 30(b) shows the calibration curve of the experimental system which is a linear representation of the critical magnetic field against the current at which the first full flux penetration is detected using the Hall sensor of each three materials.
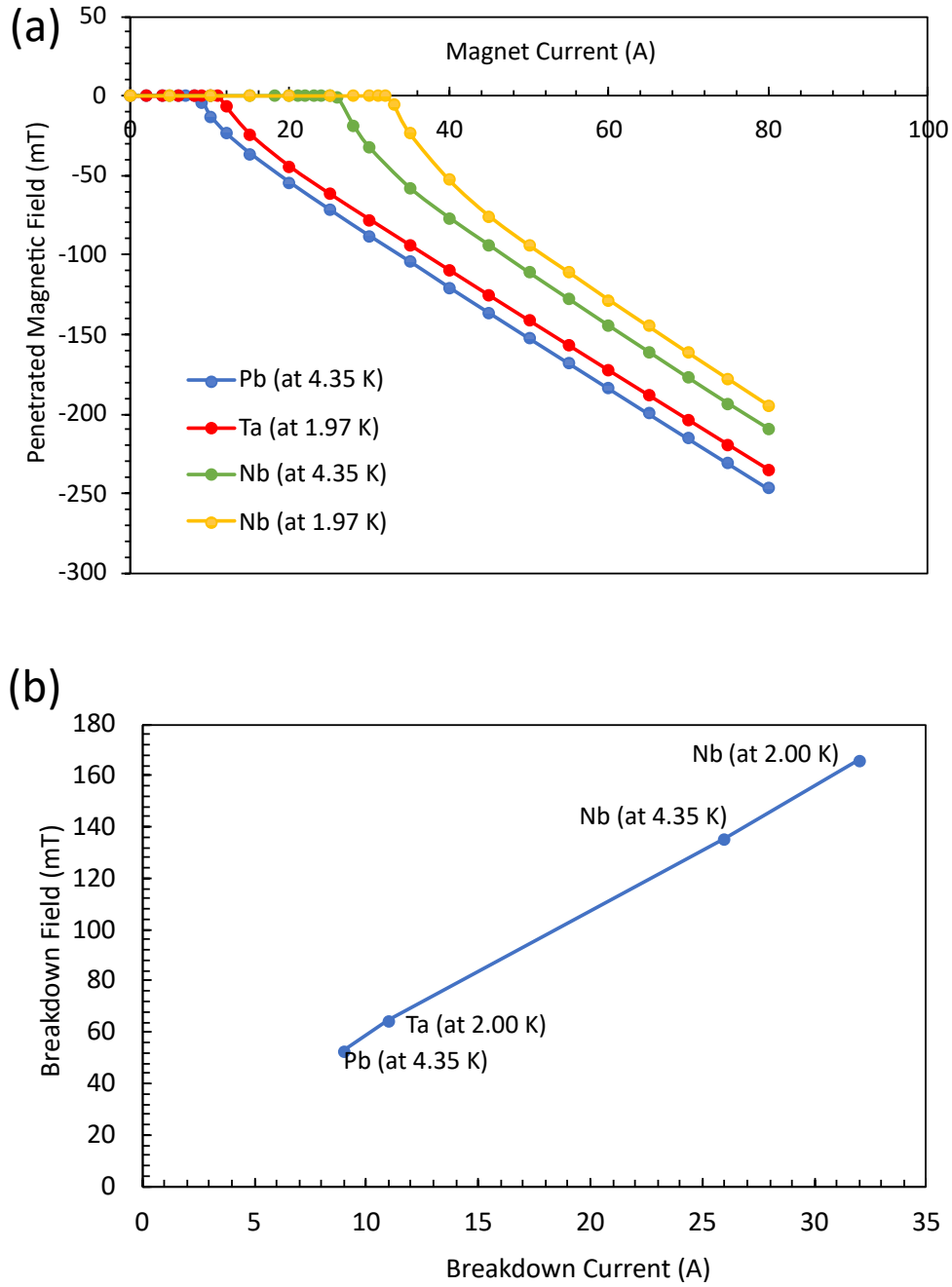
FIG. 30. Calibration 1 (a) Field penetration detected from center Hall probe for 50 mm diameter 0.1 mm thick Pb at 4.35 K, Ta at 2.00 K and Nb at both 4.35 and 2.00 K (b) Calibration curve of magnetic field penetration setup.

5.4.2 CALIBRATION 2

To make setup calibration more accurate, it was performed in several steps to find the maximum magnetic field from the magnet at the sample surface. First, two separate measurements were done without the sample. As shown in Fig. 31, these two tests were done under the same conditions but with different vertical spacings between the magnet and the magnetic sensor. In test 01, the top surface and in test 02 bottom surface of the Hall probe is closer to the magnet.

In both tests, the vertical components of the magnetic field (B_z) at the positions of all three Hall probes were recorded as functions of the magnet current. Measurements were performed both in increasing and decreasing fields to test the linearity of the characteristic curves shown in Fig. 32. With the dipole-like magnetic field distribution of the solenoid, the vertical magnetic field component decreases rapidly within the lateral distance from the magnet axis.
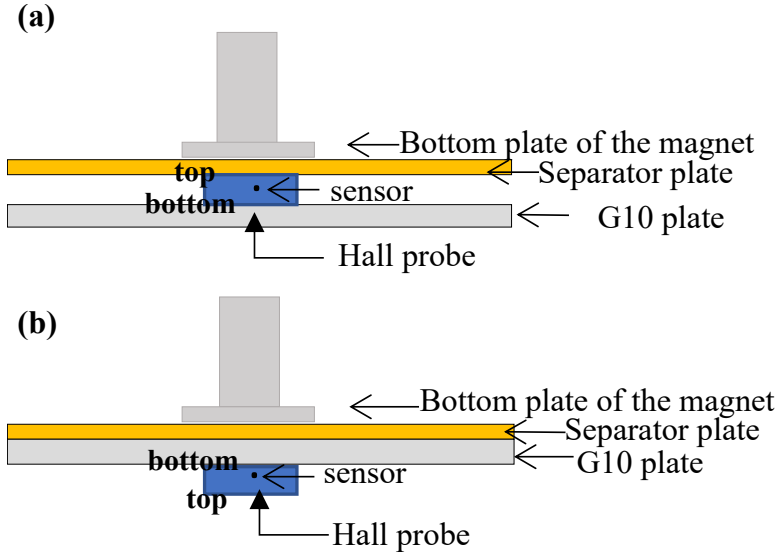
FIG. 31. Setup arrangement with the orientation of Hall probes for the calibration 2 (a) test 01: Hall probes are upside and (b) test 02: Hall probes are downside.

The characteristic Hall probe curves inferred from both tests were used to calculate the vertical magnetic component at three different probe locations which would be observed at 100 A of the magnet current. At the same time, the vertical magnetic field along the sample radius was simulated for 100 A of magnet current. Fig. 33 compares the observed magnetic field detected by the Hall probes with the simulated magnetic field for 100 A. A difference between the measured (black dots) and simulated fields (dashed curves) is mainly due to uncertainty in the spacing between the Hall probes and the magnet. When we corrected the spacing by 0.19 mm (less than the thickness of NbTi wire), the experimental magnetic fields coincide with the simulations.

Finally, a simulation of the actual solenoid was done to find the maximum magnetic field at the sample surface with the magnet current of 100 A taking into account the spacing correction of 0.19 mm mentioned above. The so-obtained radial field distribution $B_{\parallel}(r)$ shown in Fig. 34 is similar to the field between two antiparallel magnetic dipoles spaced by $2d$ with the peak in the radial field $B_{\parallel}(r)$ at the distance $r \sim 4d$ from the magnet axis. The calculated maximum surface magnetic field of 6.26 mT/A was used to calculate the maximum $B_{\parallel}(r)$ (until the Meissner state breaks down) at different magnet currents. This applied surface magnetic field is independent of the sample thickness if the sample is thicker than the London penetration depth. From $B_{\parallel}(r)$ we readily infer the radial distribution of the screening supercurrent density in a thick film: $J_{\parallel}(r, z) = (B_{\parallel}(r)/\mu_0)e^{-z/\lambda_L}$, where $z = 0$ corresponds to the surface of the superconductor. Once the maximum screening current density along the ring of radius ≈ 4mm where $B_{\parallel}(r, 0)$ is maximum exceeds the depairing current density $J_d = H_{sh}/\lambda_L$ the Meissner state becomes unstable with respect to penetration of vortices. This measurement setup was tested on bulk Nb and Pb superconductors, as described in the next chapter.
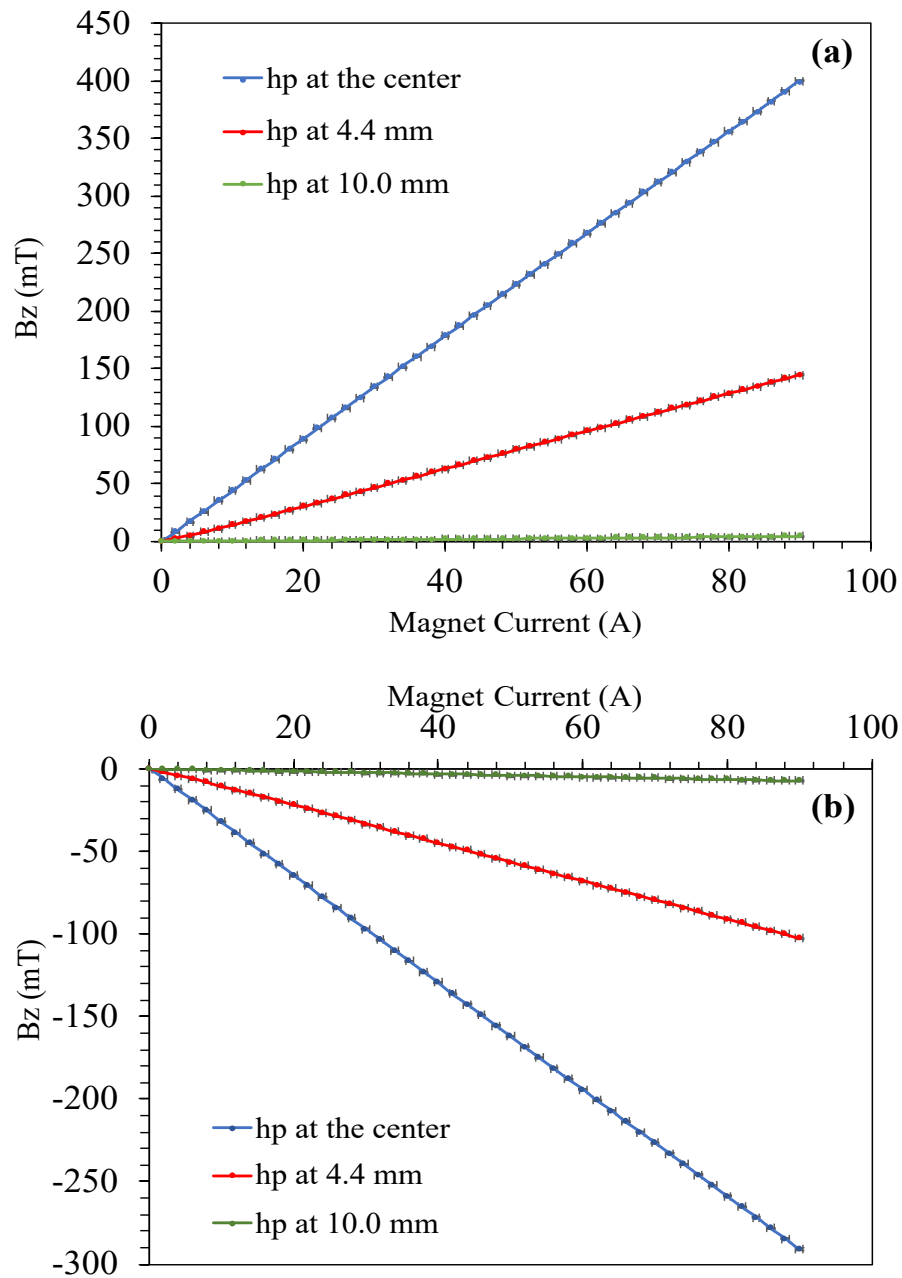
FIG. 32. Vertical component of the magnetic field against magnet current at three Hall probe (hp) positions in (a) test 01 and (b) test 02.
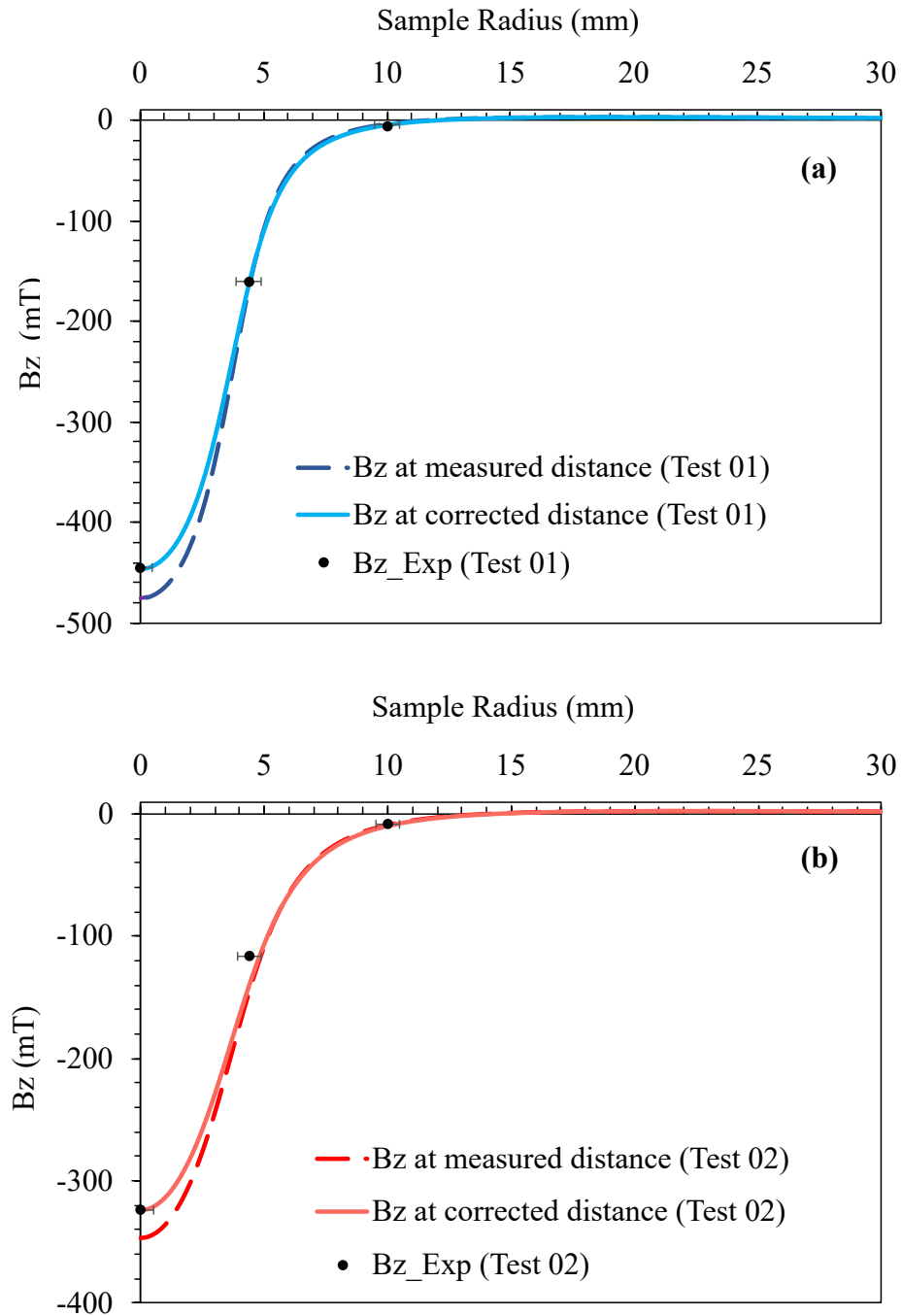
FIG. 33. The simulated vertical component of the magnetic field profile along the sample radius at measured distance (dashed line) and corrected distance (solid line) from magnet to the sensor for 100 A. Extrapolated magnetic field from experimental curves in Fig. 32 at three Hall probe positions for 100 A are marked by black dots. (a) test 01 and (b) test 02.
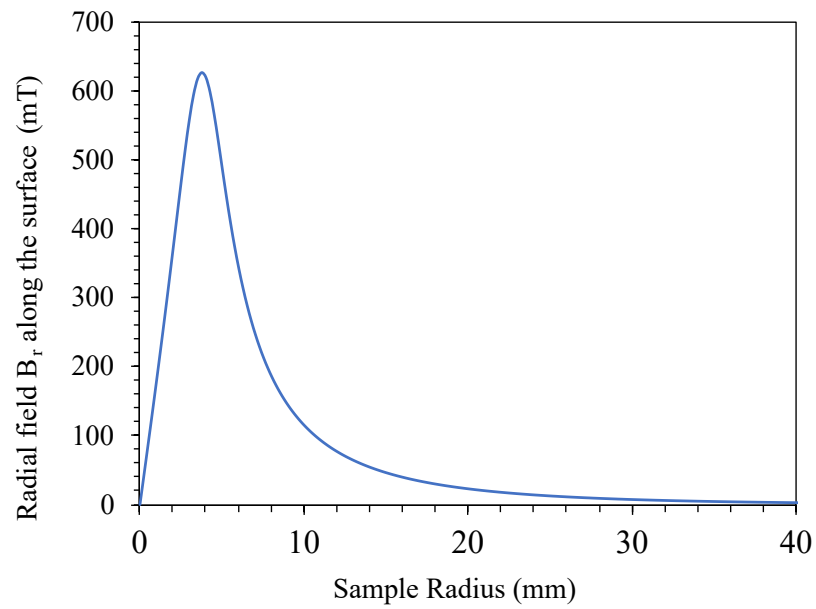
FIG. 34. Radial field B_r on the surface of an ideal superconductor in the Meissner state at 100 A is corrected using above steps and maximum magnetic field is 6.26 mT/A. B_z in the Meissner state is zero.

CHAPTER 6

MEASUREMENTS ON BULK SUPERCONDUCTORS

If a sample is thinner than a few λ_L the applied magnetic field is partially screened, and the z-component of this field is detected by the Hall probes attached at the bottom of the sample. Once the applied parallel field exceeds a critical value at which vortex semi-loops start penetrating the film and reaching its opposite side, the Hall probe detects a jump-wise increase in B_z. In the case of thick films with $d \gg \lambda_L$ studied in this work, the Hall probes detect no signal as long as the magnetic flux does not break through the sample. However, once the magnetic field breaks through the sample, the Hall probe detects the vertical component B_z produced by penetrating vortices, which allows us to measure the field of full flux penetration, B_p, and the critical magnetic fields of the superconductor.

In this experiment, the measurements done using the MFP magnetometer are graphically represented by plotting the penetrated magnetic field (vertical axis) as a function of the surface magnetic field (horizontal axis) in the units mT. Here the penetrated magnetic field is from direct measurements by Hall probes and the surface magnetic field is calculated by multiplying the applied magnet current by the maximum surface magnetic field taken from the calibration (6.26 mT/A). This current-field conversion is valid only up to the breakdown field, B_p at which the applied field lines are parallel to the superconducting surface. After the breakdown field, the applied magnetic field is no longer parallel to the surface, thereby the magnet-current conversion to find the surface magnetic field is not valid anymore. However, this does not affect to the graphical behavior of a particular superconductor, and representing data in this way is convenient to catch B_p of a tested superconductor at first sight without making any calculation.

6.1 BULK LEAD AND NIOBIUM

Our magnetometer was tested on lead (type I superconductor, T_c= 7.2 K) and niobium (marginal type II superconductor, T_c= 9.25 K). Fig. 35 shows the observed magnetic field signal at three Hall probes as a function of the maximum surface magnetic field for 250 μm thick samples (a) lead at 4.35 K and (b) niobium at both 4.35 and 2.00 K. Concurrent first flux penetration through the sample was detected by all three Hall probes; the center probe

detected the strongest penetrated magnetic field. Side Hall probes from the center detected a weaker field and the field of opposite polarity at 10.0 mm in the niobium sample.
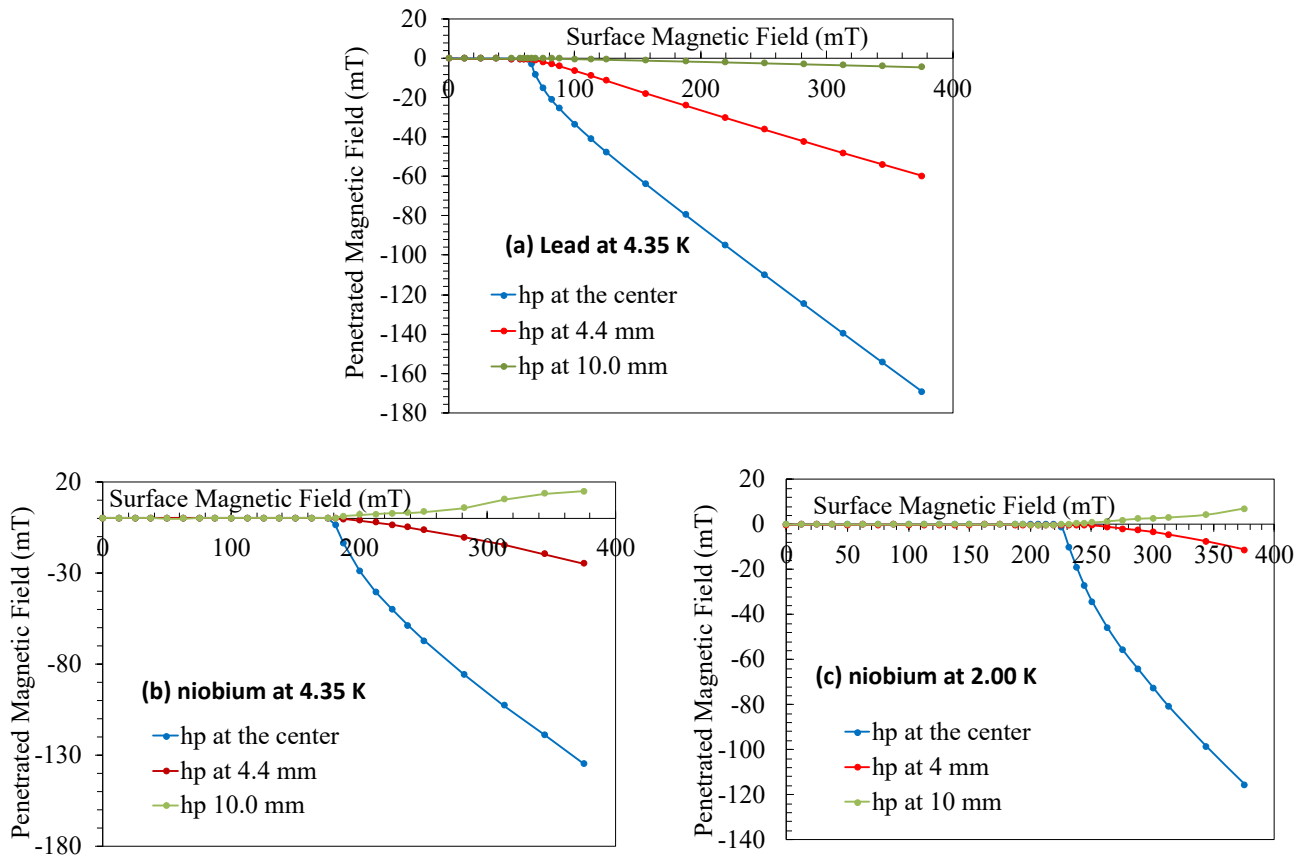
FIG. 35. Penetrated magnetic field detected from three Hall probes (hps) when the surface magnetic field is increased gradually through 250 μm thick (a) lead at 4.35 K and (b) niobium at 4.35 K and (c) at 2.00 K.

These measurements show that, at $B > B_p$, a central circular region of the sample is in a field transparent mixed state while the peripheral parts of the sample remain in the Meissner state. The opposite field polarity detected by the Hall probe at 10.0 mm in Nb

is consistent with the dipolar return field of the magnet focused in a circular region of the mixed superconducting state. As temperature decreases, superconductivity is destroyed at a much higher field, hence B_p increases.
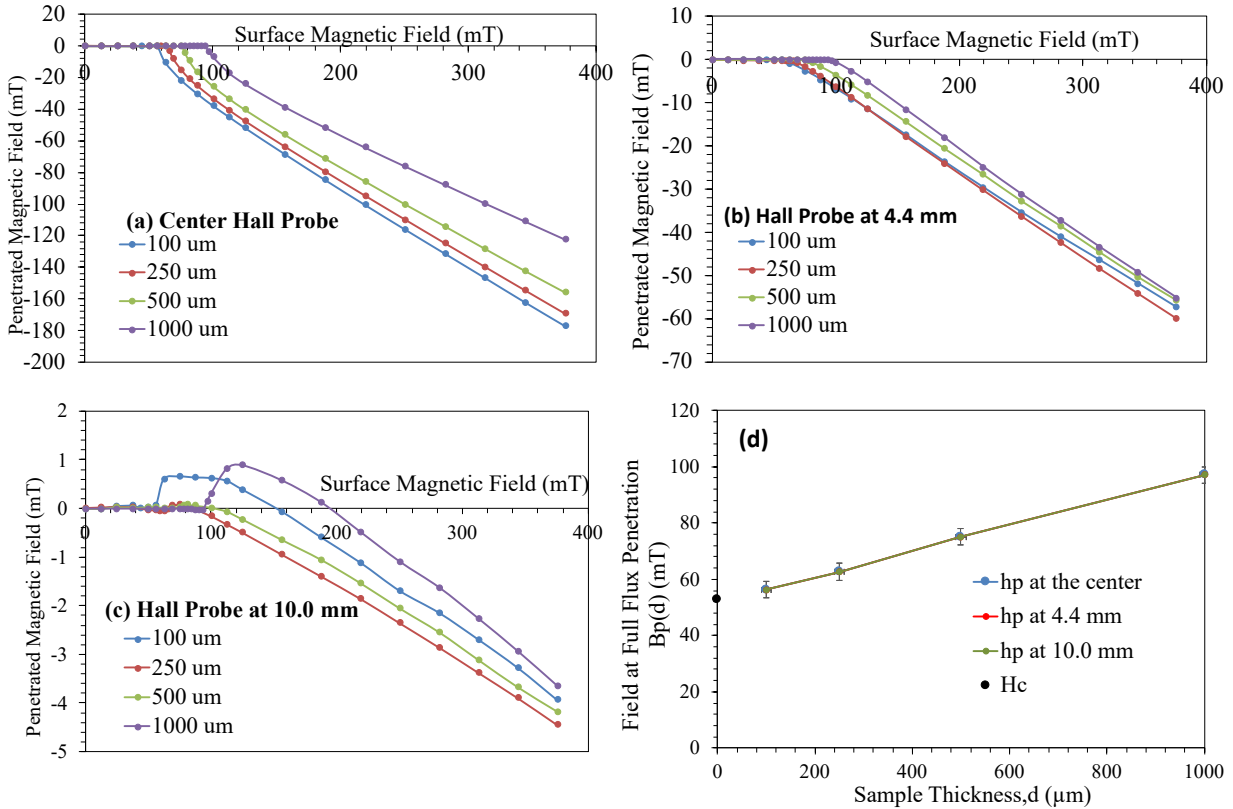
FIG. 36. (a) Penetrated magnetic field detected from Hall probes (a) at the center (b) at 4.4 mm (c) at 10.0 mm (d) The surface magnetic field of full flux penetration through the lead samples with different thickness, $B_p(d)$ at three Hall probe (hp) locations as a function of sample thickness for lead at 4.35 K (three curves overlap with each other). Here, $B_p(d)$ extrapolated to zero thickness is close to B_c of lead at 4.35 K.

6.2 THICKNESS EFFECT

It turns out that the measured field onset of full flux penetration in thick samples with $d \gg \lambda_L$ depends on the film thickness d. The results for lead samples of four different thicknesses at 4.35 K are shown in Fig. 36. Here all three Hall probes detected the first penetrated flux simultaneously. The experiments showed that the maximum surface magnetic field $B_p(d)$ at which the magnetic flux breaks through the sample is a linear function of the sample thickness d. Extrapolation of $B_p(d)$ to thickness $\sim \lambda_L$ gives $B_p(0) = 51.73$ mT, close to the thermodynamic critical field of clean lead, $B_c = 52.64$ mT at 4.35 K [28] (Fig. 36(d)).

We performed the same measurements on niobium samples of different thicknesses at 4.35 K and 2.00 K (Fig. 37) in which case all three Hall probes also detected a nearly simultaneous flux penetration. The resulting full flux penetration field $B_p(d)$ also exhibits a linear dependence on the sample thickness, as shown in Fig. 38. Extrapolations of $B_p(d)$ to $d(\lambda_L)$ give $B_p(0) = 132.54$ mT at 4.35 K and $B_p(0) = 163.30$ mT at 2.00 K.

It turned out that these values of B_p agreed well with the temperature-dependent lower critical field $B_{c1}(T)$ of clean niobium which can be described by a conventional formula

$$B_{c1}(T) = B_{c1}(0)[1 - (T/T_c)^2], \tag{72}$$

where $T_c = 9.25$ K and $B_{c1}(0) \simeq 173.5$ mT [29]. From Eq. (72) we get $B_{c1} = 135.1$ mT at 4.35 K and $B_{c1} = 165.4$ mT at 2.00 K. The slightly lower observed values of $B_p < B_{c1}$ may be attributed to the reduction of B_{c1} by nonmagnetic impurities [41] in our samples.

The thickness dependence of $B_p(d)$ at $d \gg \lambda_L$ results from penetration of vortex semi-loops from the side of the sample exposed to the field of the magnet. As the surface field increases, the size and the number of vortex semi-loops gradually increase until they reach the opposite side of the sample where they produce perpendicular field components detected by the Hall sensors, once the applied surface field reaches the field of full flux penetration B_p. This field at which the vortex semi-loops reach the opposite side of the sample increases with the thickness of the sample. In this quasi-macroscopic limit, the observed linear thickness dependence of $B_p(d)$ is qualitatively consistent with the Bean critical state model in which the flux density profile in the superconductor changes linearly with the distance z from the surface $B(z) = B_\parallel - B_p(0) - \mu_0 J_c z$.
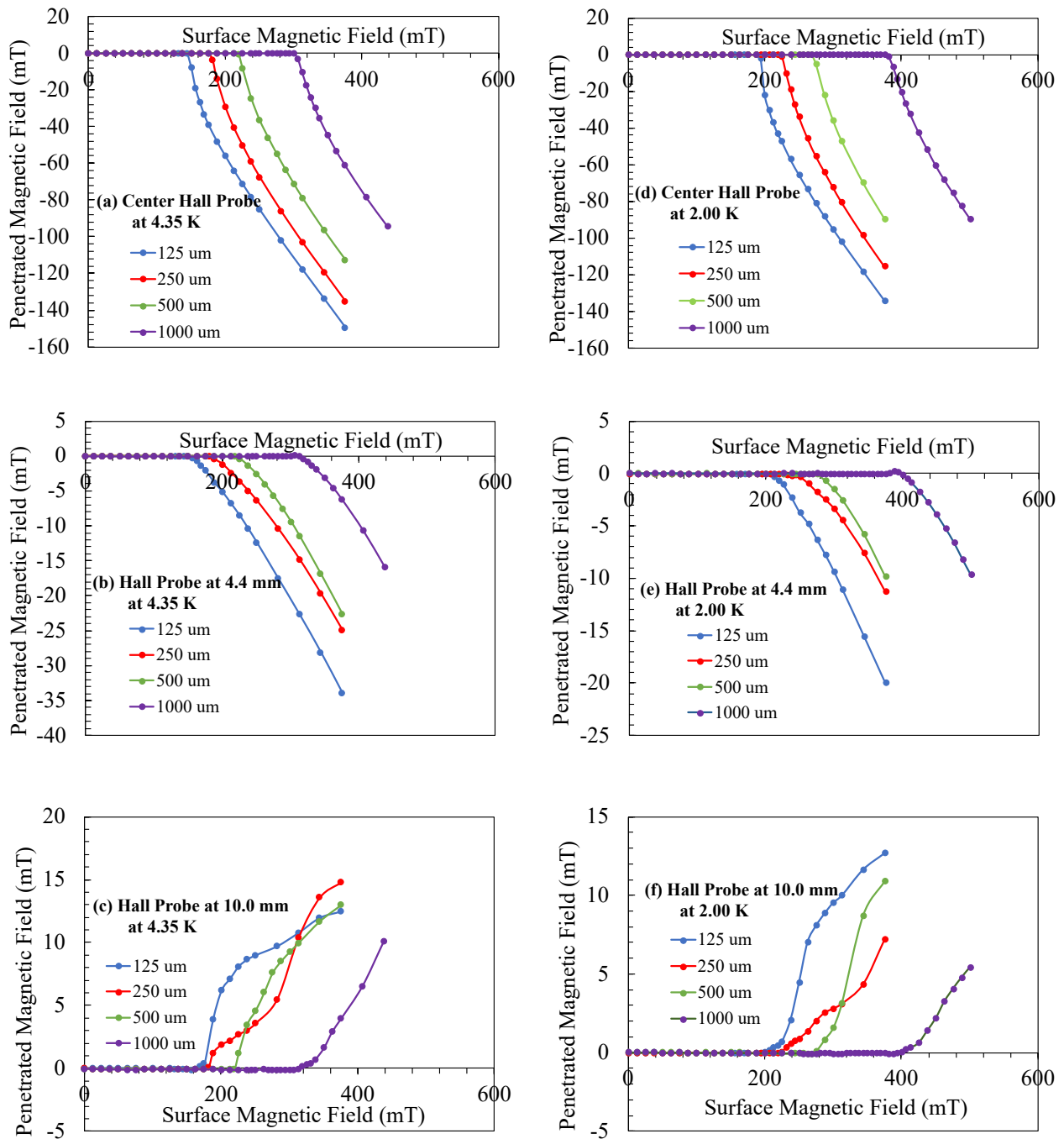
FIG. 37. Penetrated magnetic field detected from Hall probes at three locations, at the center, 4.4 and 10.00 mm from the center at 4.35 K and 2.00 K for niobium samples with different thickness. Hall probe at 10.0 mm detected opposite polarity signal.

Here $B_{\parallel}$ is the applied field which varies along the surface over radial distances much larger than d, $B_p(0) \approx B_{c1}$ is a jump in $B(z)$ in the surface layer of thickness $\simeq \lambda$ due to the Meissner current and equilibrium magnetization of vortices [71], and the depinning critical current density J_c is assumed independent of B at $B \ll B_{c2}$ [41]. Hence, the surface field $B_p(d)$ at which the flux reaches the opposite side of the sample takes the form

$$B_p(d) = B_p(0) + \mu_0 J_c d. \tag{73}$$
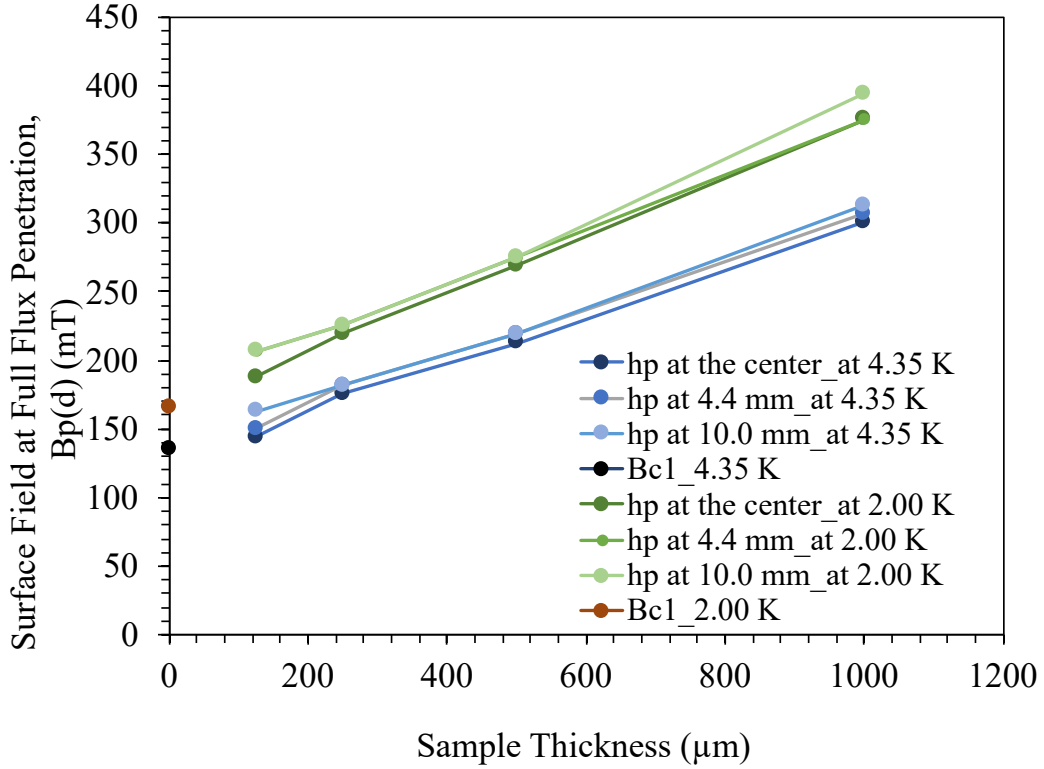
FIG. 38. The surface magnetic field of full flux penetration through the sample, $B_p(d)$ at three Hall probe (hp) locations as a function of sample thickness for niobium at 4.35 and 2.00 K. Here, $B_p(d)$ extrapolated to zero thickness is close to B_{c1} of niobium at 4.35 and 2.00 K.

From Eq. (73) and the slope of $B_p(d)$ for Nb at 4 K shown in FIG.38, we get the critical current density $J_c = [B_p(d_m) - B_p(0)]/\mu_0 d_m \approx 1.41 \times 10^8$ A m^{-2} consistent with J_c values for the cavity-grade Nb with weak flux pinning [72]. Here $B_p(0) = 132.5$ mT and $B_p(d_m) = 310$ mT at $d_m = 1$ mm were taken from Fig. 38. J_c at 4.35 K and 2.00 k was calculated for all Nb samples with different thicknesses shown in Table.4 to investigate the effect of thickness on J_c which follows the same order. Although pinning of vortices by the material defects affects the measured $B_p(d)$, the extrapolation of $B_p(d)$ to $d \simeq \lambda_L \leq 0.1\,\mu$m much smaller than thicknesses $0.1 - 1$ mm of our samples may give either a bulk critical magnetic field B_c for a type-I superconductor (Pb) or the lower critical field B_{c1} in a type-II superconductor (Nb).

As shown above, this procedure yields the extrapolated values of B_p close to the known values of B_{c1} and B_c for Nb and Pb. The nearly linear dependence of $B_p(d)$ also indicates that the pinning of vortices and J_c in our samples are not significantly affected by the film thickness.

TABLE 4. J_c of bulk Nb samples measured using MFP magnetometer.

d (μm)	$J_c \times 10^8$ Am^{-2} (4.35 K)	$J_c \times 10^8$ Am^{-2}(2.00 K)
125	1.11	2.08
250	1.54	1.96
500	1.38	1.78
1000	1.41	1.76

6.3 HYSTERESIS BEHAVIOR

The magnetic response of the superconducting samples were observed not only under ramp up magnetic field, but under ramp down. First, the sample was cooled down from room temperature to a given temperature below T_c in the external zero field and then the field was ramped up to a chosen maximum field above H_c (or H_{c1}) and reversed back to zero. In Fig.39, the curves obtained for lead, tantalum and niobium samples with thickness 0.1 mm describes the hysteresis behavior of superconducting samples.

In the case of a perfect superconductor with no pinning centers, impurities, the magnetization in ramp up and down external field should be the same. But, for the measurements shown in Fig. 39, when the external field exceeds the value H_c (H_{c1} for type II superconductor) and field penetrates the sample and the magnetization is no longer reversible. The reverse path falls below the initial magnetization curve and leaves a some value in zero external field. This is due to formation of trapped flux inside the superconductor.

More magnetic history has been observed in type II superconductors than type I. The sample should be warmed above T_c between two consecutive sample measurements to remove trapped flux which can affect the results.
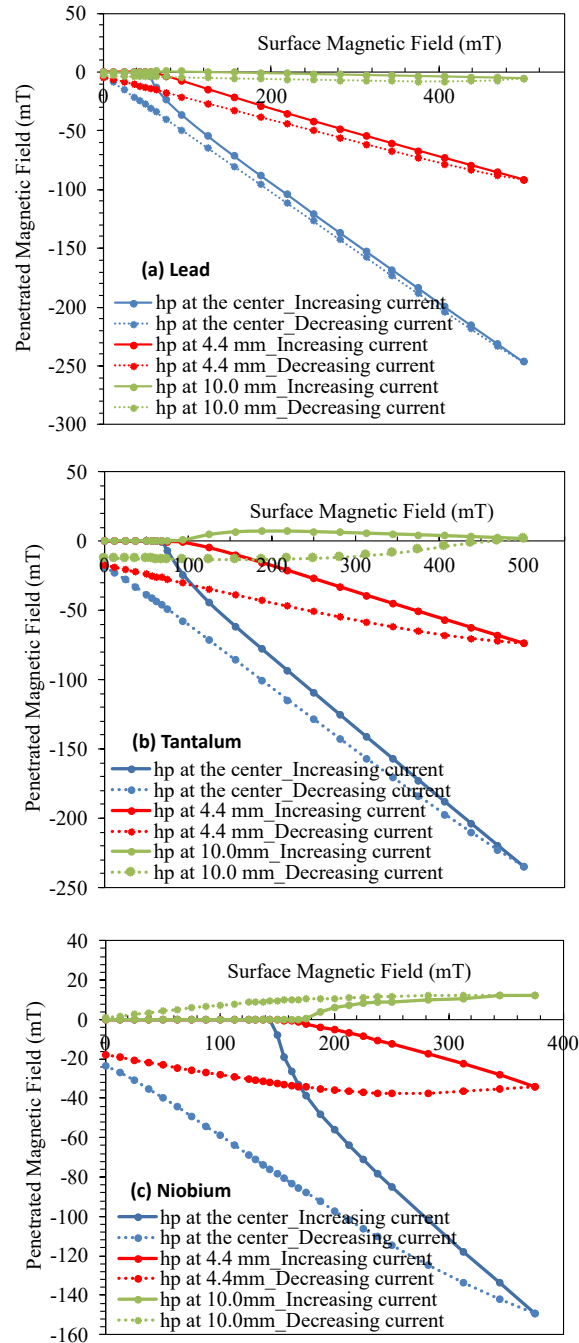
FIG. 39. The sample was cooled down to temperature below T_c in the zero field of the superconducting magnet and the magnetic field was ramped up and down back to zero. Penetrated magnetic field at three Hall probe (hp) locations (a) lead at 4.35 K (b) tantalum at 2.0 K and (c) niobium at 4.35 K and corresponding reversed field curves (Hysteresis).

6.4 MODEL TO SIMULATE BULK Pb AND Nb MEASUREMENTS

Three Hall probes mounted under the sample detect the magnetic field penetration through the superconducting flat sample at three main positions along the sample radius. According to the field penetration data displayed in section 6.1, both lead and niobium show nearly the same field profile along the sample radius except at the 10.0 mm Hall probe signal for Nb, which shows opposite polarity. Hall probe data reveals that when superconductivity breaks down, the strength of the penetrated magnetic field from the center is significantly higher and it decreases along the sample radius. It is worth simulating this behavior using a physical model as depicted in Fig. 40, that is showing the flat disc sample is in its mixed state when applied magnetic field to its surface exceeds the material's critical field. The superconducting film in the mixed state is simulated by a material with a permeability that varies with the radius and applied field.
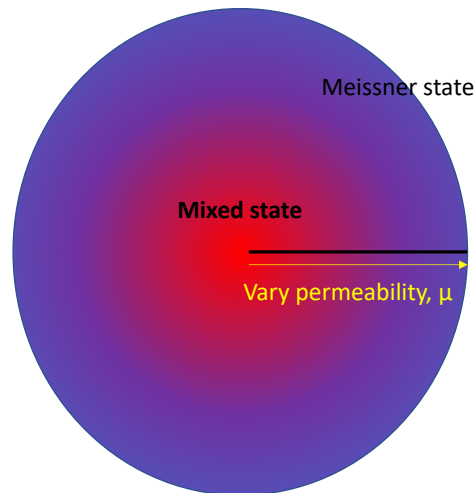
FIG. 40. The flat disc sample is in its mixed state when applied magnetic field to its surface exceeds the material's critical field is simulated by a material with a permeability that varies with the radius and applied field.
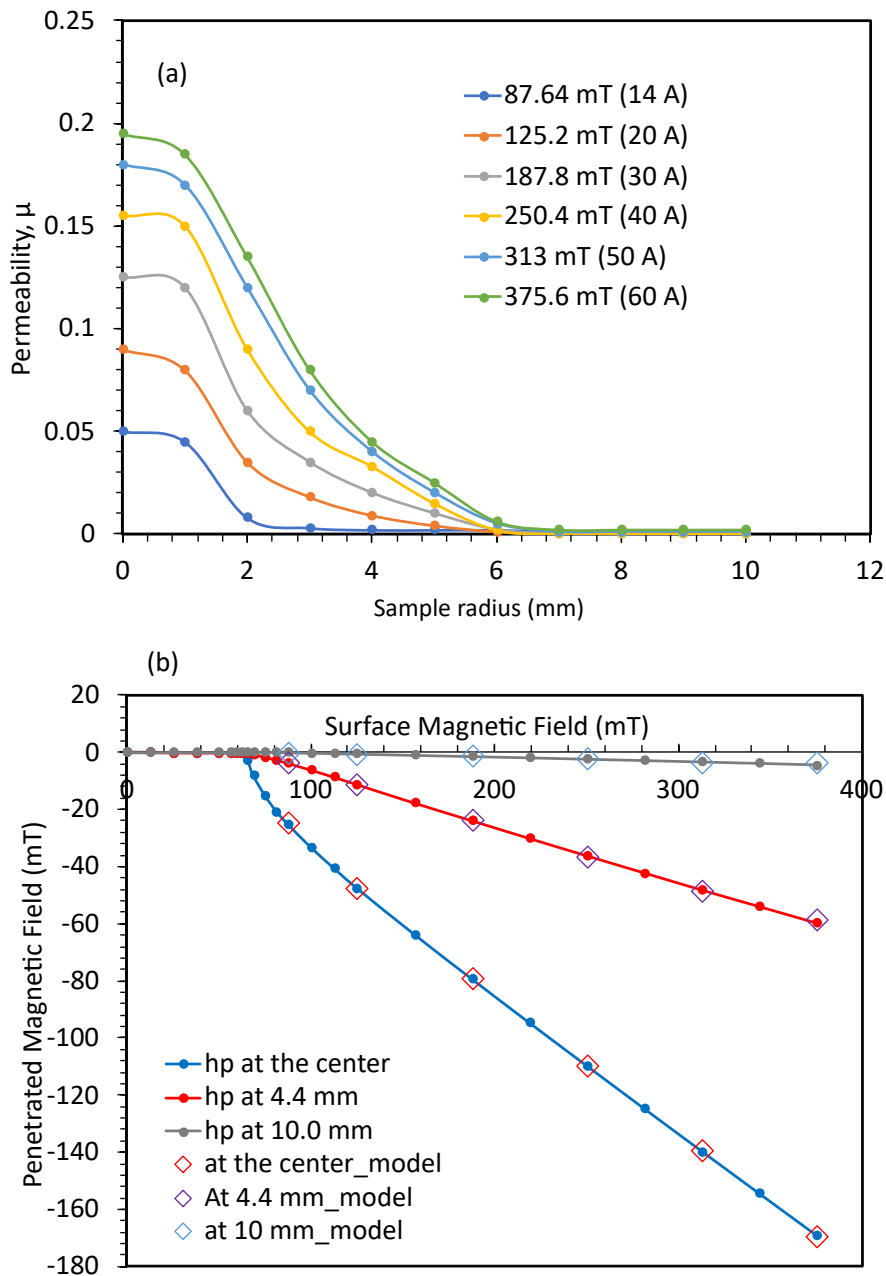
FIG. 41. The model for lead 250 μm thick (a) The variation of permeability along the sample radius at different magnet current greater than critical current when simulated penetrated magnetic field through the sample agrees with measured at three Hall probe locations. (b) Measured penetrated magnetic field as a function of surface field at three Hall probe locations. Open squares represent simulation data.
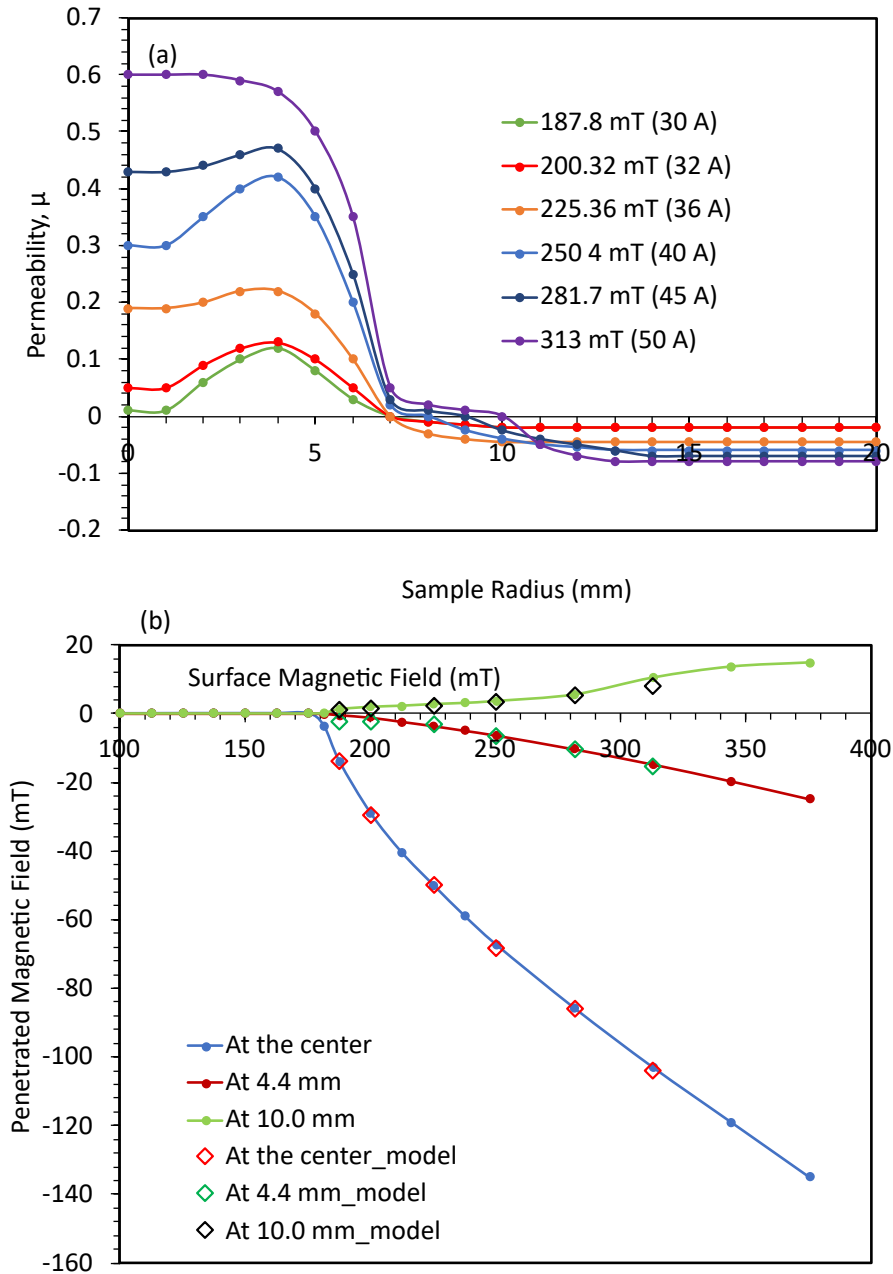
FIG. 42. The model for niobium 250 μm thick (a) The variation of permeability along the sample radius at different magnet current greater than critical current when simulated penetrated magnetic field through the sample agrees with measured at three Hall probe locations. (b) Measured penetrated magnetic field as a function of surface field at three Hall probe locations. Open squares represent simulation data.
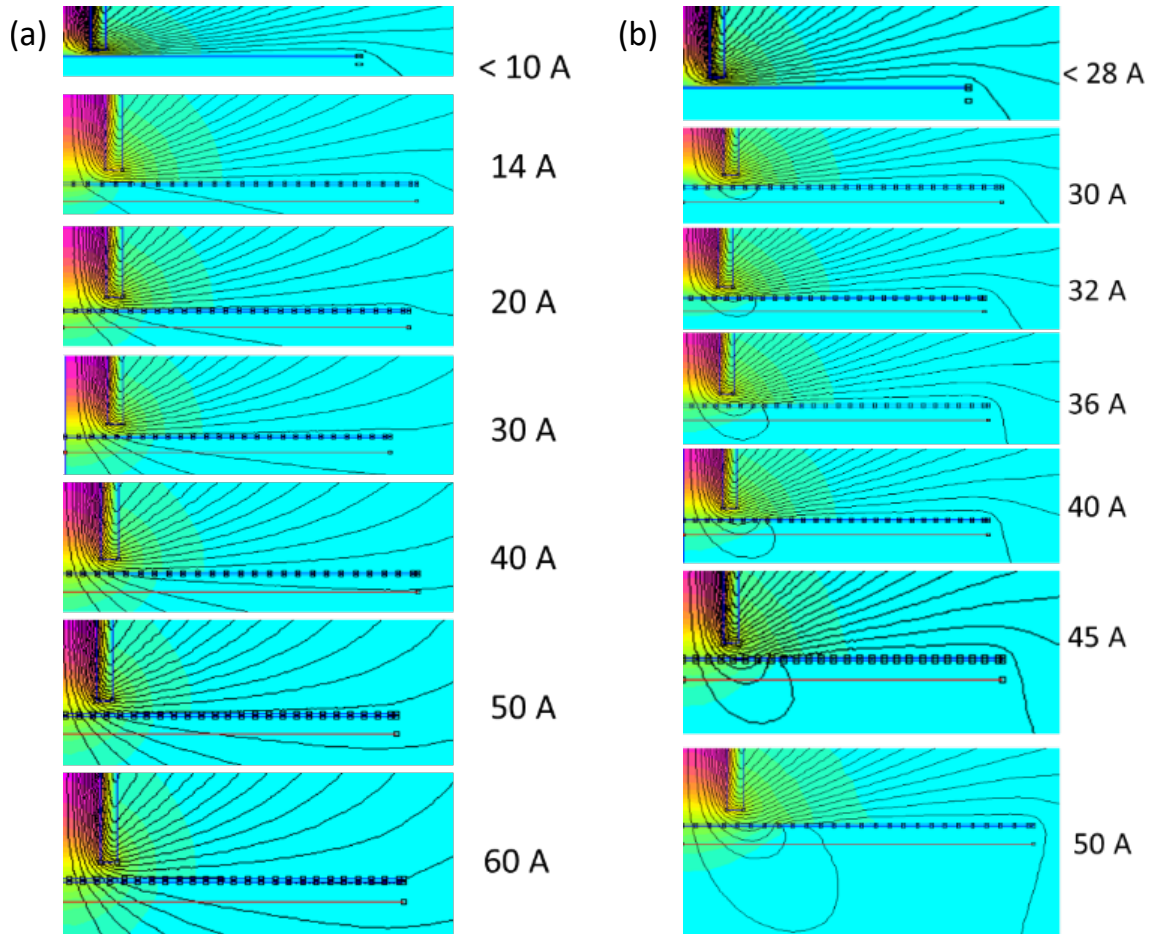
FIG. 43. The magnetic field penetration through superconducting lead and niobium at different magnet current.

In this model, we assume that the center of the sample is in flux transparent mixed state while the peripheral part of the sample is still in the Meissner state due to the variation of permeability, μ along the sample radius. For instance, if μ is 0.6 at some position on the superconductor, which means that 40 % of the sample is still in Meissner state while 60% consists of normal conducting vortices. The finite Element Magnetic Method (FEMM) program was used to simulate the magnetic field at the three Hall probe positions in the mixed state. In this course of the simulation, first a current (greater than the critical current found from the measurements) is applied to the magnet, then the permeability profile along the sample radius is adjusted until penetrated magnetic field matches the measured field at three

Hall probe locations and continue it for different magnet current (surface magnetic field). Fig. 41 and 42 represent the simulated permeability profile on the sample radius at different magnet currents (top) and how the simulated penetrated field at three Hall probe lactations agree with the measurements (bottom) for lead (type I superconductor) and niobium (type II superconductor) in the order. In the case of niobium, negative permeability is the response of the Nb sample to the imposed magnetic field coming from field lines in the opposite direction by the magnetic dipole. Fig. 43 depicts the diagrams of field penetration into lead and niobium samples with increasing magnetic field. However, this simulation is preliminary and it should be developed considering the nonlinearity behavior of superconductors in the mixed state.

CHAPTER 7

MEASUREMENTS ON THIN FILM SUPERCONDUCTORS

Superconducting thin films have been suggested as a promising technology to surpass the performance of bulk niobium cavities. The best niobium narrow film cavities have already achieved higher Q at low fields than bulk niobium. The sensitivity of the residual resistance to trapped magnetic flux is less in thin film cavities compared to bulk niobium [73]. Superconducting thin films also have the possibility to use substrates such as oxygen-free copper that dissipates heat more efficiently than bulk niobium and Nb thin film on the copper structure is more cost-effective than bulk niobium [74]. Another interest of thin film technology is SIS multi-layer thin film structure which has been proposed as a way to use magnetic shielding layers to increase both accelerating gradient and Q factor [13, 14].

In our study, thin film fabricated on sapphire and metal substrates are tested using the MFP magnetometer along with some other structural characterizations.

7.1 CHARACTERIZATION METHODS

Magnetic Field Penetration Measurements

MFP magnetometer was used to perform magnetic field penetration measurements that allow the identification of field at first full flux penetration, B_p of each thin film. B_p is a handy characteristic of a thin film to observe its sustainability under an external parallel magnetic field to its surface.

T_c and RRR Measurements

The transition temperature, T_c and residual resistant ratio, RRR of thin films are measured with the so-called four-point probe method. The electrical resistance decreases with temperature. In reality, the decrease in resistance is limited by impurities and other crystallographic defects, hence it indicates an index of the purity and overall quality of a sample. Higher RRR denotes higher purity.

RRR is defined as

$$RRR = \frac{R_{300K}}{R_{4.2K}}, \tag{74}$$

where R_{300K} and $R_{4.2K}$ are the resistance at room and liquid helium temperatures, respectively at standard atmospheric pressure. For instance, with the superconducting behavior of Nb below its T_c =9.2 K, $R_{4.2K}$=0. Hence, dc electrical resistance, R of the Nb is measured at room temperature (300K) and just above T_c. Then, $RRR_{Nb} = \frac{R_{300K}}{R_{10K}}$. Purity of niobium used for cavity fabrication is high, RRR = 300 [75].

The RRR can be also related to the mean free path. Resistance, $R \propto (\rho + \rho_{res})$. ρ_{res} is constant and temperature dependent. The resistivity of the material is given by, $\rho = \frac{m_e}{ne^2\Gamma}$, where m_e is the mass of the electron, e is its charge, n is the number of unpaired electrons in the materials, those are constant depending only on the atomic properties of the pure material and Γ is the average time between collisions, it is $\Gamma = l/v_f$ where v_f is Fermi's velocity and is still a constant but l depends on the impurities in the material. The product ρl can be considered constant for a given metal (3.75×10^{-6} Ωm^2 for Nb) and can be used to estimate the mean free path from the resistivity.

The transition temperature T_c and the transition width ΔT_c calculated from the resistance vs temperature curve using following equations

$$T_c = \frac{T(90\%) - T(10\%)}{2}, \tag{75}$$

$$\Delta T_c = T(90\%) - T(10\%), \tag{76}$$

where T(90%) and T(10%) are the temperatures corresponding to the 90 % and 10 % of the resistance before the transition respectively.

X-ray Diffraction (XRD)

XRD is a powerful non-destructive method used to measure the average spacings between layers or rows of atoms, the orientation of a single crystal or grain, the crystal structure of an unknown material, and the size, shape, and internal stress of small crystalline regions. English physicists W. H. Bragg and his son W. L. Bragg developed a relationship, called Bragg's law $n\lambda = 2d\sin\theta$, in 1913 to explain why X-ray beams are reflected in crystal structure at certain angles of incidence, θ. d is the distance between atomic layers in a crystal, λ is the wavelength of the incident X-ray beam and n is an integer. The atomic

planes of a crystal cause an incident beam of X-rays to interfere with one another as they leave the crystal. The phenomenon is called X-ray diffraction (Fig. 44), thus the X-ray diffraction pattern is representative of the crystal structure of a given sample.
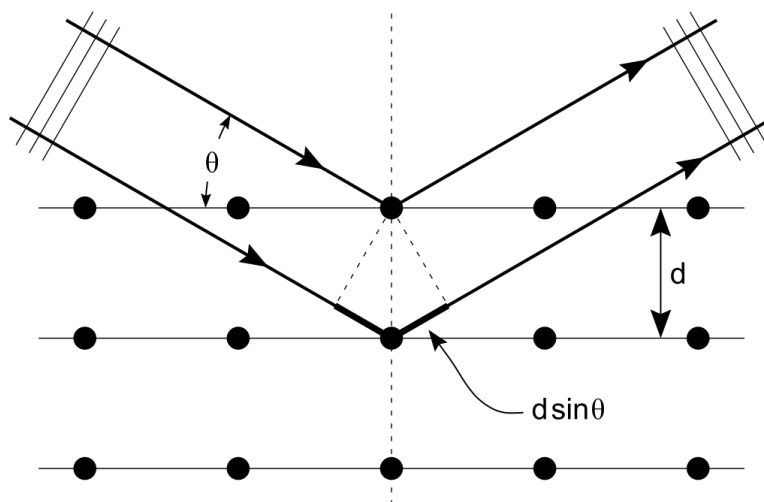
FIG. 44. The atomic planes of a crystal cause an incident beam of X-rays to interfere with one another as they leave the crystal.

The crystal structure of the films was characterized by monochromatic Cu-Kα radiation on Rigaku Miniflex II Xray diffractometer. Wavelength of X-ray diffraction for Cu-Kα is 0.15418 nm.

The Scherrer equation uses an analysis of x-ray data from a θ - 2θ scan to calculate the average crystallite size in a polycrystalline material given by $D = \frac{K\lambda}{\beta \cos \theta}$, where K is a dimensionless shape factor, with a value close to unity. The shape factor has a typical value of about 0.9, but varies with the actual shape of the crystallite, λ is the X-ray wavelength, β is the line broadening at half the maximum intensity (FWHM), after subtracting the instrumental line broadening, in radians, and θ is the Bragg angle.

Scanning electron microscopy (SEM)

The SEM is a microscope that uses electrons instead of light to form an image. SEM has many advantages over traditional microscopes. The SEM has a large depth of field, which allows more of a specimen to be in focus at one time. Images with much higher resolution of the morphology or topography of a specimen at very high magnifications can be obtained. Because the SEM uses electromagnets rather than lenses, the researcher has much more control over the degree of magnification.

Electron Backscatter Diffraction (EBSD)

EBSD is a scanning electron microscope (SEM) based technique with a backscatter diffraction camera for materials characterization. In EBSD, the electron beam is scanned across the surface of a tilted crystalline sample, the diffracted electrons at each point form a pattern that can be detected and then analyzed using dedicated hardware and software. At each point, the indexing process provides information about the phase and the crystallographic orientation from which the microstructure can be effectively reconstructed. This enables a full characterization of the microstructural properties of the sample.

The availability of a combination of SEM (the sample's geometrical features), EBSD(crystal structure), and EDS (chemical composition) in one instrument is impressive.

In the framework of EBSD analyses, the Tescan Vega SEM instruments with the Edax Velocity EBSD camera at Jefferson Lab was used.

Thickness Measurements

The Bruker Dektak XT Surface Profiler and Empyrean Series 2 X-Ray Diffraction System (XRD) were used to find thickness of thin films that can perform the critical nanometer-level film, step and surface measurements.

7.2 NIOBIUM THIN FILMS

Niobium cavities have technological benefits with respect to copper cavities. However, defects on the cavity surface can trigger the dissipation of energy at high accelerating fields, causing thereby local heating, which leads to thermal instabilities, and eventually to the cavity quenching. Thermal stability can be improved by enhancing the conductivity of Nb,

mainly using high-purity Nb and by minimizing surface defects. Bulk niobium has a typical heat conductance lower than ~ 75 W/mK at 4.2 K if the purity is high as RRR=300, whereas, for copper, the value is 300-2000 W/mK [11]. The RF cavities made of copper and coated with a thin layer of superconducting material (typically Nb) are very attractive because copper substrate can remove excessive heat to the He bath. It is a relatively low-cost supporting structure that provides much better thermal stability, that is already widely used as an alternative to bulk Nb cavities. Copper is a strong candidate for cavity fabrication due to its availability, cost, machinability, and higher thermal and electrical conductivity. If the performance can be improved to approach that of solid niobium, it could provide a significant cost reduction for SRF-based particle accelerators.
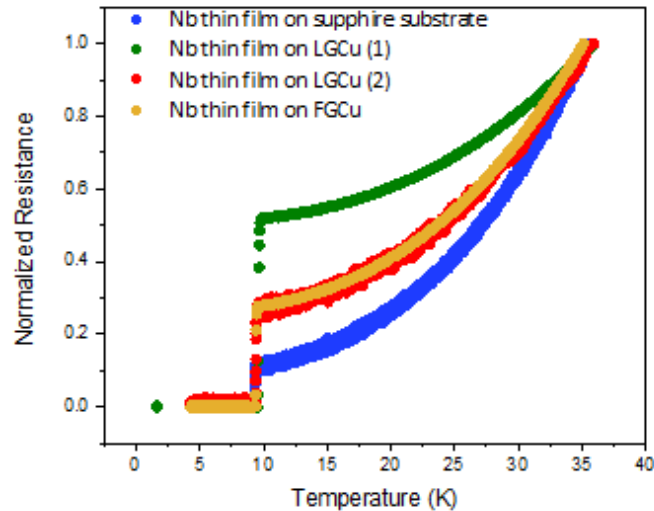
FIG. 45. Normalized resistance as a function of temperature measured using four-point probe method for 3 um thick single crystal niobium (001) thin film fabricated on Al_2O_3 wafer with RRR=332 (blue), 1 um thick niobium thin film fabricated on large grain copper with RRR=34 and 190 (green) and (red) and 1 um thick niobium thin film fabricated on fine grain copper with RRR=107 (yellow) by Electron Cyclotron Resonance (ECR). This RRR data is taken from measurements done at Jefferson Lab.

In 1980 CERN started to develop the sputtering technique for the deposition of thin Nb films on Cu cavities, starting optimizing deposition parameters using small samples, coating extended to 3 GHz cavities and later on up to 500 MHz cavity [76]. At that time, the poor thermal conductive, less-purity Nb sheet (RRR ~ 40) was used to fabricate cavities. Typical performance of bulk cavities at 500 MHz and 4.2 K was $Q \sim 2.5 \times 10^9$ with $R_s \sim 100$ nΩ at low field and it decreases nearly by a factor of two with maximum accelerating field of 10 MV/m [77]. Nb sputter-coated copper cavities showed higher Q than bulk Nb cavities due to a lower BCS surface resistance, but it decreased rapidly with the field than for bulk Nb due to the residual resistance, and the accelerating field reached values higher than 8 MV/m. Better results were achieved by smoothening the surface by chemical polishing to enhance the adhesion of the film to bulk copper [77].

TABLE 5. RRR and Tc values from four point probe method and B_p from field penetration measurements of Nb thin film coated using ECR method

.

Sample	RRR	T_c (K)	ΔT_c (K)	B_p (mT)	
				4.35 K	2.00 K
(a) Nb on Sapphire	332	9.31	0.03	62.6	80.1
(b) Nb on LGCu (1)	34	9.57	0.28	78.3	97.0
(c) Nb on LGCu (2)	190	9.47	0.24	90.8	125.2
(d) Nb on FGCu	107	9.43	0.10	106.4	106.4

A different approach pursued at Jefferson lab, Electron Cyclotron Resonance (ECR) was used to coat these Nb thin films on copper and sapphire substrates [78]. ECR is an energetic vacuum deposition featuring both ultra-high vacuum (UHV) and high deposition energy, which are the keys to obtaining a high-quality thin film. The energy of the niobium ions was controlled by a bias voltage to obtain the best film quality.

Part of this work was dedicated to perform magnetic field penetration measurements on ECR Nb thin film coatings on both sapphire and copper at Jefferson Lab to investigate their behavior under an external magnetic field and to perform the capability of the MFP magnetometer on thin film measurements. Measurements were done at both 4.35 K and 2.00 K on four Nb thin films on different substrates: single crystal a-plane sapphire wafer, large grain (LG), and fine grain (FG) copper. The RRR and T_c values extracted from resistivity measurements of the sample from room temperature down to below T_c using a four-point probe shown in Fig. 45 and field at first full flux penetration, B_p observed from MFP magnetometer measurements shown in Fig. 47, 48, 49 and 50 are listed in the Table 5.

The magnetic field penetration through thin film depends on the quality of the substrates which is a great influence on the quality of the film. Thin films typically take the substrate morphology, thus, the substrate roughness affects the roughness of the thin film.
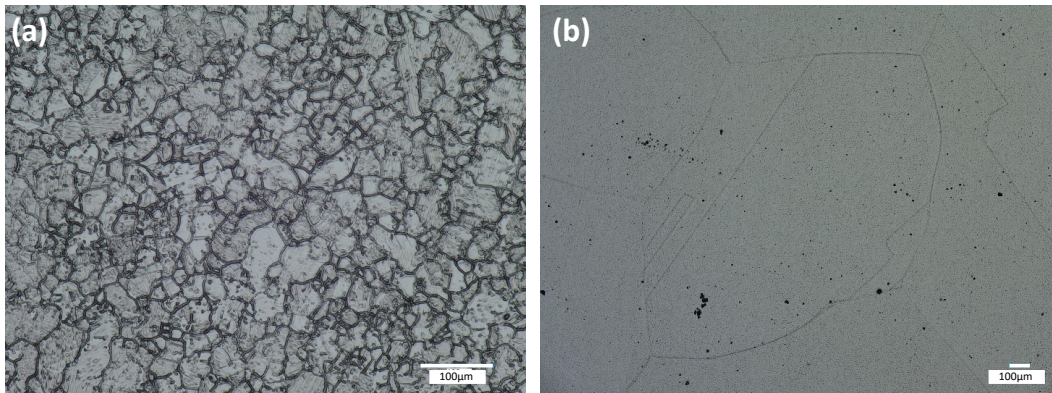
FIG. 46. Optical images of (a) fine grain and (b) large grain copper substrates that are used to coat Nb thin films.
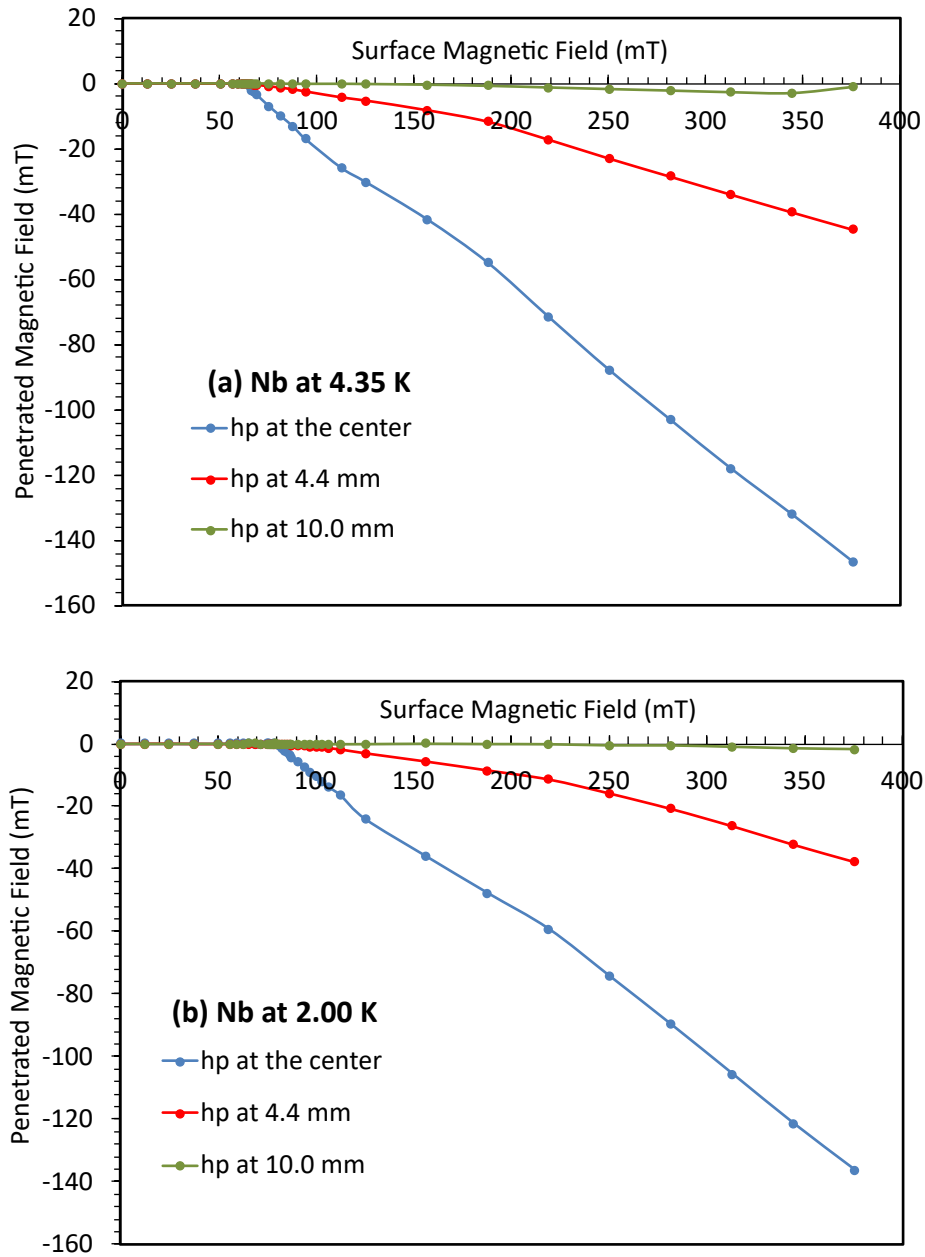
FIG. 47. Full flux penetration measured at (a) 4.35 K and (b) 2.00 K from the Hall probes at center, at 4.4 mm and at 10.00 mm on 3 um thick single crystal niobium (001) thin film fabricated on Al_2O_3 wafer with RRR=332 and T_c=9.31±0.03 K by Electron Cyclotron Resonance (ECR).
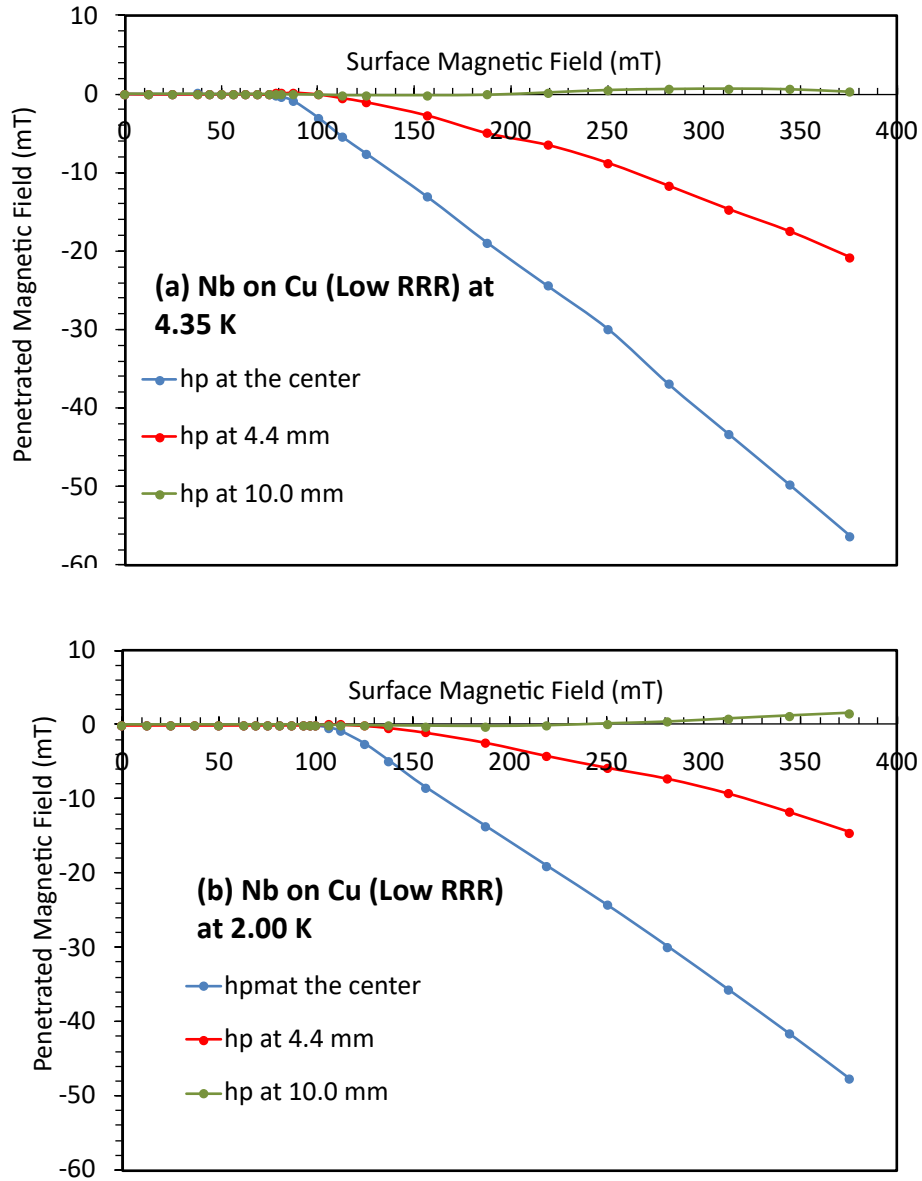
FIG. 48. Full flux penetration measured at (a) 4.35 K and (b) 2.00 K from the Hall probes at center, at 4.4 mm and at 10.00 mm on 1 um thick niobium thin film fabricated on large grain copper with RRR=34 and T_c=9.57±0.28 K by Electron Cyclotron Resonance (ECR).
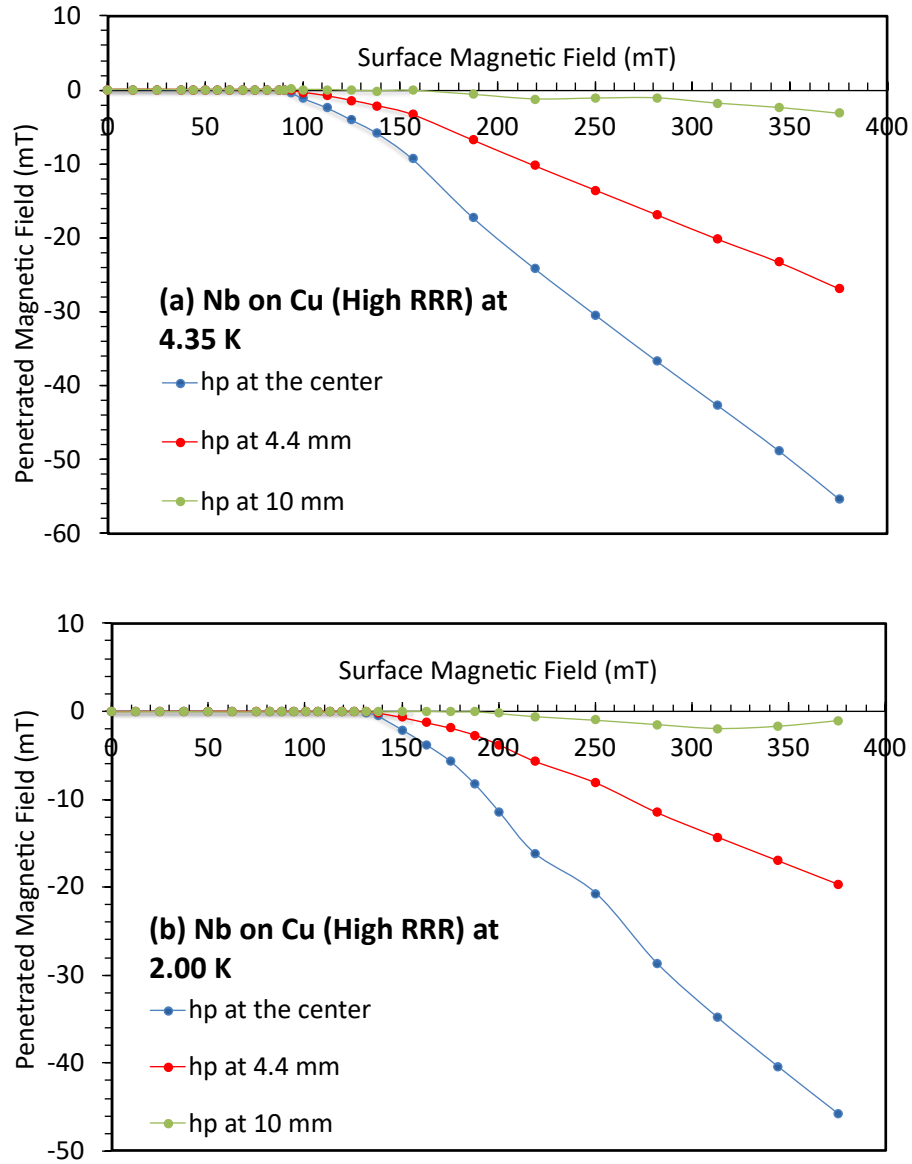
FIG. 49. Full flux penetration measured at (a) 4.35 K and (b) 2.00 K from the Hall probes at center, at 4.4 mm and at 10.00 mm on 1 um thick niobium thin film fabricated on large grain copper with RRR=190 and T_c=9.47±0.24 K by Electron Cyclotron Resonance (ECR).
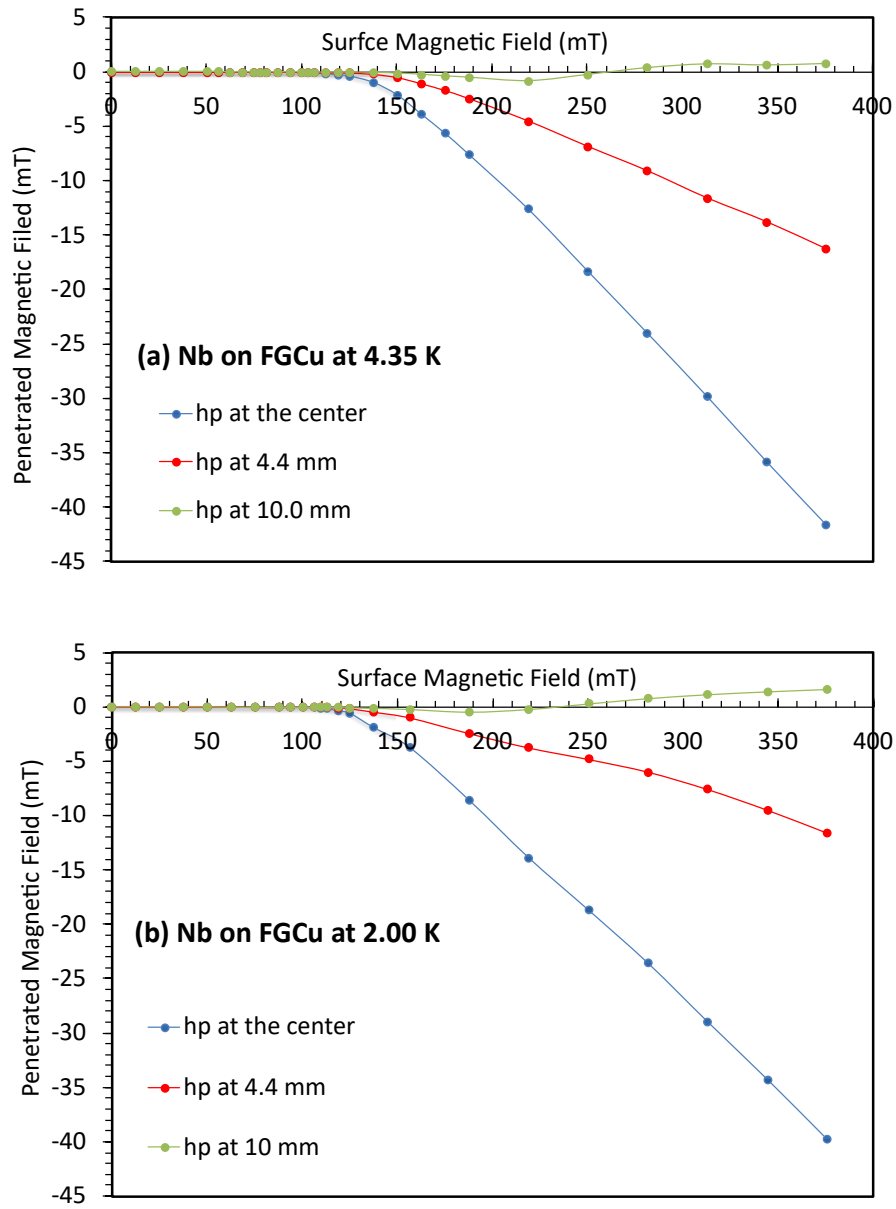
FIG. 50. Full flux penetration measured at (a) 4.35 K and (b) 2.00 K from the Hall probes at center, at 4.4 mm and at 10.00 mm on 1 um thick niobium thin film fabricated on fine grain copper with RRR=107 and T_c=9.43±0.10 K by Electron Cyclotron Resonance (ECR).

In addition, sample purity measured by RRR value is equally crucial when studying their high field behavior. Samples with the largest RRR have the fewest defect or impurity densities. Among samples measured in our experiment, the sample deposited onto a-plane sapphire exhibited the smallest normal state resistance of all samples just before the superconducting transition showing the highest RRR of about 332 and the superconducting transition temperature of 9.31±0.03 K. Eventhough it has a high RRR, it showed early flux penetration compared to other samples. When Nb thin film is coated on a copper substrate, that sample has the ability to transport heat efficiently due to the high thermal conductivity of the substrate.

The niobium film deposited onto copper displays a higher normal state resistance than that deposited onto a-plane sapphire and T_c of 9.57±0.28 K and 9.47±0.24 K for Nb deposited on LGCu 1 and LGCu 2 respectively and it is 9.43±0.10 K for Nb on FGCu. Also, the RRR of FG copper (grain size is a few tens of μm) was found to be lower than that of LG copper (grain size is in the mm range), possibly due to more dislocations in FG copper as shown in Fig.46. Sample purity is greatly influenced by grain structure due to the presence of intragranular impurities and can degrade SRF performance as they contribute to a reduction of the electron mean free path and the local lower critical field H_{c1}. Grains are separated by "weak-links" as the presence and diffusion of impurities at grain boundaries and intergranular oxidation, which impede the flow of surface supercurrents, creating a nonlinear loss mechanism [79]. These superconductively weak links are known as Josephson junctions. In our measurements, the first full flux penetration, B_p of Nb coated on LG copper is reduced with the low RRR. Impurities inside the grain reduces mean free path, l which reduces coherence length, $\xi = (l\xi_o)^{1/2}$ leads to suppress maximum field at superconducting phase ($B_p \propto \ln(1/\xi)$), which means the samples with less purity show early flux penetration.

The DC magnetic properties of bulk niobium can be explained relatively easily. The bulk niobium typically used for SRF cavity fabrication has large average size grains which leads to flux penetration through Josephson vortices that will be pinned at grain boundaries, converted to Abrikosov vortices in the grain boundaries and they move relatively easily across the sample thickness due to the lack of pinning centers.

The DC magnetic properties of thin films can be more complicated to explain. Josephson vortices still penetrate first into the thin film at the grain boundaries which typically contains defects and impurities but when the Abrikosov vortices enter the grain interior they become pinned and mixed state would be longer than bulk materials (higher H_{c2}). Grain boundaries in other promising SRF materials like Nb_3Sn are known to be less transparent to strong

magnetic fields than in Nb, because grain boundaries in Nb$_3$Sn are effective pinning centers for vortices. The magnetic field penetration is also affected by the film alignment with the magnetic field which greatly affects the field strength at which flux can enter the sample. Magnetic field penetrates a thin film at a maximum strength when the sample plane is aligned perfectly parallel to it. Thus, any small variation from parallel can lead to early penetration at smaller field and the transition to normal conducting becomes broader.

7.3 NIOBIUM TIN THIN FILMS

Our setup was used to measure B_p in Nb$_3$Sn films and multilayers. The Nb$_3$Sn thin film was grown on Al$_2$O$_3$ wafer by multilayer sequential sputtering at room temperature and then annealed at 950 °C by Nizam Sayeed at Jefferson Lab [80]. This thin film was fabricated by depositing alternative layers of Nb (20 nm thick) and Sn (10 nm thick) up to 50 cycles for 1.5 μm film on sapphire substrate and annealed it at 950 °C for 3 h in a vacuum furnace to form Nb$_3$Sn. The crystal structures of the films were analyzed by X-ray diffraction peaks as depicted in Fig. 51(a) Fig. 51(b) shows the resistance curve as a function of temperature measured by four-point probe method using a drive current of 10 mA, which gives transition temperature, T_c=17.85 K with ΔT_c=0.04 K. SEM and AFM images of the coated film are depicted in Fig. 51(c) and (d) respectively. The measured RMS roughness of the film is 34.65 nm. SEM image of the samples has clear grains with no visible Sn residue on the surface.

Stoichiometric Nb$_3$Sn multilayers with Al$_2$O$_3$ interlayers were grown on R-plane, 300 μm thick sapphire wafer by high-temperature confocal sputtering from elemental targets by Chris Sundahl at the University of Wisconsin-Madison. This multilayer contained four 60 nm Nb$_3$Sn layers separated by 6 nm Al$_2$O$_3$ interlayers, and a 200 nm thick Nb film was deposited on the back side of the Al$_2$O$_3$ wafer to prevent leakage of RF field during cavity measurements (Fig. 53(a)) [54]. Structural characterization is performed in Chris Sundahl et.al [54] shown in Fig. 53(a). Crosssectional scanning transmission electron microscopy (STEM) image represents the morphology and nanostructure of the Nb$_3$Sn/Al$_2$O$_3$ stack with fine interfaces as shown in Fig. 53 (b) and (c).
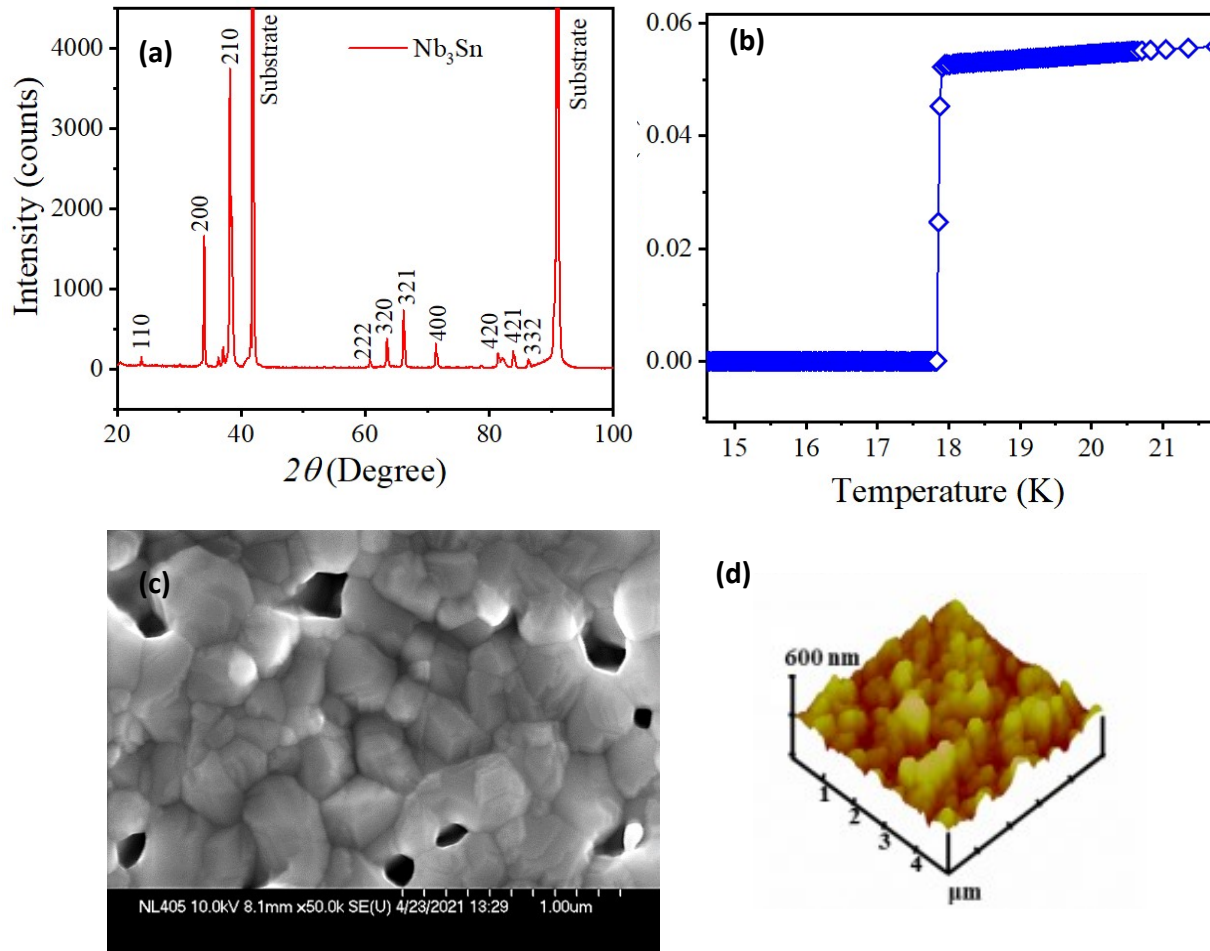
FIG. 51. (a) X-ray diffraction pattern (b) resistance vs temperature curve (c) SEM and (d) AFM images of 1.5 μm thick Nb_3Sn thin film grown on Al_2O_3 wafer by multilayer sequential sputtering at room temperature and annealed at 950 °C by Nizam Sayeed at Jefferson Lab [80]

We found that the measured flux penetration field can depend on the magnetic field ramp rate and the efficiency of heat transfer from the samples. For instance, at the magnetic field ramp rate of 3.13 mT/s (current ramp rate of 0.5 A/s), we observed a sequence of jumpwise penetrations of magnetic flux shown by the blue curves in Fig. 52 and 54. This behavior is indicative of partial thermomagnetic flux jumps caused by the positive feedback of the heat generated by moving vortices and the number of penetrating vortices [81, 82]. Here each step on Fig. 52 and 54 comes from a flux micro-avalanche originating at a surface defect.
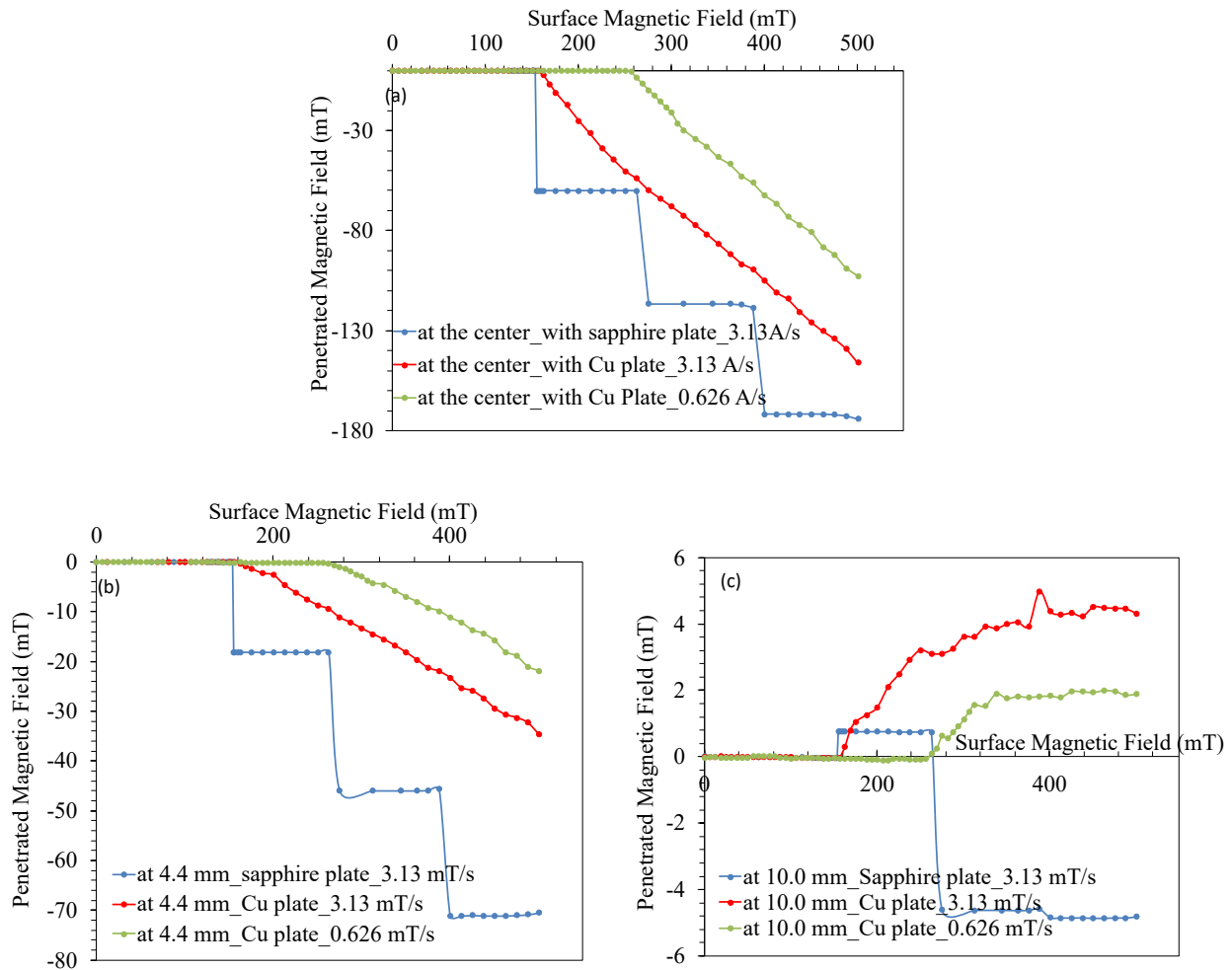
FIG. 52. Full flux penetration measured at 4.35 K from the Hall probes at center (a), at 4.4 mm (b) and at 10.00 mm (c) on 1.5 μm thick Nb_3Sn thin film grown on Al_2O_3 wafer by multilayer sequential sputtering at room temperature and annealed at 950 °C by Nizam Sayeed at Jefferson Lab [80]. Flux jumps were observed at a magnet ramp rate of 3.13 mT/s (blue curve). They disappeared when the sapphire separator plate is replaced by a copper plate (red curve). The field onset of flux penetration increased at slower ramp rate 0.626 mT/s (green curve).

Similar local avalanches were observed in computer simulations of dendritic flux penetration in superconducting films [83, 84]. Such partial flux jumps are more pronounced in Nb_3Sn as compared to Nb and Pb because of the much lower electrical and thermal conductivities of Nb_3Sn.

Furthermore, measurements of flux penetration on thin films are sensitive to surface or edge defects which can cause premature local penetration of vortices. In turn, the heat generated by penetrating vortices causes more vortices to enter the sample which produces more heat and eventually, a thermo-magnetic avalanche [81, 82]. Such partial local flux jumps are particularly pronounced at low temperatures as the specific heat $C(T) \propto T^3$ decreases with T.

In superconducting thin films thermo-magnetic instabilities result in propagation of fast dendritic flux avalanches [83–85], the field onset of these partial flux jumps decreasing as the magnetic ramp rate increases [81]. These thermomagnetic avalanches can be mitigated by reducing vortex dissipation and improving heat transfer from the sample, particularly by covering a superconducting film with a normal metallic film with high thermal and electric conductivities [85]. The flux jump mitigating measures in our setup were implemented by replacing the sapphire separator plate with a copper plate to improve the efficiency of heat transfer from the sample. As a result, the field jumps detected by the Hall probes disappear at a lower magnet ramp rate, as shown by the red curve in Fig. 52 and 54. Moreover, the field of full flux penetration increases as the ramp rate decreases as shown by the green curve, the observed B_p being well above B_{c1} in Nb_3Sn. The reduction of B_p by flux jumps can be particularly pronounced in such promising SRF materials as Nb_3Sn and superconducting pnictides which have 2-3 orders of magnitude lower thermal and electrical conductivities than Nb.

Investigation of the effect of ramp rate on the flux penetration field is important because it can reveal the relevance of partial flux jumps to the SRF breakdown in accelerator cavities, where the ramp rates of the rf field reach $\sim 10^9$ T/s. In this case, even a few vortex semi-loops penetrating at the surface defect can generate enough heat to ignite propagation of dendritic flux avalanche into the cavity wall. These effects are most pronounced in low conductive SRF materials like Nb_3Sn, which may contribute to the reduced breakdown field observed on Nb cavities coated with Nb_3Sn films as compared to the best Nb cavities [86]. Vortex avalanches can be mitigated by SIS multilayers blocking the propagation of vortex loops in the cavity wall. In that regard, the system described in this work can be useful to investigate the effect of the ramp rate on the penetration field and the ways B_p can be increased by
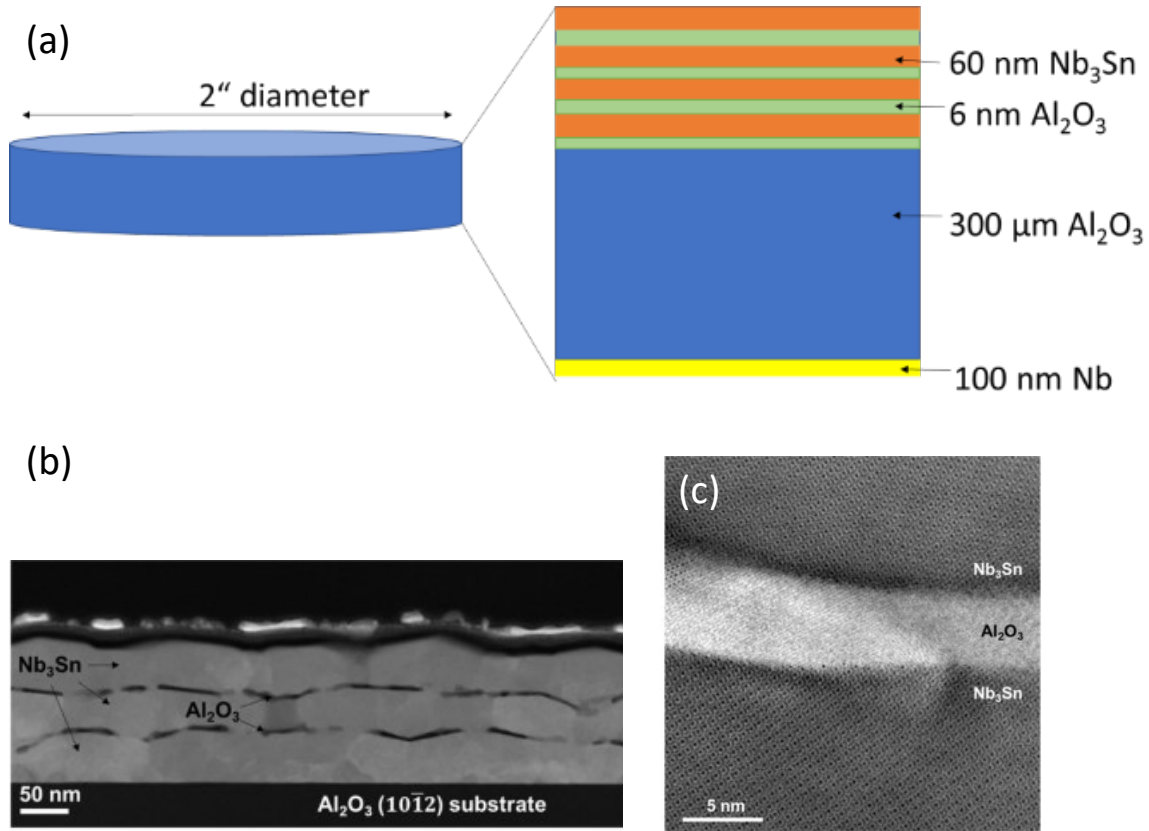
FIG. 53. (a) Schematic of Nb_3Sn/Al_2O_3 multilayer heterostructures grown on Al_2O_3 wafer by high-temperature confocal sputtering by Chris Sundahl at University of Wisconsin-Madison. This multilayer sample consists of four 60 nm Nb_3Sn layers separated by 6 nm Al_2O_3 interlayers. A 200 nm thick Nb film was deposited on the back side of the wafers to prevent leakage of RF field during cavity measurements and cross-sectional transmission electron microscopy images of Nb_3Sn/Al_2O_3 multilayer heterostructures (b) Low-magnification image of trilayer morphology (c) High-magnification image of the interfaces between Al_2O_3 and Nb_3Sn. Figures (b) and (c) are reproduced from [54].
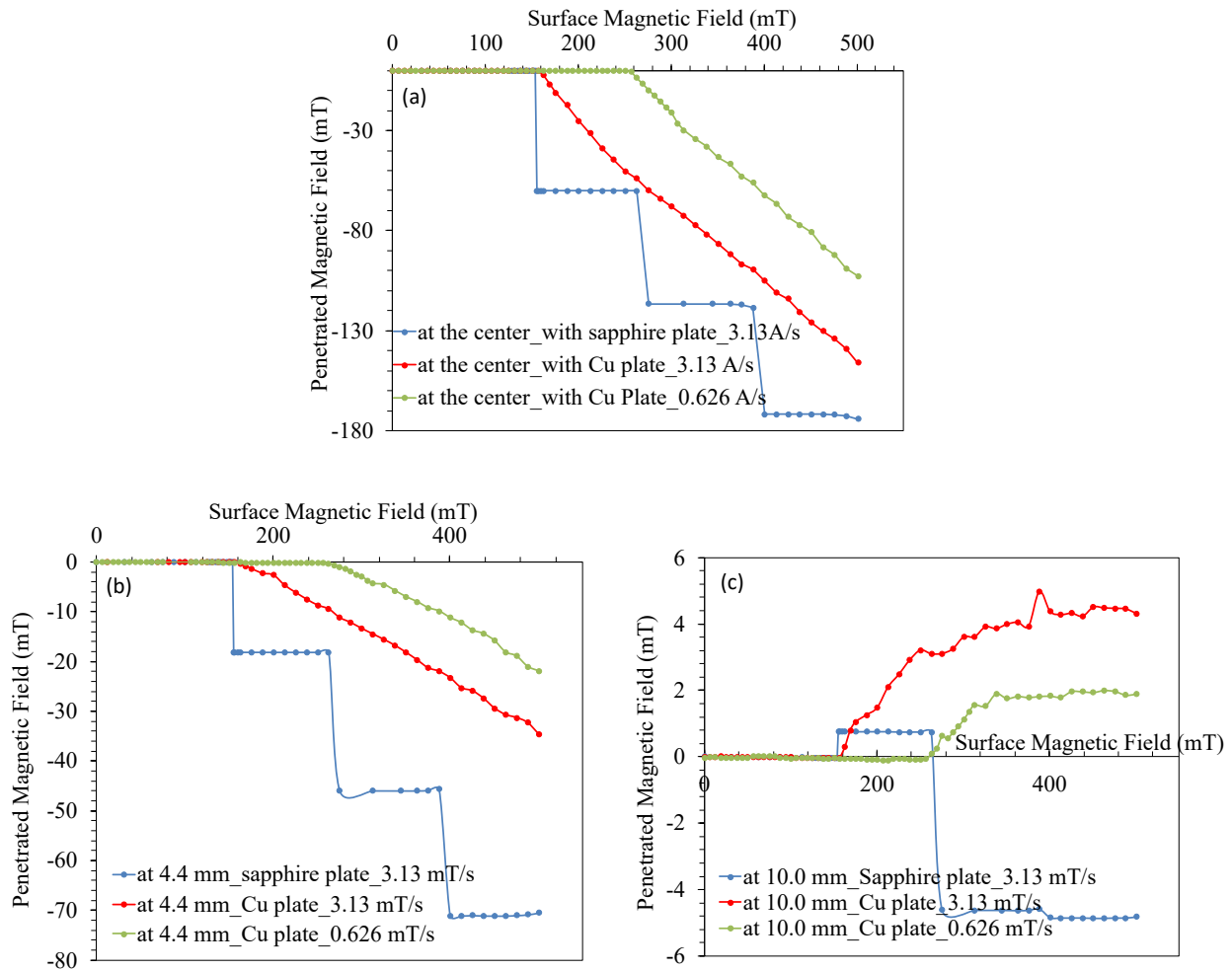
FIG. 54. Full flux penetration measured at 4.35 K from the Hall probes at the center (a), at 4.4 mm (b) and at 10.00 mm (c) on Nb_3Sn/Al_2O_3 multilayer grown on Al_2O_3 wafer by high-temperature confocal sputtering by Chris Sundahl at the University of Wisconsin-Madison [54]. This multilayer sample consists of four 125 nm Nb_3Sn layers separated by 6 nm Al_2O_3 interlayers. A 200 nm thick Nb film was deposited on the back side of the wafers to prevent leakage of RF field during cavity measurements. Flux jumps were observed at a magnet ramp rate of 3.13 mT/s (blue curve). They disappeared when the sapphire separator plate is replaced by a copper plate (red curve). The field onset of flux penetration increased at a slower ramp rate of 0.626 mT/s (green curve).

optimizing the film or multilayer geometry and improving heat transfer from local vortex hotspots. For Nb$_3$Sn thin films and Nb$_3$Sn/Al$_2$O$_3$ multilayers grown on sapphire substrates, we observed an increase of the field onset of flux penetration as the ramp rate decreases. The next chapter describes the measurements done on bulk Nb with SIS multilayers to achieve a higher breakdown field using our measurement system at a slower ramp rate to probe the superheating field of the material.

However, these measurements on thin superconducting films suggest that our MFP magnetometer has the capability for thin film measurements, especially to compare each other.

CHAPTER 8

MEASUREMENTS ON SIS MULTILAYERS ON BULK NIOBIUM

The SIS multilayers coated on bulk Nb is a effective structure to screen the surface of bulk Nb at higher magnetic field, there by higher accelerating gradient once implementing to the SRF cavities. In SIS multilayers the dielectric I-layers are very effective planar pinning centers which block the expansion of vortex semi-loops to the bulk. In the case of an ideal surface and S-I interfaces, the vortex semi-loops can break through the I-layers if the surface field becomes close to the superheating field $B_{sh} \gg B_{c1}$. In a more realistic situation B_{sh} can be locally reduced by surface materials defects, yet the measurements of field of first full flux penetration through the superconductor, B_p allows us to directly observe the enhancement of the magnetic breakdown field by a multilayer coted bulk Nb as compared to a bare with the same thickness. Here B_p quantifies the field magnitude by which the bulk of the Nb cavity is screened by a multilayer.

8.1 CANDIDATE MATERIALS: NbTiN AND AlN

In this work, NbTiN and AlN-based multilayers deposited on bulk Nb were studied for SRF accelerating cavity applications. NbTiN is a suitable S layer material for SIS structures which is a B1 compound with a critical temperature of 17.8 K. The T_c is very sensitive to the nitrogen (N) stoichiometry of NbN (superconducting phase of interest is cubic δ-phase, a=4.388 ^{o}A) and NbN is highly resistive due to the presence of randomly distributed metallic and gaseous vacancies. The presence of Ti results in NbTiN and it shows enhancing qualities of NbN with increasing Ti amount [87]. Its relative ease of fabrication and stability at room temperature makes it a convenient candidate to demonstrate the SIS concept. It has a NaCl structure where Ti and Nb form a face-centred cubic (fcc) lattice and N atoms occupy all the octahedral interstices. AlN is the chosen insulator due to its good insulating properties with high thermal conductivity at room temperature, 321 W/(m K) [88] comparable to Cu 385 W/(m K). That can be grown with a wurtzite hexagonal close-packed or sphalerite B1 cubic structures (similar to the NbTiN structure).

8.2 DEPOSITION

NbTiN and AlN thin layers are deposited on bulk Nb using reactive Direct Current Magnetron Sputtering (reDCMS) in an Ultra-High Vacuum (UHV) system with a base pressure of 10^{-10} Torr. The system is equipped with several DC magnetron sputtering guns with rotatable shutters. A NbTi target with Nb/Ti weight ratios: 80/20 (wt.%) and a pure Al target are used to deposit the NbTiN/AlN SIS structures. The Nb substrates are prepared by buffered chemical polishing (BCP), electropolishing (EP), or mechanical polishing (MP). Multiple Nb substrates with a 2-inch diameter and 250 μm (or 150 μm) thickness were used as substrates along with witness samples and MgO plates that are used to probe the films' quality and their properties. MgO is a single crystal with a lattice parameter of 4.36 Å which closely matches NbTiN (4.34 Å). This substrate provides an excellent surface for film growth, yielding high quality NbTiN films, that were used to measure resistance with respect to the temperature of the film. The films were deposited in the same run to ensure identical environmental conditions in one parameter study. The films were deposited at 450 °C on bulk Nb after a 24-hour bake at 600°C, then post-annealed at 450 °C for 4 hours. Even though bulk-like properties can be achieved at the deposition temperature of 600 °C, both for NbTiN, highest T_c and AlN, more pronounced dielectric properties, the successive deposition of these layers on top of each other requires the temperature to be reduced to 450 °C to limit Al diffusion into Nb and NbTiN which results in amorphous structures and diffuse interfaces. The deposition method was optimized to deposit the superconductor and insulator layers on bulk substrates and on top of each other maintaining the quality and properties of each layer and of the base substrate [87, 89].

8.3 MAXIMUM ACHIEVABLE PEAK SURFACE FIELD

The magnetic penetration shielding of SIS structures can be measured by the MFP magnetometer. The magnetic shielding of layers to bulk Nb depends on the thickness of the superconducting layer. A thinner superconducting layer (a few hundred nm) can withstand higher fields but more of the applied field will reach the bulk superconductor. A thicker superconducting layer cannot withstand high fields but will attenuate the applied field more before it reaches the bulk superconductor. The maximum surface field, H_m, that exceeds the superheating field of both S layer material and Nb substrate relies on the optimum thickness of the superconducting layer was calculated in [14] and given by

$$d_m = \lambda \ln(\mu + \sqrt{\mu^2 + k}),$$

where $\mu = H_{sh}\lambda/(\lambda + \lambda_o)H_{sho}$ and $k = (\lambda - \lambda_o)/(\lambda + \lambda_o) > 0$. λ and λ_o are the penetration depths and H_{sh} and H_{sho} are the superheating fields of layer material and substrate (Nb). When S layer is NbTiN (λ=150-200 nm [11], H_{sh}= 339 nm [90]) and substrate is Nb (λ=40 nm, H_{sh}= 240 nm [20]), d_m is in the range 135 - 192 nm. λ of NbTiN also depends on the temperature and the layer thickness [91].
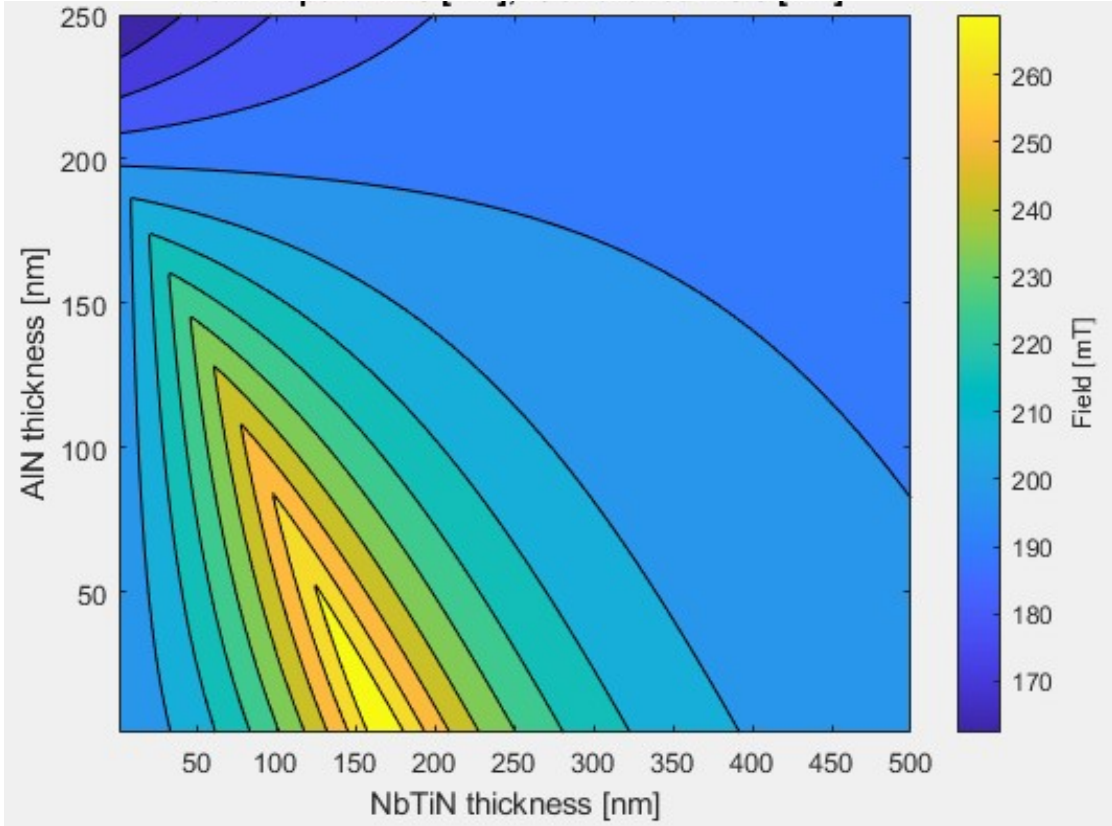
FIG. 55. A Contour plot of the maximum achievable peak surface-field, B_v without vortex dissipations for NbTiN/AlN on bulk Nb structure assuming penetration depth =240 nm and coherence lengh=3.5 nm of NbTiN layer and penetration depth =40 nm and B_v =200 mT (breakdown field) for bulk Nb.

The model in Ref. [92], the optimum thickness of the superconducting layer and the insulating layer are extracted from the contour plot of the maximum achievable peak surface field (superheating field) (B_v) without vortex dissipation for SI structure on Nb. The contour plot shown in Fig. 55 was calculated using the equations from Ref. [92] and assumes London penetration depth = 240 nm and coherence length of 3.5 nm of NbTiN layer. These calculations are performed on the ideal superconductor and insulator. In real situations, the substrate Nb includes defects and surface roughnesses, which affects directly to thickness of both layers.

In this work, B_p was measured for NbTiN/AlN coated on bulk Nb with different S layer thickness by managing insulator layer thickness as 10 nm. But there will not be any significant effect to B_p by slight change in thickness of insulating layer.

8.4 MEASUREMENTS OF MULTILAYERS ON BULK NIOBIUM

8.4.1 MONOLAYER NbTiN

In the SIS structure concept, the superconducting films need to have a thickness smaller than the material's penetration depth. It is important to investigate how the thickness affects the properties of the film. Our first attempt was to test monolayer NbTiN coated on bulk Nb to study the B_p measurements using the MPF magnetometer. Two thin films with thickness 75 nm and 149 nm were coated on chemically poli shed bulk Nb. Thickness was measured using witness samples. The crystallographic structures of deposited thin films were examined by X-ray diffraction (XRD) analysis. High-angle X-ray diffraction measurements provide information about the crystalline relations between the substrate and the deposited layers. The NbTiN crystal structure contains 200 and 220 crystal orientations (Fig. 56(a)). Electron backscatter diffraction (EBSD) indicates multi crystal nature of the deposited film on bulk Nb as shown in Fig. 56(b), shows a higher quality crystal structure.

Table 6 describes the NbTiN transition temperatures extracted from resistivity measurements on deposited thin films.

TABLE 6. Thicknesses of NbTiN layer and transition temperatures

Sample No.	Thickness	T_c (K)	ΔT_c (K)
1	75	16.2	0.40
2	149	16.3	0.30

The resistances of the films were measured from 4.5 to 300 K using standard four-point probe method. As shown in Fig. 57, a sharp resistance decrease observed for monolayer NbTiN on bulk Nb around 16.2 K, indicates good quality of the film. T_c would be close to accepted T_c= 17.8 K for bulk films with micrometer thickness.

Fig. 57 and 58 show the penetrating magnetic fields detected by three Hall probes as a function of the surface field at 4.35 and 2.00 K, respectively. All three hall probes detected first signal at the same time, but Hall probe mounted at center and 10 mm from the center read negative and positive signal respectively with increasing magnet current, while Hall probe at 4.4 mm showed positive signal first and eventually detected negative signal.

SI structure with NbTiN layer thickness is 75 nm shows 16.4 % and 23.2 % of percentage increase compared to bare Nb at 4.35 K and 2.00 K respectively. When the thickness is doubled (149 nm), percentage increase enhanced to 21.9 % at 4.35 K and to 27.5 % at 2.00 K.
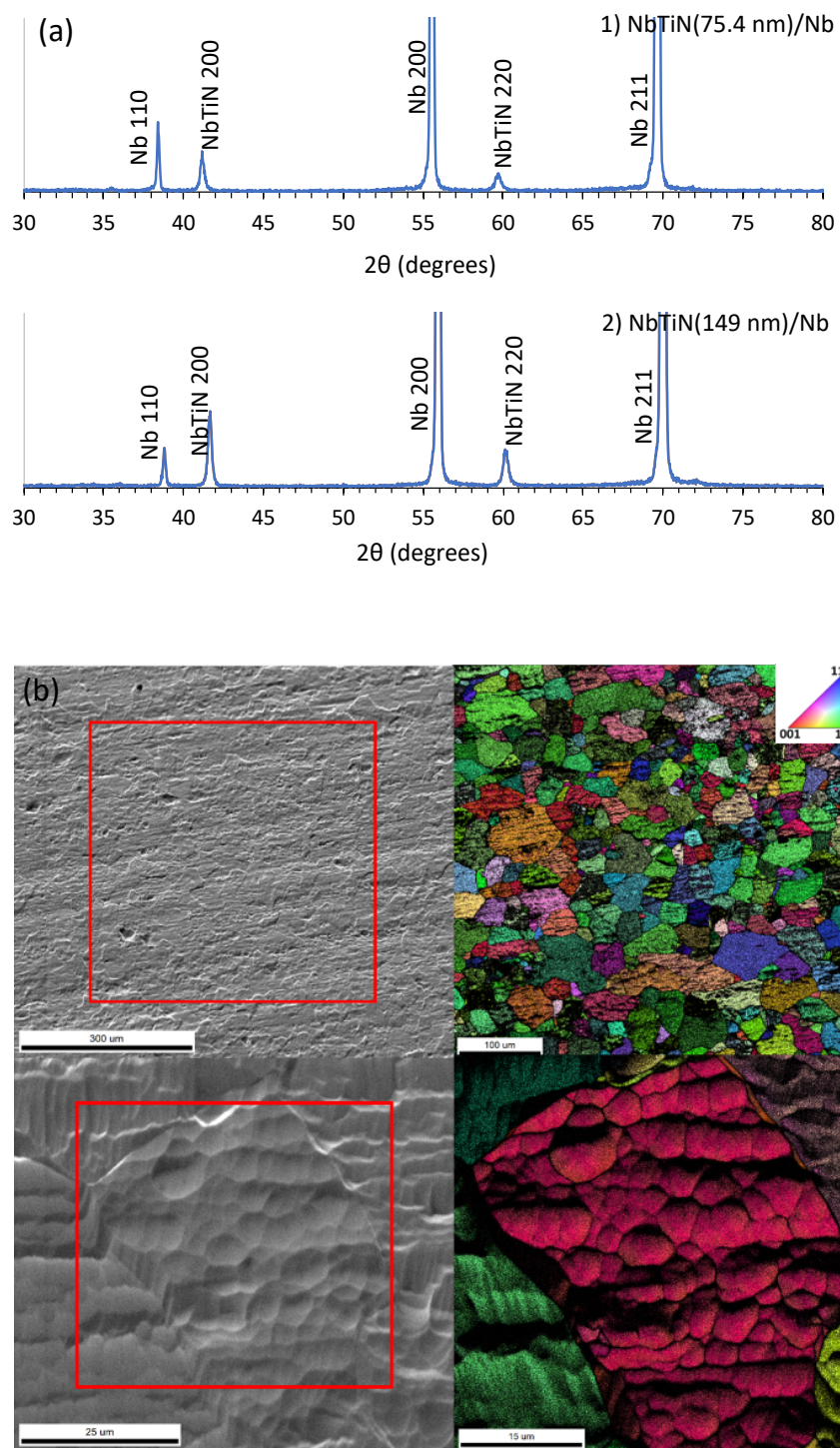
FIG. 56. (a) XRD scans and (b) SEM images and relevant Inverse Pole Figure (IPF) map from EBSD showing the poly-crystallinity of films for monolayer NbTiN structure coated on BCP bulk niobium. The IPF map is filtered for confidence index above 0.1.
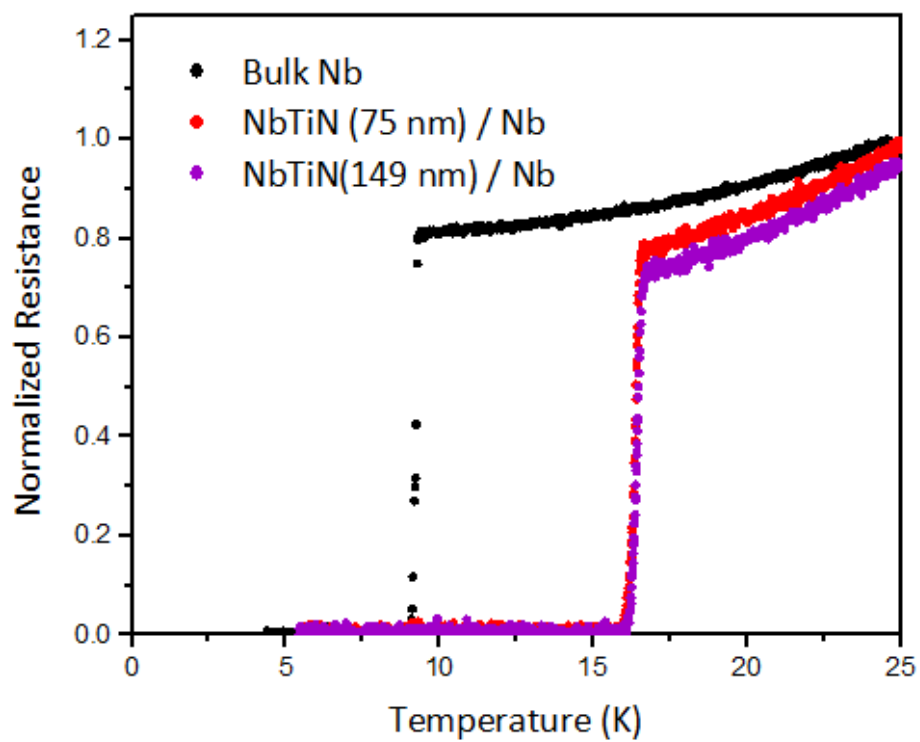
FIG. 57. DC resistance as a function of temperature for NbTiN layer with thickness 75 nm and 149 nm on BCP bulk niobium substrates.
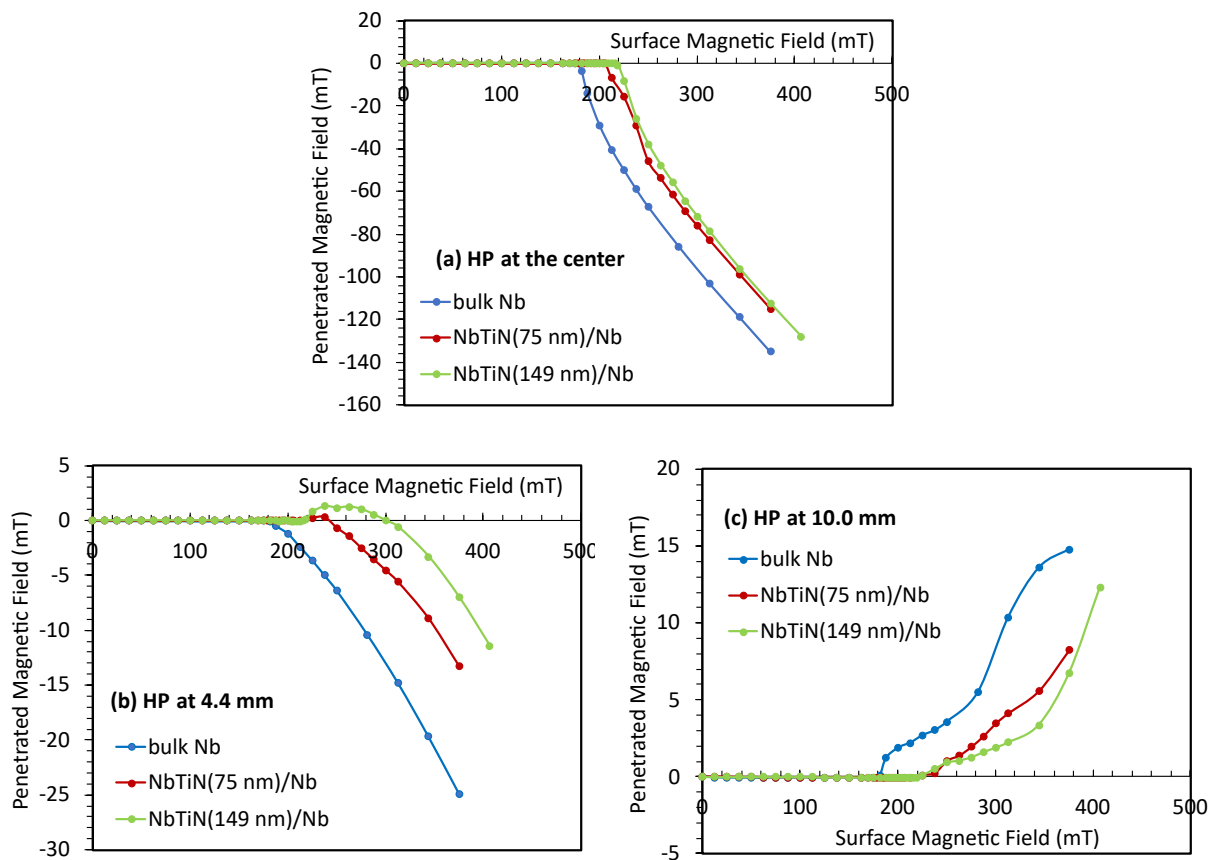
FIG. 58. Penetrated magnetic field detected by Hall probe at the (a) center (b) 4.4 mm and (c) 10.0 mm from the center at 4.35 K for NbTiN monolayers deposited on bulk Nb.
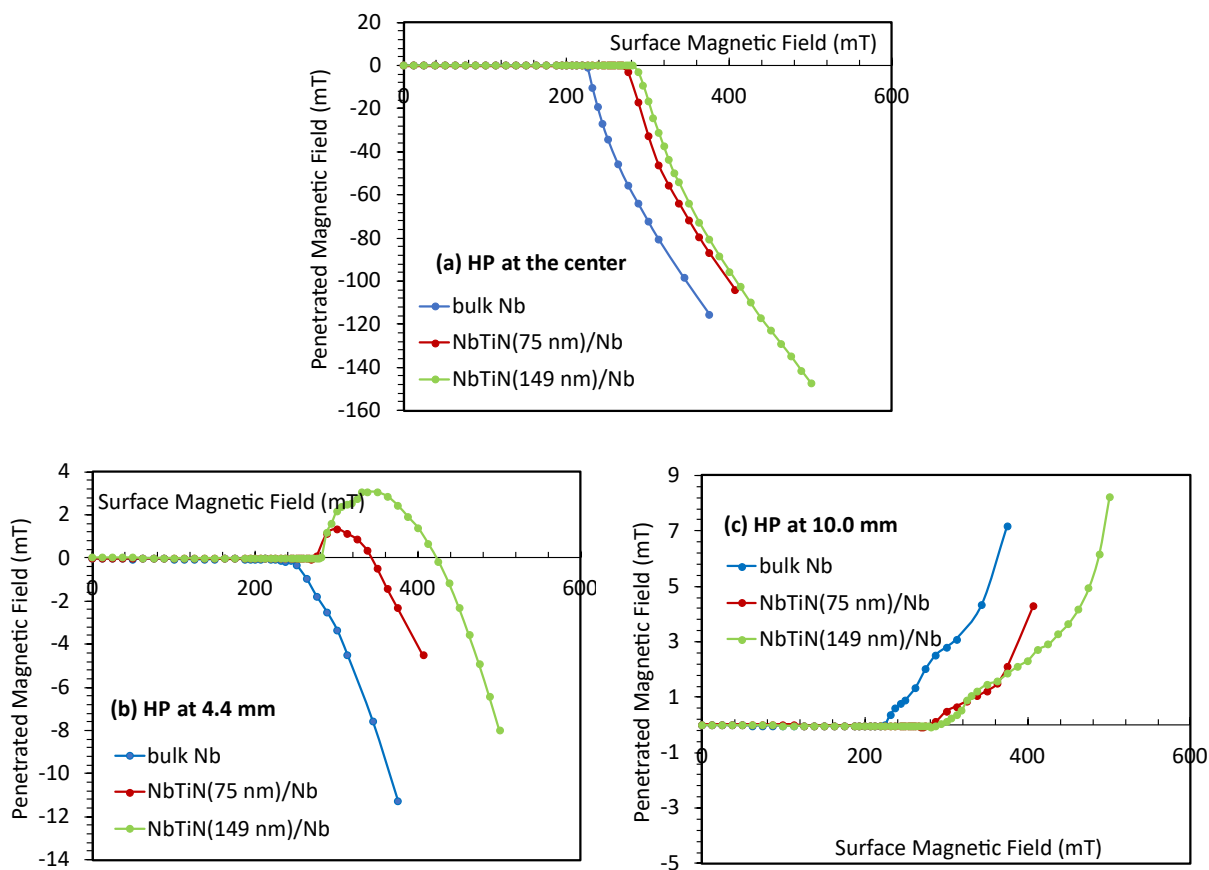
FIG. 59. Penetrated magnetic field detected by Hall probe at the (a) center (b) 4.4 mm and (c) 10.0 mm from the center at 2.00 K for NbTiN monolayers deposited on bulk Nb.

8.4.2 NbTiN AND AlN BILAYER

Then MFP magnetometer measurements were carried out with NbTiN layered on bulk Nb with AlN ($\sim$ 10 nm) interlayer. The objective was to study the variation of B_p with respect to different S layer thicknesses maintaining constant I layer thickness. Table 7 shows the dimensional characteristics of the NbTiN layers along with T_c taken from resistance vs temperature measurements shown in Fig. 60 for each coating. DC resistive transition of the bilayer films is broad, but showing transition for both Nb and NbTiN. T_c ranged from 14.5 to 16 K (the bulk value was 17.8 K). Low T_c values are often observed for very thin films due to their high defect density and their lower mean free paths caused by the impurities.

XRD analysis is shown in Fig. 61 revealed that NbTiN/AlN layers is in good relationship with the Nb substrate showing NbTiN (200 and 220) and AlN (002) peaks. EBSD images in Fig. 62 confirm the multicrystal nature of the deposited films on bulk Nb, but not as clear as monolayer NbTiN on Nb, possibly due to presence of AlN layer with rippled interfaces on the rough chemically polished (BCP) Nb substrate, Morphological features on their surface are shown in SEM images. Thicknesses of the thin film may not be uniform and differ slightly from the expected values estimated from deposition rates due to the rough substrate.

TABLE 7. Thicknesses of NbTiN layer and transition temperatures. Here AlN layer thickness of sample 3 is $\sim$ 5 nm and $\sim$10 nm for others.

Sample No.	Thickness	T_c (K)	ΔT_c (K)
3	83.5	14.5	1.47
4	83.0	14.4	1.49
5	166.0	15.7	0.79
6	250.0	12.2	0.74
7	371.0	13.9	0.09
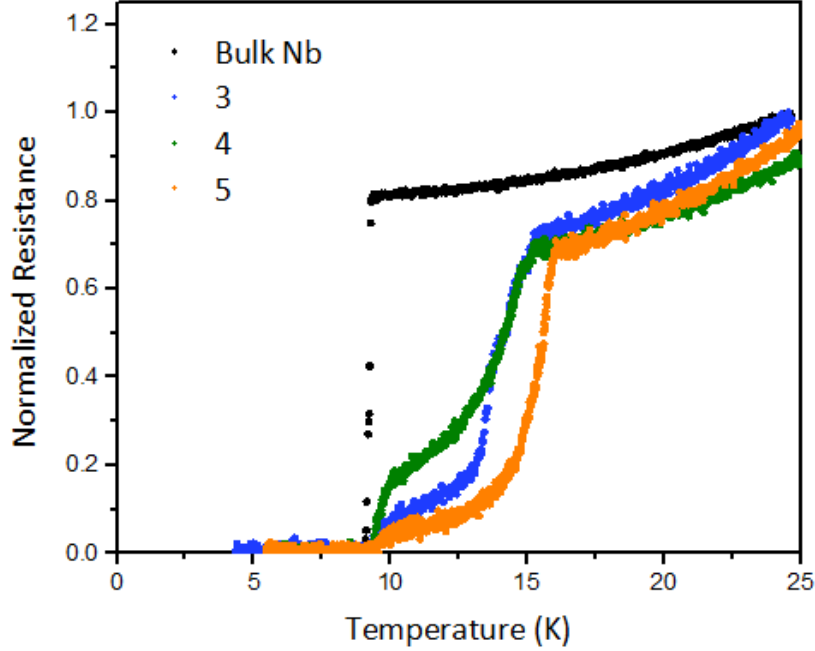
FIG. 60. Normalized resistance as a function of temperature for some of NbTiN/AlN thin films coated on BCP bulk Nb.

The MFP magnetometer was used to measure fabricated SIS samples to investigate the so-called screening effect at higher fields. Results of field penetration measurements are shown in Fig. 63 (at 4.35 K) and 64 (at 2.00 K) represents the enhanced B_p of NbTiN/AlN multilayers deposited on BCP bulk Nb compared to bare Nb, that demonstrates multilayer's ability to screen the bulk Nb at higher field. The penetrated magnetic field profile along the sample radius observed from three Hall probes is the same as it was for single-layer NbTiN on bulk Nb. Moreover, Optical microscope observation confirmed that samples were intact during the testing and can be used for repeating testing or another study.

The most interesting result observed in this experiment is depicted in Fig. 65(a), the variation of the field at first full flux penetration, B_p against NbTiN layer thickness while the AlN layer is constant $\sim$ 10 nm. B_p is thickness dependent as expected, which allows identifying optimum thickness for maximum B_p. Fig. 65(b) extracted from contour plot in Fig. 55 (for penetration depth=240 nm and coherence length=3.5 nm) that is the variation of maximum achievable field, B_v with respect to NbTiN layer thickness while the AlN layer
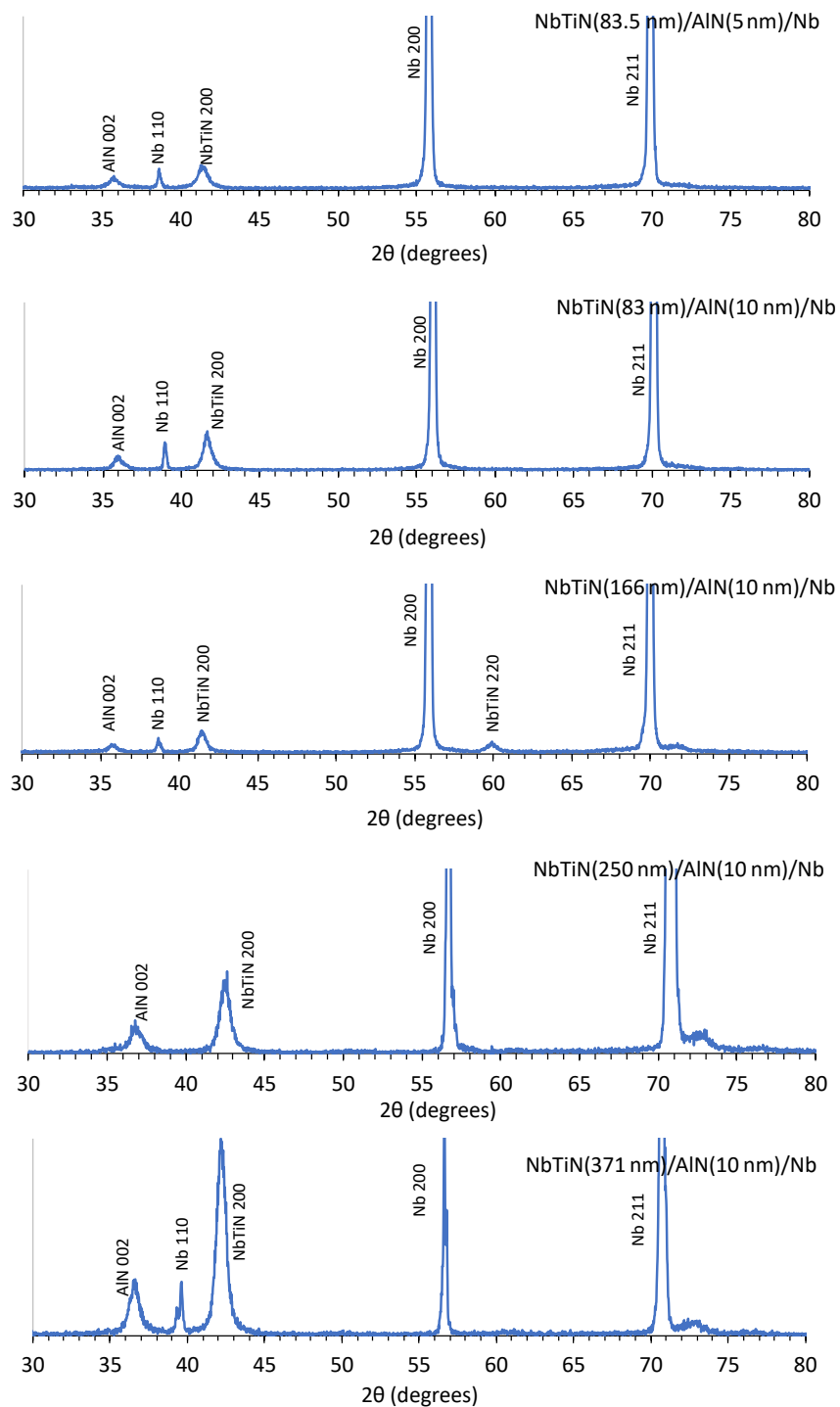
FIG. 61. XRD analysis for NbTiN/AlN structure coated on bulk Nb showing NbTiN (200 and 220) and AlN (002) peaks.
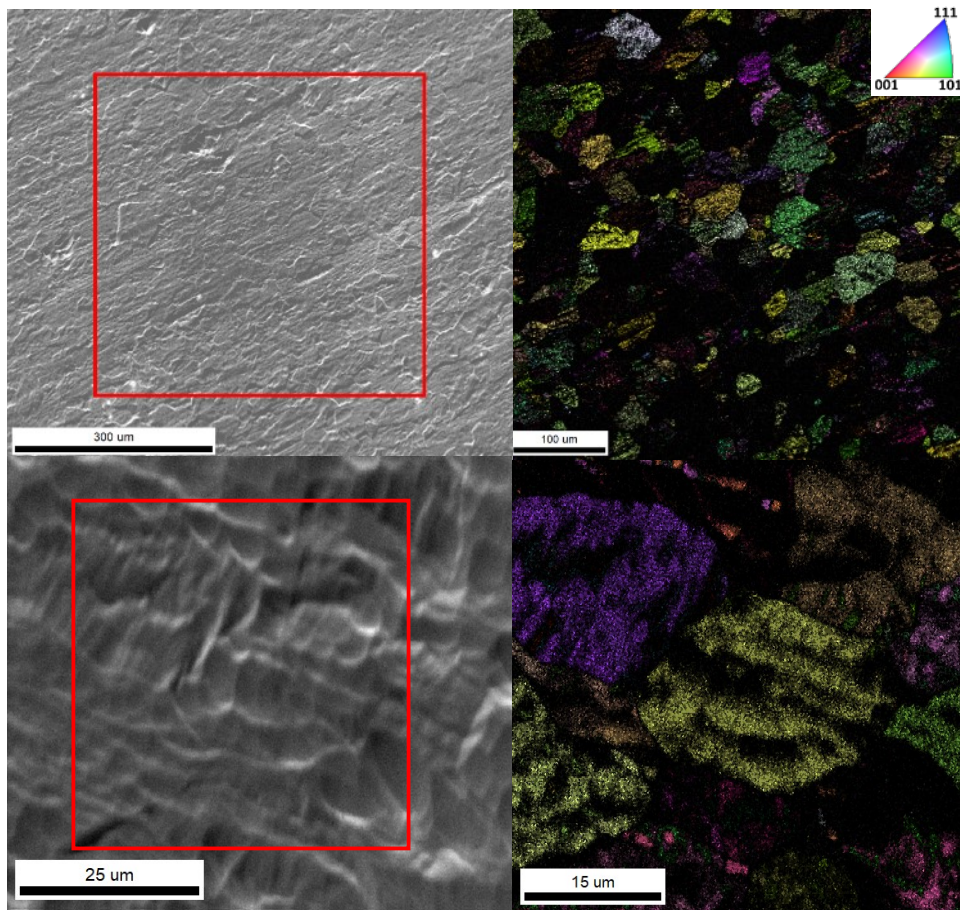
FIG. 62. SEM images and relevant Inverse Pole Figure (IPF) map from EBSD showing the poly-crystallinity of films for NbTiN/AlN structure coated on BCP bulk niobium. The IPF map is filtered for confidence index above 0.1.
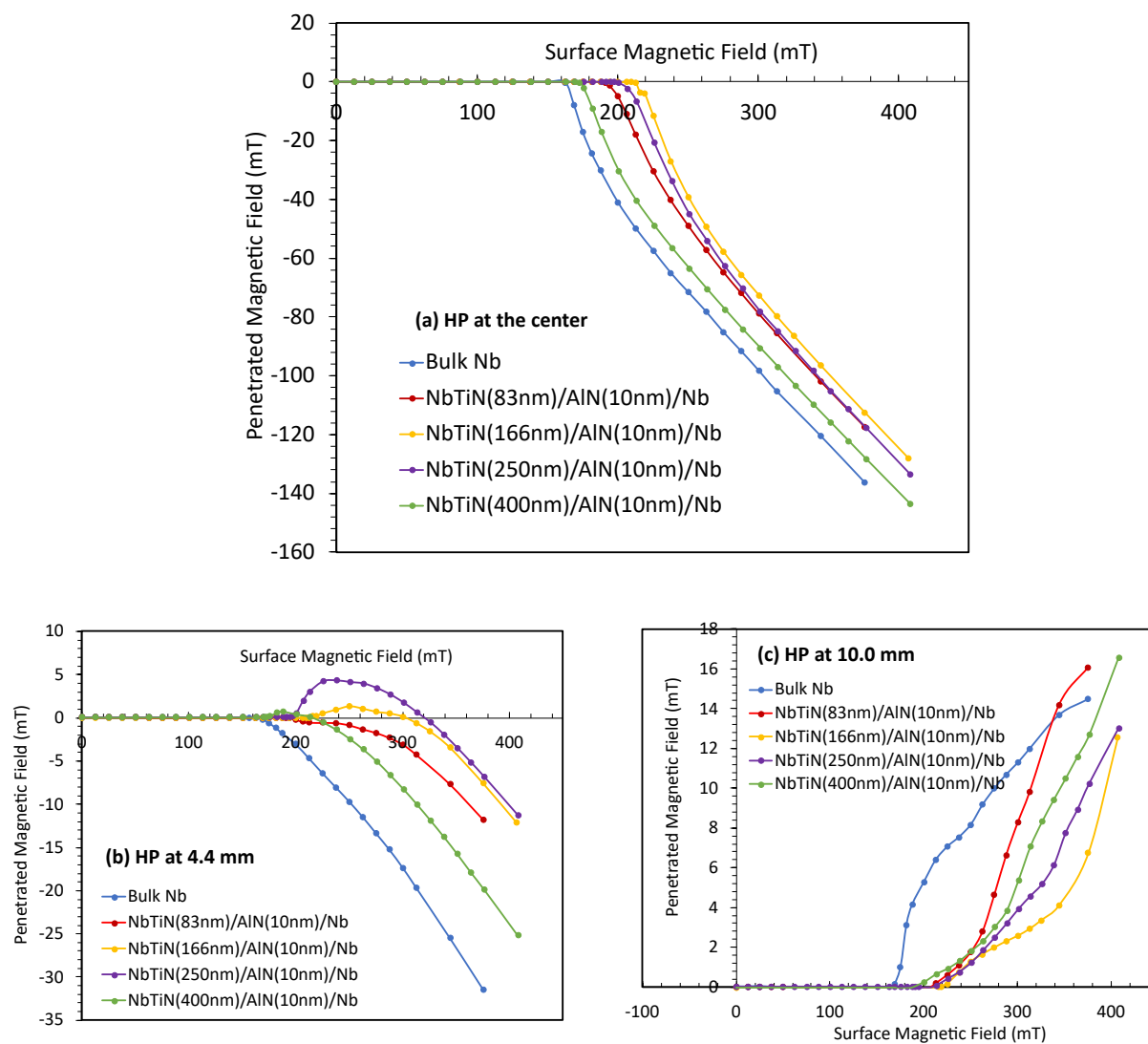
FIG. 63. Penetrated magnetic field detected by Hall probe at the (a) center (b) 4.4 mm and (c) 10.0 mm from the center for NbTiN/AlN deposited on bulk Nb at 4.35 K.
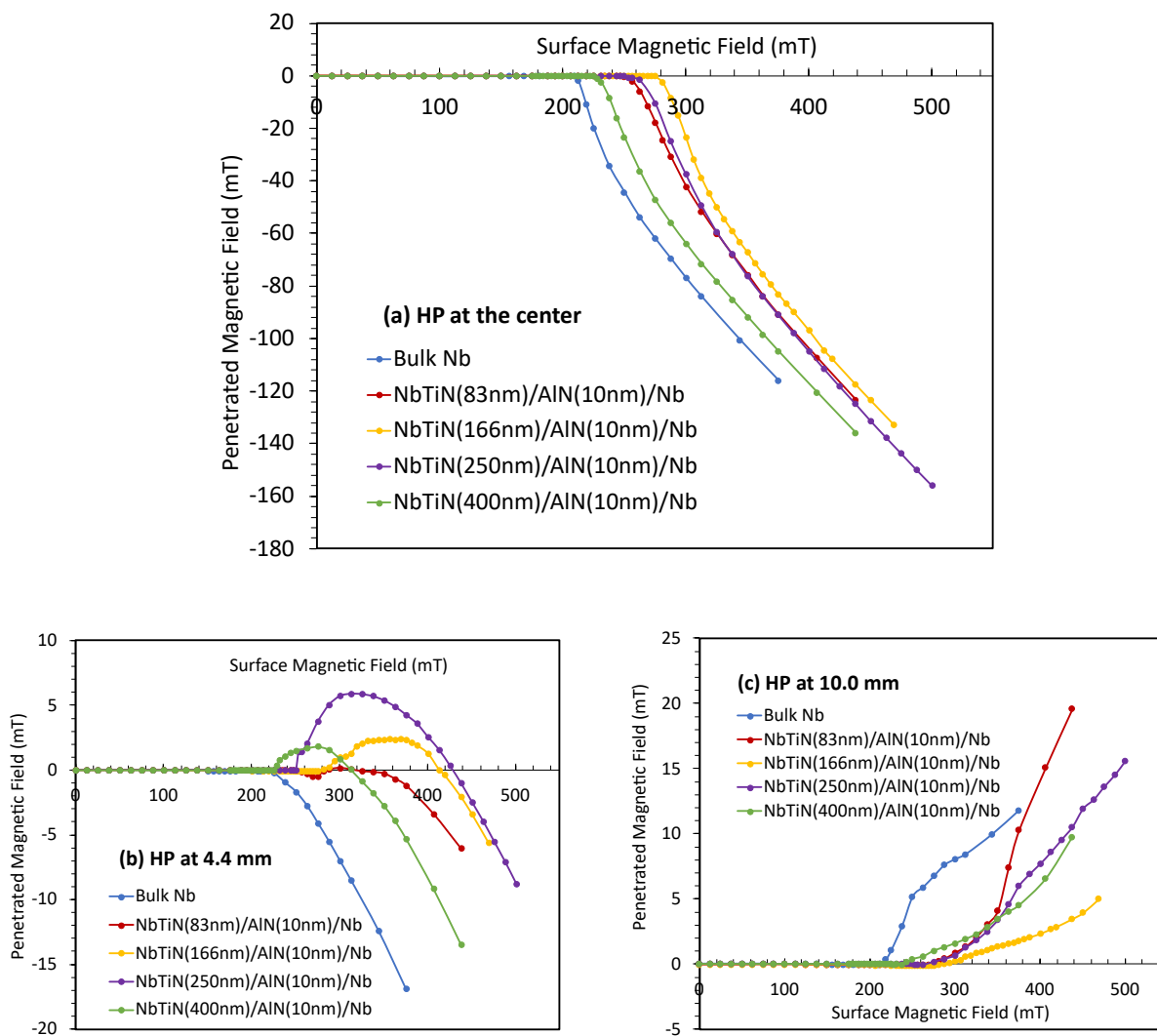
FIG. 64. Penetrated magnetic field detected by Hall probe at the (a) center (b) 4.4 mm and (c) 10.0 mm from the center for NbTiN/AlN deposited on bulk Nb at 2.00 K.
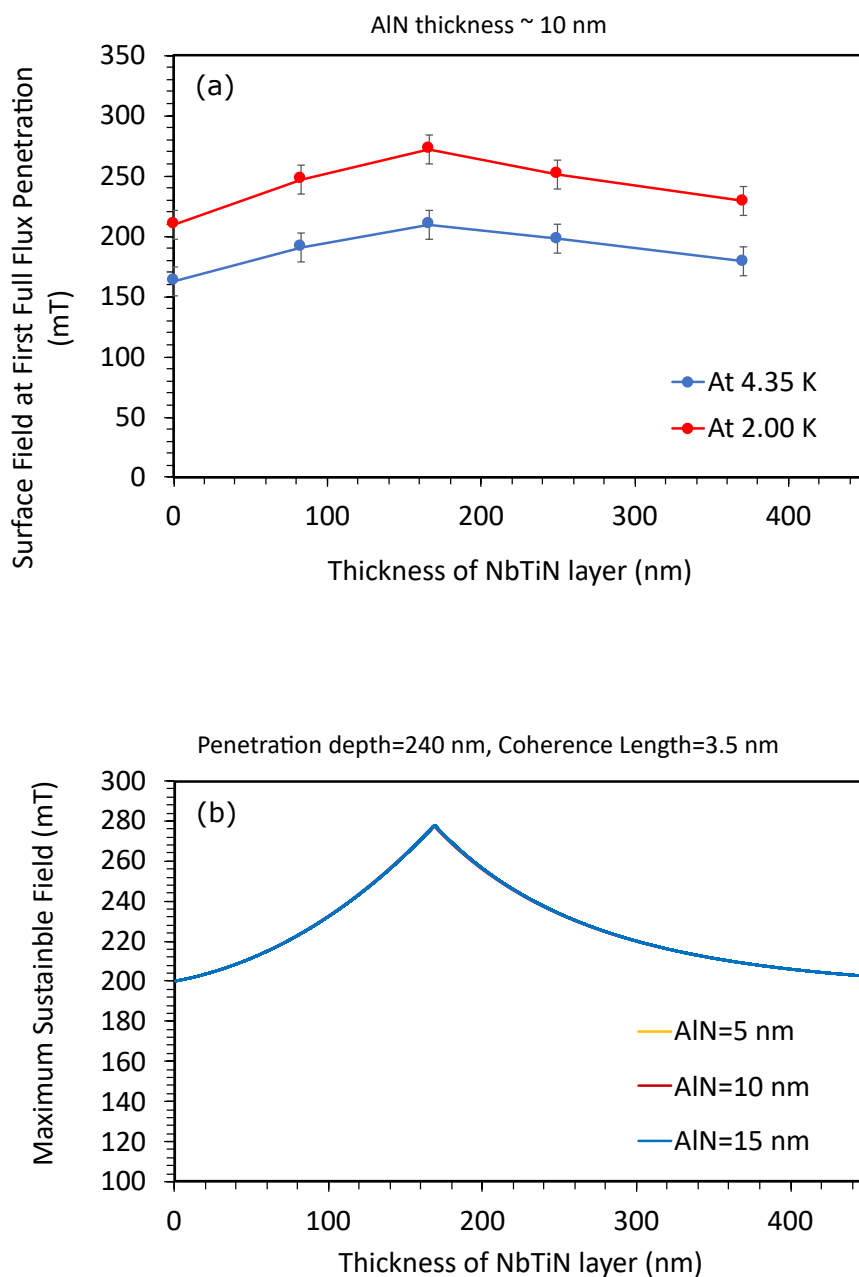
FIG. 65. (a) Experimental data for the surface field at first full flux penetration, B_p at 4.35 K and 2.00 K for different NbTiN layer thickness maintaining constant AlN layer thickness $\sim$ 10 nm (b) Theoretical curves (penetration depth 240 nm and coherence length=3.5 nm) show the variation of maximum achievable peak surface field with the NbTiN layer thickness for constant AlN layer thickness. Curves for AlN thickness 5, 10, and 15 nm overlap each other which shows the slight variation of the AlN layer does not affect to the results much.
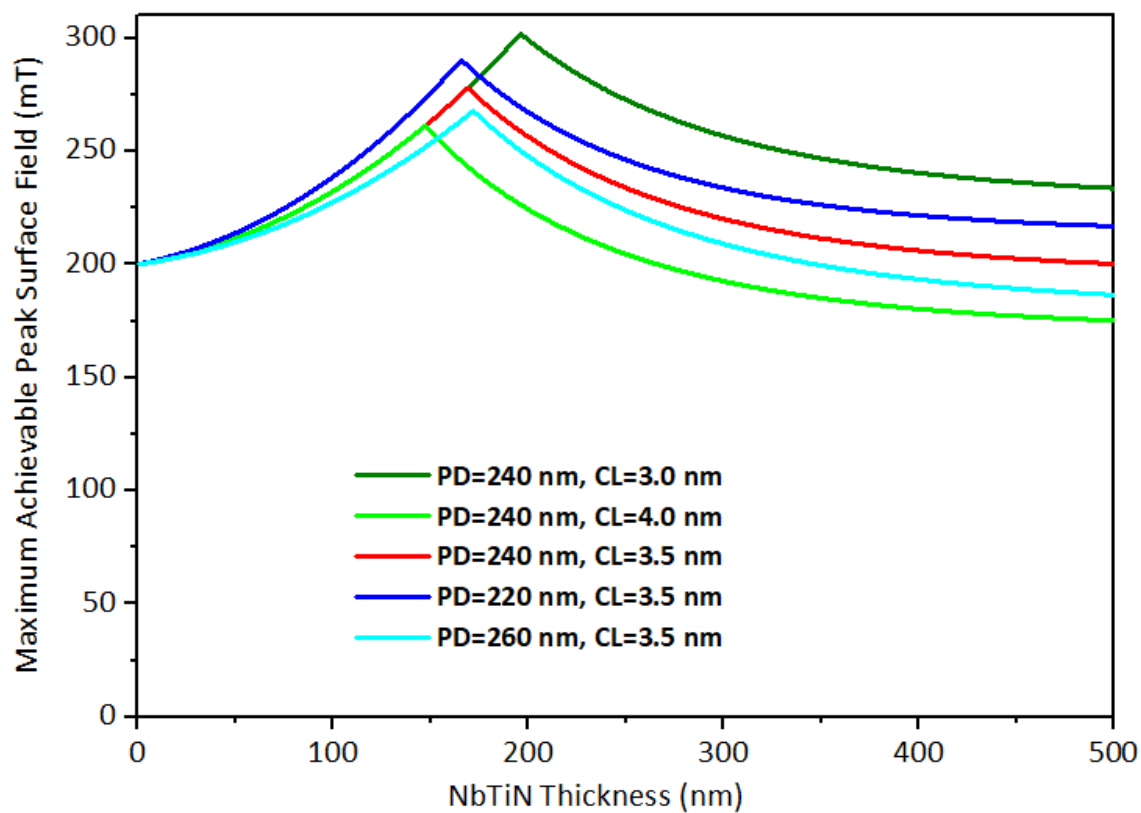
FIG. 66. Theoretical curves exhibits the variation of maximum achievable peak surface field with NbTiN thickness for slight deviation of penetration depth (PD) and coherence length (CL).

is constant. This model is based on calculations performed on the ideal superconductor and insulator. In real situations, the Nb substrate includes defects and surface roughnesses, which affect directly the B_p measurements.

Nevertheless, the model qualitatively agrees with the results obtained for single layer NbTiN on bulk Nb with a single AlN interlayer. The AlN layer thickness was managed to be constant for all four samples, but a slight change in thickness would not make any significant changes. Moreover, the contour plots shown in Ref. [60, 92] were obtained for the defect free NbN layer on bulk Nb and the maximum field withstands for 10 nm thick insulator layer in between. Therefore the dielectric layer thickness is limited to $\sim$ 10 nm is an acceptable selection. Among the four samples tested, the maximum B_p was detected on the sample with the 166 nm thick NbTiN layer. This matches the contour plot for penetration depth, λ= 240 nm, and coherence length, ξ= 3.5 nm. However, λ and ξ are exactly not known for our samples. As shown in Fig. 66 model predicts how the peak of B_v curve varies with λ and ξ of the NbTiN thin film. The peak of the curve moves towards the right and increases with decreasing ξ and moves towards the left and increases with decreasing λ.

In Ref. [92], Maximum achievable field is described by

$$B_v = \frac{\phi_o}{4\pi\lambda_s\xi_s} \frac{\cosh\frac{d_s}{\lambda_s} + \left(\frac{\lambda_{Nb}+d_I}{\lambda_s}\right)\sinh\frac{d_s}{\lambda_s}}{\sinh\frac{d_s}{\lambda_s} + \left(\frac{\lambda_{Nb}+d_I}{\lambda_s}\right)\cosh\frac{d_s}{\lambda_s}}. \tag{77}$$

When ϕ_o= 2.07 × 10^{15} Wb, λ_s= 240 nm, ξ_s=3.5 nm, λ_{Nb}= 40 nm d_s=166 nm and d_I= 10 nm, B_v is calculated as 273.17 mT. The peak maximum of B_v of the contour plot shown in Fig. 65(b) for d_I= 10 nm is 276.81 mT when optimum d_s= 161 nm. This tells that 166 nm is close to the optimum thickness of the NbTiN layer when the AlN layer is 10 nm thick. At optimum S layer thickness, nearly 25 % increase of B_p was observed. However, with SIS system having a single NbTiN (with optimum thickness) and a single AlN interlayer on Nb yields 25 % increase compared to the bare substrate. If there is a stack of bilayers on bulk Nb, B_p will be enhanced to a great extent.

The depairing current density

$$J_d = \frac{B_p}{\mu_o\lambda_s}. \tag{78}$$

This yields $J_d = 9.06 \times 10^{11}$ Am^{-2}, that is way higher than J_d calculated for bulk Nb in chapter 6.2. Also, this agrees with the reported values of NbTiN film in [93].

8.5 EFFECT OF THE SUBSTRATE ROUGHNESS

The surface topographical defects induce local field enhancements triggering premature vortex penetration at the field well below the maximum achievable field or superheating field. Thin films follow the roughness of the substrates. In previous work, NbTiN samples were coated on chemically polished Nb which has micrometer roughness as shown in Fig. 67(a). A smoother surface could result in a more stable SIS structure under a higher surface field.

In this work, the next step is directed to produce an Nb substrate with a smoother surface. In this task, the mechanical polishing (ML) procedure was optimized to remove a damaged surface layer and obtain an even mirror finish surface (Fig. 67(b)) in less amount of time and effort. This was done in a few steps: first coarse polishing follows to remove the bulk of the deformed surface from the sheet fabrication process, then intermediate polishing may be required to reduce deformations further and final polishing was to make the surface smooth and shiny. Starting from 250 μm thick Nb, shiny smooth surface ended up around 150 μm. This could have started from a higher thickness than 250 μm to ended up by 250 μm for easy comparison.
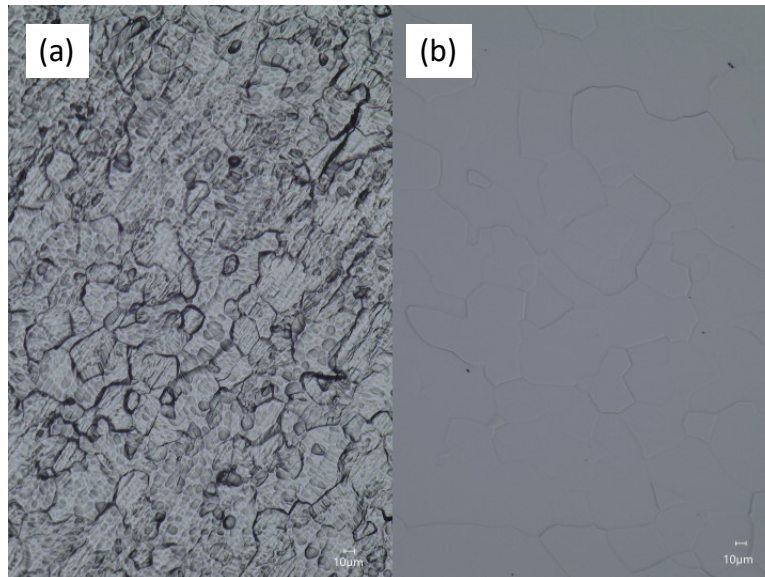
FIG. 67. Optical images of (a) BCP and (b) mechanically polished along with the electropolishing Nb substrate. Roughness of BCP and MP+EP Nb is $\sim$ 3 μm and 20 nm respectively.

However, in this process, we cannot guarantee the final thickness, but if samples are polished at the same time (four or five 2-inch samples) would finish with nearly equal thickness. A polishing machine from Buehler was used to polish samples mounted on stages using wax as shown in Fig. 68(a). The sample stage mounted to the machine is spinning on the rotating polishing pad both in the same direction or opposite directions as needed. Slurry, a mixture of denser particles (15, 9, 3, 1 μm big) flows on to the pad while polishing to speed up the process. Starting from a slurry with large particles move forward reducing the particle sizes, finally use the mixture of silica, H_2O_2, and water for the mirror finish. The time for the process may vary with the nature of the surface. Further, samples surface should be cleaned to remove if particles are embedded in the top layer from the mechanical polishing (MP) process. Next step is followed up with electropolishing (EP) of the sample to remove 3-4 μm thick material from the surface.
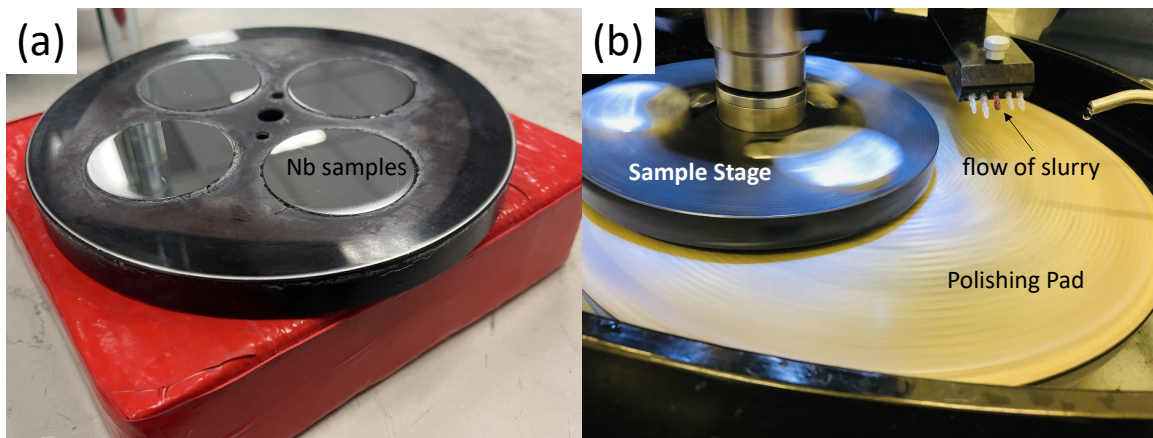
FIG. 68. Mechanical polishing set up (a) Nb samples mounted on sample stage using wax, these four samples are polished for mirror finish (b) sample stage is spinning on the polishing pad along with flow of slurry.

Two MP+EP Nb substrates (150 μm thick) were used to coat NbTiN/AlN SI structure flowing the same thickness of sample no. 6 and 7 (NbTiN layer thickness 250 and 371 μm) in

Table 7 to study the effect on different roughness of the substrate. MFP magnetometer measurements are shown in Fig. 69, comparing B_p of the bare BCP Nb. Note that we can not directly compare NbTiN/AlN coated on MP+EP Nb (150 μm thick) here with NbTiN/AlN coated BCP Nb (250 μm thick) in the above study due to the different thicknesses of substrates. MFP magnetometer measurements are thickness dependent as demonstrated in chapter 6.
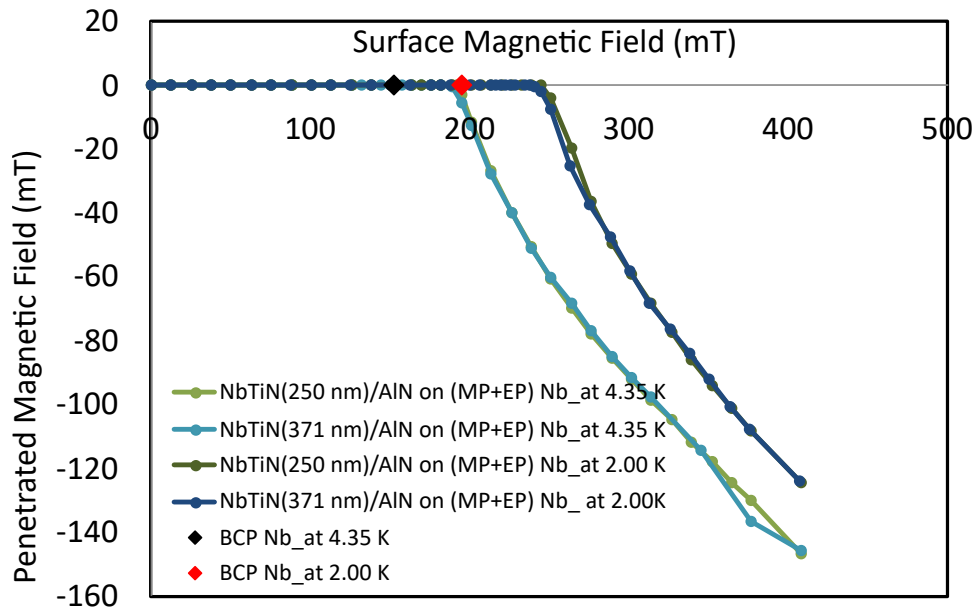
FIG. 69. The penetrated field at 4.35 K and 2.00 K for NbTiN/AlN coated on mechanically polished (MP) and electropolished (EP) Nb (150 μm thick) comparing with chemically polished (BCP) bare Nb with the same thickness. Samples with MP+EP Nb substrates shows 25.5 % and 20 % enhancement of B_p compared to bare BCP Nb at 4.35 K and 2.00 K respectively.

Then, it would be easy to calculate B_p at 150 μm thickness from B_p vs thickness curve for BCP Nb in chapter 6 and compare. As shown in Fig. 69, B_p does not significantly changing with the NbTiN layer thickness at both temperatures. Both samples represent a 25 % increase at 4.35 K and 20 % at 2.00 K compared to bare BCP Nb. This enhancement

is significant and it is about ∼10 % compared to NbTiN/AlN deposited on rough BCP Nb. Most importantly, samples are in good condition after MFP magnetometer measurements. Further work is needed to develop the procedure for more pronounced results along with other characterization methods.

CHAPTER 9

SUMMARY, CONCLUSION AND FUTURE WORK

The main purpose of the present work has been to develop an experimental setup and then perform magnetic field penetration measurements of planar superconductors used in current and next-generation SRF cavities emulating the field profile at the wall of the SRF cavity operating at fundamental accelerating mode. This setup is known as Magnetic Field Penetration (MFP) magnetometer, which was designed, built, and then implemented at Jefferson Lab.

MFP magnetometer can be used to measure magnetic field penetration through planar supercondcting sample with 2 inch diameter and up to a few mm in thickness. It consists of main components, the superconducting magnet which is placed on the sample to produce the magnetic field parallel to the sample surface to mimic the field profile at the SRF cavity wall, three Hall probes mounted other side of the sample along the sample radius (at 0, 4.4 and 10.0 mm) to detect penetrated field through the sample and separator plate (initially sapphire then copper plate with 0.5 mm thickness) inserted between magnet bottom and sample to maintain fixed gap. All the components are assembled in a non magnetic container symmetrically that attached to the cryogenic insert at vertical test facility at Jefferson lab to perform the measurements submerging the setup in liquid He bath at 4.35 K and 2.00 K.

In the first part of the experiment, the superconducting magnet was designed and fabricated under the lab facility at the Center for Accelerator Science at Old Dominion University and tested at Jefferson Lab at cryogenic temperature. Then, Hall probes were tested and calibrated using a separate setup. In the second part of the experiment, assembled setup was calibrated to find the maximum surface field applied on the sample, that is 6.26 mT/A, used for current-field conversion when a superconductor is in Meissner state up to the breakdown of the superconductivity. In the magnetic field penetration measurements, the first full flux penetration, B_p (a key parameter to characterize superconductors to improve the performance of SRF cavities) can be clearly identified. The measurements were done in three categories: bulk, thin films, and multi-layered superconductors.

9.1 MEASUREMENTS ON BULK SUPERCONDUCTORS

9.1.1 SUMMARY

First bulk lead and niobium samples were tested for field penetration measurements. The center Hall probe detected a strong signal compared to other probes and in the case of Nb, the Hall probe at 10.0 mm detected the opposite signal. Hysteresis behavior was also observed for those materials. The measurements were repeated for samples with different thicknesses (range of a few hundred of μm) and B_p was graphically represented as a function of thickness. Next, a model was built to simulate B_p at different magnet currents and matched with the experimental data.

9.1.2 CONCLUSION

Bulk lead and niobium testings reveal that MFP magnetometer measurement depends on the sample thickness which is B_p is a function of sample thickness. The plot B_p vs sample thickness for both lead and niobium is linear. Extrapolated B_p at zero thickness agrees with the well-known critical field of lead and niobium as shown in Table 8. The small deviation is due to impurities inside and defects on the surface of the samples.

TABLE 8. Critical field of lead and niobium from measurements compared to values from references.
.

	Critical Field (mT)		
Sample	Lead	Niobium	
	4.35 K	4.35 K	2.00 K
(a) From Reference	52.6 [28]	135.1 [29]	165.4 [29]
(b) From Measurement	51.7	132.5	163.3

Hysteresis curve observed under forward and backward current is also an attractive outcome. Further studies on this is out of our experimental goal.

The model is based on the concept that once the superconductor transforms to the flux transparent mixed state, the center region of the superconductor is in the mixed state while the peripheral part is still in the Meissner state. Permeability, μ variation along the sample radius was presented for bulk lead and niobium samples with thickness 250 μm at different magnet currents to match the simulation of penetrated magnetic field with lab data. This is under further studies to improve the simulations.

9.2 MEASUREMENTS ON THIN FILM SUPERCONDUCTORS

9.2.1 SUMMARY

In this section, the first thin film measurements were done using Nb thin film (thickness nearly 1-3 μm) fabricated on sapphire and bulk copper. 1.5 μm thick Nb_sSn and Nb_sSn/Al_2O_3 coated on a sapphire substrate also measured under different magnetic field ramp rates: 3.13 mT/A and 0.626 mT/A. The sapphire separator plate placed between the magnet and the sample was replaced by a copper plate with the same thickness to observe the effect on the measurements.

9.2.2 CONCLUSION

The magnetic field penetration through thin film depends on the quality of the substrates which is a great influence on the quality of the film. Thin films typically take the substrate morphology, thus the substrate roughness affects the roughness of the thin film. Nb thin film coated on sapphire shows higher RRR, compared to that of copper. Even though Nb thin film coated on sapphire has high RRR, Nb thin film coated on copper showed magnetic field penetration relatively at higher fields. This is due to the high thermal conductivity of copper that allows for transporting heat efficiently across the sample. Furthermore, among the Nb thin films coated on copper, one having low RRR showed early magnetic field penetration too, which tells that B_p has a significant influence on material purity.

Magnetic field penetration measurements of both Nb_sSn and Nb_sSn/Al_2O_3 coated on a sapphire plate showed flux jumps due to thermo-magnetic instability, which is mitigated by increasing thermal conductivity across thesample by replacing the separator plate (sapphire) by copper with the same thickness. B_p is increased by slowing down the current ramp rate.

The magnetic field ramp rate of 0.626 mT/A was chosen for future measurements. Note that the thin film samples are intact during the testings, which means the MFP magnetometer is adequate not only for bulk measurements but also for the thin film measurements.

9.3 MEASUREMENTS ON MULTILAYER SUPERCONDUCTORS

9.3.1 SUMMARY

To explore the SIS concept to enhance the SRF cavity performance, the structure of NbTiN (superconductor) and AlN (insulator) layers fabricated on bulk Nb was chosen. The first two samples of single-layer NbTiN on bulk Nb were tested for field penetration along with resistivity vs temperature measurements, XRD, and EBSD profile.Then the effect of NbTiN layer thickness on B_p measurements was observed using four samples of NbTiN/AlN coated on bulk Nb with NbTiN layer thickness 83, 166, 250, 371 nm keeping AlN layer thickness constant ~ 10 nm. They were also tested for resistivity vs for temperature, XRD, and EBSD profile.

Besides, the effect of surface roughness was also started to study. The Nb substrates prepared from chemical polishing ended up with a micrometer rough surface. Thus, mechanical polishing along with electropolishing was used to smoothen the Nb surface to obtain mirror shine surface with nanometer roughness in order to prepare multilayer with sharp interfaces and to increase the B_p of multilayer samples. Two Nb samples were smoothened using the procedure of mechanical polishing and electropolishing to get a mirror shine-less rough surface and coated with NbTiN/AlN with a thickness comparable to the last two samples from the above thickness measurement series (NbTiN layers are 250 and 371 nm thick and AlN layer is 10 nm thick).

9.3.2 CONCLUSION

Single layer NbTiN on bulk Nb showed maximum B_p among samples coated on bulk Nb. They showed sharp resistive transition and a very clear polycrystalline nature is observed from EBSD images compared to bilayer films. This reveals that the sample quality affects the B_p measurements.

However, the most interesting results were obtained from the series of NbTiN/AlN coated on BCP Nb samples with different thicknesses with constant AlN thickness. The variation of B_p confirms the existence of optimum thickness of the S layer for maximum field and that

is consistent with the theory built up in Ref. [92]. The optimum thickness of NbTiN for maximum B_p among four thicknesses is 166 nm when AlN is nearly 10 nm which shows 24 % and 27 % increase compared to bare Nb observed at 3.45 K and 2.00 K in order. The optimum thickness varies with penetration depth, λ, and coherence length, ξ of the samples.

NbTiN/AlN coated on mechanically polished followed by electropolishing Nb substrates performed better than those coated on BCP substrate. Comparison is tricky due to different substrate thicknesses which affect the measurements. However, 25.5% and 20% percentage increase compared to BCP bare bulk Nb was observed at 3.45 K and 2.00 K respectively. Moreover, $\sim$10 % increase was estimated compared to NbTiN/AlN bilayer coated on BCP Nb. More work is required to get more pronounced results.

Overall, a combination of numerical modeling and experimental measurements could help to improve our understanding of the behavior of superconductors in an external magnetic field and pave the way for the development of more efficient superconducting materials for SRF applications.

9.4 FUTURE WORK

To improve the simulation of magnetic field penetration through superconductors in the mixed state, we could consider using a more sophisticated model that takes into account the complex interplay between the magnetic field, the superconducting state, and the material properties of the superconductor. One approach could be to use a three-dimensional numerical model that solves the time-dependent Ginzburg-Landau equations coupled with Maxwell's equations, which can capture the complex dynamics of the magnetic field and the superconductor.

Regarding the experiments on Nb treated with mechanical polishing and electropolishing, it may be worthwhile to vary the polishing parameters, such as the polishing time, and the polishing pressure, to optimize the surface quality of the Nb samples. Additionally, it may be beneficial to perform complementary measurements, such as scanning electron microscopy or atomic force microscopy, to characterize the surface morphology of the samples and correlate it with their superconducting properties.

Exploring SIS multilayers with other promising superconducting materials could provide valuable insights. We could try using different materials for the S and I layers, or varying the thickness of the layers, to see how these factors affect the B_p measurements. Additionally, measuring the B_p of multilayered Nb with a stack of SI layers could provide information on effectiveness of multilayers clearly.

BIBLIOGRAPHY

[1] H. Padamsee, J. Knobloch, and T. Hays, *RF Superconductivity for Accelerators* (Wiley & Sons, New York, 1998).

[2] H. Padamsee, The science and technology of superconducting cavities for accelerators, Superconductor Science and Technology **14**, 28–51 (2001).

[3] H. Padamsee, *RF Superconductivity- Science Technology and Applications* (WILEY-VCH, 2009).

[4] R. L. Geng, H. Padamsee, A. Seaman, and V. D. Shemelin, World record accelerating gradient achieved in a superconducting niobium RF cavity, in *Proc. Particle Accelerator Conference PAC2005* (JACoW Publishing, Geneva, Switzerland, 2005) pp. 653–655.

[5] F. Furuta, T. Konomi, K. Saito, G. V. Eremeev, and R. L. Geng, High gradient results of ICHIRO 9-cell cavity in collaboration with KEK and JLab, in *Proc. 15th International Conference on RF Superconductivity SRF2011* (JACoW Publishing, Geneva, Switzerland, 2011) pp. 386–390.

[6] D. Reschke, S. Aderhold, A. Gössel, J. Iversen, S. Karstensen, D. Kostin, G. Kreps, A. Matheisen, W.-D. Möller, F. Schlander, W. Singer, X. Singer, N. Steinhau-Kühl, A. Sulimov, and K. Twarowski, Results on large grain nine-cell cavities at DESY: gradients up to 45 MV/m after electropolishing, in *Proc. SRF2011*, International Conference on RF Superconductivity No. 15 (JACoW Publishing, Geneva, Switzerland, 2011) pp. 490–494.

[7] A. Grassellino, A. Romanenko, Y. Trenikhina, M. Checchin, M. Martinello, O. S. Melnychuk, S. Chandrasekaran, D. A. Sergatskov, S. Posen, A. C. Crawford, S. Aderhold, and D. Bice, Unprecedented quality factors at accelerating gradients up to 45 MVm^{-1} in niobium superconducting resonators via low temperature nitrogen infusion, Supercond. Sci. Technol. **30**, 094004 (2017).

[8] J. Matricon and D. Saint-James, Superheating fields in superconductors, Physics Letters A **24**, 241–242 (1967).

[9] M. K. Transtrum, G. Catelani, and J. P. Sethna, Superheating field of superconductors within Ginzburg-Landau theory, Phys. Rev. B **83**, 094505 (2011).

[10] F. Pei-Jen Lin and A. Gurevich, Effect of impurities on the superheating field of type-II superconductors, Phys. Rev. B **85**, 054513 (2012).

[11] A-M. Valente-Feliciano, Superconducting RF materials other than bulk niobium: a review, Supercond. Sci. Technol. **29**, 113002 (2016).

[12] T. L. Hylton and M. R. Beasley, Effect of grain boundaries on magnetic field penetration in polycrystalline superconductors, Phys. Rev. B **39**, 9042–9048 (1989).

[13] A. Gurevich, Enhancement of rf breakdown field of superconductors by multi-layer coating, Appl. Phys. Lett. **88**, 012511 (2006).

[14] A. Gurevich, Maximum screening fields of superconducting multilayer structures, AIP Advances **5**, 017112 (2015).

[15] C. Z. Antoine, S. Berry, S. Bouat, J-F. Jacquot, J-C. Villegier, G. Lamura, and A. Gurevich, Characterization of superconducting nanometric multilayer samples for superconducting rf applications: First evidence of magnetic screening effect, Phys. Rev. ST Accel. Beams **13**, 121001 (2010).

[16] A. M. Valente-Feliciano, G. Eremeev, H. L. Phillips, C. E. Reece, J.K. Spradlin, Q. Yang, D. Batchelor, and R.A. Lukaszew, NbTiN based SIS multilayer structures for SRF applications, in *Proc. 16th International Conference on RF Superconductivity SRF2013* (JACoW Publishing, Geneva, Switzerland, 2013).

[17] T. Tan, M.A.Wolak, X.X.Xi, T.Tajima, and L. Civale, Magnesium diboride coated bulk niobium: a new approach to higher acceleration gradient, Sci Rep **6**, 35879 (2016).

[18] R. Ito, T. Nagata, H. Hayano, T. Kubo, T. Saeki, Y. Iwashita, R. Katayama, H. Ito, and H. Oikawa, Development of Coating Technique for Superconducting Multilayered Structure, in *Proc. 9th International Particle Accelerator Conference, IPAC2018* (JACoW Publishing, Geneva, Switzerland, 2018) pp. 4954–4956.

[19] C. Z. Antoine, M. Aburas, A. Four, F. Weiss, Y. Iwashita, H. Hayano, S. Kato, T. Kubo, and T. Saeki, Optimization of tailored multilayer superconductors for RF application and protection against premature vortex penetration, Supercond. Sci. Technol. **32**, 085005 (2019).

[20] A. Gurevich, Theory of RF superconductivity for resonant cavities, Supercond. Sci. Technol. **30**, 034004 (2017).

[21] E. H. Brandt, The flux-line lattice in superconductors, Rep. Prog. Phys. **58**, 1465 (1995).

[22] E. Zeldov, A. I. Larkin, V. B. Geshkenbein, M. Konczykowski, D. Majer, B. Khaykovich, V. M. Vinokur, and H. Shtrikman, Geometrical barriers in high-temperature superconductors, Phys. Rev Lett. **73**, 1428–1431 (1994).

[23] E. H. Brandt, Geometric barrier and current string in type-II superconductors obtained from continuum electrodynamics, Phys. Rev. B **59**, 3369–3372 (1999).

[24] T. Junginger, W. Weingarten, and C. Welsch, Extension of the measurement capabilities of the quadrupole resonator, Rev. Sci. Instrum. **83**, 063902 (2012).

[25] S. Keckert, R. Kleindienst, O. Kugeler, D. Tikhonov, and J. Knobloch, Characterizing materials for superconducting radiofrequency applications-a comprehensive overview of the quadrupole resonator design and measurement capabilities, Rev. Sci. Instrum. **92**, 064710 (2021).

[26] O. B. Malyshev, L. Gurran, R. Valizadeh, S. Pattalwar, N. Pattalwar, K. D. Dumbell, and A. Gurevich, First Results of Magnetic Field Penetration Measurements on Multilayer S-I-S Structures, in *Proc. 7th International Particle Accelerator Conference, IPAC2016* (JACoW, Geneva, Switzerland, 2016) pp. 2245–2247.

[27] A. C. Rose-Innes and E. H. Rhoderick, *Introduction of Superconductivity*, 2nd ed. (Pergamon, Oxford, 1978).

[28] G. Chanin and J. P. Torre, Critical-field curve of superconducting lead, Phys. Rev. B **5**, 4357–4364 (1972).

[29] D. K. Finnemore, T. F. Stromberg, and C. A. Swenson, Superconducting properties of high-purity niobium, Phys. Rev. **149**, 231–243 (1966).

[30] P. Zhang, J. Li, Q. Guo, Y. Zhu, K. Yan, R. Wang, K. Zhang, X. Liu, and Y. Feng, *Titanium for Consumer Applications* (Elsevier, 2019).

[31] A. Godeke, Nb_3Sn for radio frequency cavities, Lawrence Berkeley National Lab.(LBNL), Berkeley, CA (United States), Tech. Rep. (2006).

[32] C. Yen, L. Toth, Y. Shy, D. Anderson, and L. Rosner, "superconducting hc-jc and tc measurements in the Nb-Ti-N, Nb- Hf-N, and Nb-V-N ternary systems, Journal of Applied Physics **38**, 2268–2271 (1967).

[33] H. K. Onnes, The superconductivity of mercury, Leiden Comm. , 122–124 (1911).

[34] C. J. Gorter and H. B. J. Casimir, Two fluid model, Z. Phys. **35**, 963 (1934).

[35] F. London and H. London, The electromagnetic equations of the supraconductor, Proceedings of the Royal Society A: Mathematical, Physical and Engineering Sciences **149 (866)**, 71–88 (1935).

[36] V. L. Ginzburg and L. D. Landau, On the theory of superconductivity, J. Exptl. Theoret. Phys. (U.S.S.R.) **20**, 1064 (1950).

[37] J. Bardeen, L. N. Cooper, and J. R. Schrieffer, Microscopic theory of superconductivity, Phys. Rev. **106** (1957).

[38] J. Bardeen, L. N. Cooper, and J. R. Schrieffer, Theory of superconductivity, Phys. Rev. **108**, 1175–1204 (1957).

[39] W. Meissner and R. Ochsenfeld, Ein neuer effekt bei eintritt der supraleitfhigkeit, Naturwissenschaften **21(44)**, 787–788 (1933).

[40] A. B. Pippard and W. L. Bragg, An experimental and theoretical study of the relation between magnetic field and current in a superconductor, Proc. R. Soc. Lond. A **216**, 547–568 (1953).

[41] M. Tinkham, *Introduction to Superconductivity* (New York: McGraw-Hill, 1975).

[42] L. N. Cooper, Bound electron pairs in a degenerate fermi gas, Phys. Rev. **104**, 1189–1190 (1956).

[43] B. Shen, *Study of Second Generation High Temperature Superconductors: Electromagnetic Characteristics and AC Loss Analysis* (Springer, Cham, 2020).

[44] V. F. Weisskopf, The formation of cooper pairs and the nature of superconducting currents, Contemporary Physics **22**, 375–395 (1981).

[45] R. G. Sharma, *Superconductivity: Basics and Applications to Magnets* (Springer Cham, 2015).

[46] J. C. Loudon and P. A. Midgley, Imaging flux vortices in type ii superconductors with a commercial transmission electron microscope, Ultramicroscopy **109** (2009).

[47] C. P. Bean and J. D. Livingston, Surface barrier in type-ii superconductors, Phys. Rev. Lett. **12**, 14–16 (1964).

[48] V. V. Schmidt, V. V. Schmidt, P. Müller, and A. V. Ustinov, *The Physics of Superconductors: Introduction to Fundamentals and Applications* (Springer, 1997).

[49] J. Matricon and D. Saint-James, Superheating fields in superconductors, Physics Letters A **24**, 241–242 (1967).

[50] D. Saint-James and P. D. Gennes, Onset of superconductivity in decreasing fields, Physics Letters **7**, 306–308 (1963).

[51] H. Padamsee, History of gradient advances in SRF, 2020arXiv200406720P (2020).

[52] A. Romanenko, A. Grassellino, O. Melnychuk, and D. A. Sergatskov, Dependence of the residual surface resistance of superconducting radio frequency cavities on the cooling dynamics around tc, Journal of Applied Physics **115**, 184903 (2014).

[53] J. Knobloch, The "Q disease" in superconducting niobium rf cavities, AIP Conference Proceedings **671**, 133–150 (2003).

[54] C. Sundahl, J. Makita, P. B. Welander, Y-F. Su, F. Kametani, L. Xie, H. Zhang, L. Li, A. Gurevich, and C.-B. Eom, Development and characterization of Nb_3Sn/Al_2O_3 superconducting multilayers for particle accelerators, Sci Rep **11**, 7770 (2021).

[55] W. M. Roach, J. R. Skuza, D. B. Beringer, Z. Li, C. Clavero, and R. A. Lukaszew, NbN thin films for superconducting radio frequency cavities, Supercond. Sci. Technol. **25**, 125016 (2012).

[56] M. C. Burtona, M. R. Beebe, K. Yang, R. A. Lukaszew, A-M. Valente-Feliciano, and C. Reece, Superconducting NbTiN thin films for superconducting radio frequency accelerator cavity applications, J. Vac. Sci. Technol. **A 34**, 021518 (2016).

[57] E. W. Collings, M. D. Sumption, and T. Tajima, Magnesium diboride superconducting rf resonant cavities for high energy particle acceleration, Supercond. Sci. Technol. **17**, S595 (2004).

[58] A. A. Abrikosov, On the lower critical field of thin layers of superconductors of the second group, Sov. Phys. JETP **19** (1964).

[59] G. Stejic, A. Gurevich, E. Kadyrov, D. Christen, R. Joynt, and D. C. Larbalestier, Effect of geometry on the critical currents of thin films, Phys. Rev. B **49**, 1274–1288 (1994).

[60] T. Kubo, Multilayer coating for higher accelerating fields in superconducting radio-frequency cavities: a review of theoretical aspects, Supercond. Sci. and Tech. **30**, 023001 (2016).

[61] D. R. Beverstock, C. Z. Antoine, J. R. Delayen, D. Manos, I. H. Senevirathne, J. K. Spradlin, and A-M. Valente-Feliciano, Samples for 3rd Harmonic Magnetometry Assessment of NbTiN-Based SIS Structures, in *Proc. 20th International Conference on RF Superconductivity SRF2021*, pp. 164–166.

[62] H. Ito, C.Z. Antoine, A. Four, H. Hayano, T. Kubo, T. Saeki, R. Ito, T. Nagata, Y. Iwashita, R. Katayama, H. Tongu, and H. Oikawa, Lower critical field measurement system of thin film superconductor, in *Proc. 9th International Particle Accelerator Conference, IPAC2018* (JACoW Publishing, Geneva, Switzerland, 2018) pp. 3882–3884.

[63] A. T. Fiory and A. F. Hebard, Penetration depths of high Tc films measured by two-coil mutual inductances, Appl. Phys. Lett. **52**, 2165 (1988).

[64] D. G. Xenikos and T. R. Lemberger, Ac susceptibility apparatus for measuring the transition temperature of high-Tc crystals, sintered samples, and films, Rev. Sci. Instrum. **60**, 831 (1989).

[65] J. H. Claassen, M. E. Reeves, and R. J. Soulen Jr., A contactless method for measurement of the critical current density and critical temperature of superconducting films, Rev. Sci. Instrum. **62**, 996 (1991).

[66] S. J. Turneaure, A. A. Pesetski, and T. R. Lemberger, Numerical modeling and experimental considerations for a two-coil apparatus to measure the complex conductivity of superconducting films, J. Appl. Phys. **83**, 4334 (1998).

[67] T. R. Lemberger and A. Ahmed, Upper limit of metastability of the vortex-free state of a two-dimensional superconductor in a nonuniform magnetic field, Phys. Rev. B **87**, 214505 (2013).

[68] J. Draskovic, T.R. Lemberger, B. Peters, F. Yang, J. Ku, A. Bezryadin, and S. Wang, Measuring the superconducting coherence length in thin films using a two-coil experiment, Phys. Rev. B **88**, 134516 (2013).

[69] D. Turner, O. B. Malyshev, G. Burt, T. Junginger, L. Gurran, K. D. Dumbell, A. J. May, N. Pattalwar, and S. M. Pattalwar, Facility for the characterization of planar multilayer thin film superconductors, Journal of Physics: Conference Series **1559**, 012067 (2020).

[70] C. H. Hinrichs and C. A. Swenson, Superconducting critical field of tantalum as a function of temperature and pressure, Phy. Rev. **123** (1961).

[71] J. R. Clem, Theory of ac losses in type-II superconductors with a field-dependent surface barrier, J. Appl. Phys. **50**, 3518–3530 (1979).

[72] A. S. Dhavale, P. Dhakal, A. A. Polyanskii, and G. Ciovati, Flux pinning characterization in cylindrical niobium samples used for superconducting radio frequency cavity fabrication, Supercond. Sci. Technol. **25**, 065014 (2012).

[73] C. Benvenuti, S. Calatroni, I. E. Campisi, P. Darriulat, M. A. Peck, R. Russo, and A. M. Valente, Study of thesurface resistance of superconducting niobium films at1.5 GHz, Physica C (Amsterdam) **316** (1999).

[74] C. James, M. Krishnan, B. Bures, T. Tajima, L. Civale, R. Edwards, J. Spradlin, and H. Inoue, Superconducting Nb thin films on Cu for applications in SRF accelerators, IEEE Transactions on Applied Superconductivity **23**, 3500205–3500205 (2013).

[75] W. Singer, A. Ermakov, and X. Singer, RRR-measurement techniques on high purity niobium, TTC report **2** (2010).

[76] C. Benvenuti, N. Circelli, and M. Hauer, Niobium films for superconducting accelerating cavities, Appl. Phys. Lett. **583** (1984).

[77] S. Calatroni, 20 years of experience with the Nb/Cu technology for superconducting cavities and perspectives for future developments, Physica C: Superconductivity **441**, 95–101 (2006), proceedings of the 12th International Workshop on RF Superconductivity.

[78] G. Wu, A.-M. Valente, H. L. Phillips, H. Wang, A.T. Wu, T. J. Renk, and P. Provencio, Studies of niobium thin film produced by energetic vacuum deposition, Thin Solid Films **489**, 56–62 (2005).

[79] R. Russo, Quality measurement of niobium thin films for Nb/Cu superconducting RF cavities, Measurement Science and Technology **18**, 2299 (2007).

[80] Md. N. Sayeed, H. Elsayed-Ali, M.C. Burton, G.V. Eremeev, C.E. Reece, A-M. Valente-Feliciano, and U. Pudasaini, Deposition of Nb$_3$Sn films by multilayer sequential sputtering for SRF cavity application, in *Proc. 19th International Conference on RF Superconductivity, SRF2019* (JACoW Publishing, Geneva, Switzerland, 2019) pp. 639–643.

[81] R. G. Mints and A. L. Rakhmanov, Critical state stability in type-II superconductors and superconducting-normal-metal composites, Rev. Mod. Phys. **53**, 551–592 (1981).

[82] E. Altshuler and T. H. Johansen, Colloquium: Experiments in vortex avalanches, Rev. Mod. Phys. **76**, 471–487 (2004).

[83] I. S. Aranson, A. Gurevich, M. S. Welling, R. J. Wijngaarden, V. K. Vlasko-Vlasov, V. M. Vinokur, and U. Welp, Dendritic flux avalanches and nonlocal electrodynamics in thin superconducting films, Phys. Rev. Lett. **94**, 037002 (2005).

[84] J. I. Vestgården, D. V. Shantsev, Y. M. Galperin, and T. H. Johansen, Dynamics and morphology of dendritic flux avalanches in superconducting films, Phys. Rev. B **84**, 054537 (2011).

[85] P. Mikheenko, A. J. Qviller, J. I. Vestgården, S. Chaudhuri, I. J. Maasilta, Y. M. Galperin, and T. H. Johansen, Nanosecond voltage pulses from dendritic flux avalanches in superconducting NbN films, Appl. Phys. Lett. **102**, 022601 (2013).

[86] S. Posen, J. Lee, D. N Seidman, A. Romanenko, B. Tennis, O. S Melnychuk, and D. A Sergatskov, Advances in Nb$_3$Sn superconducting radiofrequency cavities towards first practical accelerator applications, Supercond. Sci. Technol. **34**, 025007 (2021).

[87] A-M Valente-Feliciano, G. Eremeev, H. Phillips, C. Reece, J. Spradlin, Y. Qiquang, D. Batchelor, and R. Lukaszew, NbTiN based sis multilayer structures for SRF applications, in *Proc. 15th International Conference on RF Superconductivity, SRF2013*, Vol. 34 (2013) pp. 670–673.

[88] Z. Cheng, , Y. R. Koh, A. Mamun, J. Shi, T. Bai, K. Huynh, L. Yates, Z. Liu, R. Li, E. Lee, M. E. Liao, Y. Wang, H. M. Yu, M. Kushimoto, T. Luo, M. S. Goorsky, P. E. Hopkins, H. Amano, A. Khan, and S. Graham, Experimental observation of high intrinsic thermal conductivity of AlN, Phys. Rev. Mater. **4**, 044602 (2020).

[89] A-M Valente-Feliciano, M. Burton, G. Eremeev, R. Lukaszew, C. Reece, and J. Spradlin, Growth and characterization of multilayer NbTiN films, in *Proc.17th International Conference on RF SuperconductivitySRF2015*, Vol. 34 (2015).

[90] T. Junginger, T. Prokscha, Z. Salman, A. Suter, and A-M. Valente-Feliciano, Critical fields of SRF materials, in *Proc. 9th International Particle Accelerator Conference, IPAC2018*.

[91] Lei Yu, R.K. Singh, Hongxue Liu, S.Y. Wu, R. Hu, D. Durand, J. Bulman, J.M. Rowell, and N. Newman, Fabrication of niobium titanium nitride thin films with high superconducting transition temperatures and short penetration lengths, IEEE Transactions on Applied Superconductivity **15**, 44–48 (2005).

[92] Takayuki Kubo, Yoshihisa Iwashita, and Takayuki Saeki, Radio-frequency electromagnetic field and vortex penetration in multilayered superconductors, Applied Physics Letters **104**, 032603 (2014).

[93] A. Klimov, W. Słysz, M. Guziewicz, V. Kolkovsky, I. Zaytseva, and A. Malinowski, Characterization of the critical current and physical properties of superconducting epitaxial NbTiN sub-micron structures, Physica C: Superconductivity and its Applications **536**, 35–38 (2017).

VITA

Iresha Harshani Senevirathne

Department of Physics

Old Dominion University

Norfolk, VA 23529

Education:

- M.S. Physics, Old Dominion University, Norfolk, VA. May 2018

- B.Sc. major in Physics, University of Peradeniya, Sri Lanka. January 2014

Publications:

- I. H. Senevirathne, A. Gurevich, J. R. Delayen, Direct Current Magnetic Hall Probe Technique for Measurement of Field Penetration in Thin Film Superconductors for Superconducting Radio Frequency Resonators, Review of Scientific Instruments, 93, 055104, 2022, doi.org/10.1063/5.0083309.

- I. H. Senevirathne, D. R. Beverstock, A-M Valente-Feliciano, A. Gurevich, J. R. Delayen, Field Shielding of NbTiN Based Multilayer Structure for Accelerating Cavities, *in proc. of LINAC2022*, Liverpool, UK, 2022, doi:10.18429/JACoW-LINAC2022-THPOGE19.

- I. H. Senevirathne, A-M Valente-Feliciano, A. Gurevich, J. R. Delayen, Measurement of magnetic field penetration in superconducting materials for SRF cavities, *in Proc. of IPAC21*, Campinas, Brazil, 2021, doi.org/10.18429/JACoW-IPAC2021-MOPAB396.

- I. H. Senevirathne, A. Gurevich, J. R. Delayen, Magnetic Field Penetration Technique to Study High Field Shielding of Multilayered Superconductors, *in Proc. of SRF2021*, East Lansing, MI, USA, 2021, doi:10.18429/JACoW-SRF2021-SUPTEV001.

- I. H. Senevirathne, G. Ciovati, J. R. Delayen, Measurements of the Magnetic Field Penetration into Superconducting Thin Films, *in Proc. of SRF2019*, Dresden, Germany, 2019, doi:10.18429/JACoW-SRF2019-THP050.

Typeset using LaTeX.